Measurement of the Branching Ratio of $K_L \to e^+e^-\gamma\gamma$

DISSERTATION

Presented in Partial Fulfillment of the Requirements
for the Degree of Doctor of Science
in the Graduate School of Osaka University

By
Tsuyoshi Nakaya

Osaka University

1995

ACKNOWLEDGMENTS

I would like first to thank my advisor, Yorikiyo Nagashima, for his gentle support and supervising my education throughout these years. I owe special thanks to Taku Yamanaka for his continuous support and many important advice regarding this work. Really, I enjoyed all works with him. I greatly appreciate the encouragement by Junji Haba who taught me the phenomena of the high energy physics. Special thanks go to Masato Takita from whom I gained invaluable insight into physics.

The work presented here is a result of group effort. I am indebted to all collaborators on experiment E799. Many thanks go to Elliott Chue, Yau Wai Wah, William Slater, Peter Haas and Bob Tschirhart who corrected my poor English and gave many important suggestions regarding this analysis. I also greatly appreciate many discussions with Kevin Scott McFarland, Deborah Appel Harris, Roy Briere, Bernhard Schwingenheuer, Ping Gu, John Matthews, Doug Roberts, Matthew Weaver and Matthew Spencer. Katsushi Arisaka, Bruce Winstein, Tony Barker, Greg Bock, Mike Crisler, Rick Ford, Bob Hsiung, Doug Jensen and Erik Ramberg have all made substantial contributions to this work as well. I also discussed the physics in the $K_L \to e^+e^-\gamma\gamma$ decay with H.B. Greenlee, G. Isidori, G. D'Ambrosio, and B. McKellar. I give great thanks to them.

To my colleagues at the Osaka university: Atsumu Suzuki, Nobuyuki Kanda, Hiroyuki Takagi, Hiroyuki Hanai, Takanori Hara and Yasuhiro Yamamoto, I give thanks, too. We had a nice time with discussions about physics. In addition, I enjoyed the life at the university with Daisuke Tatsumi, Motoharu Yagi, Yuji Matsumiya, Naoki Kishi, Kazunori Hanagaki, Koji Adachi, Takeo Kawasaki, Toshihiro Tsuji, Takayuki Yamaguchi, Katsumi Senyou, Fumihiko Kato, Masayoshi Sadamoto and Sachiko Tsuzuki.

I would also like to thank Michiko Tanaka, Mr. Sugioka, Sachiko Tanimoto and Takahiko Tomita as my teachers who gave suggestions to me when I advanced to the physics course.

I wish to thank my parents, Toshio and Akiko Nakaya who have supported me through the long years with their unlimited encouragement. Additional thanks go to my parents in law, Ichio and Sumiko Kawakami for their moral support. Finally I am very grateful to the life with my wife, Akiko Nakaya whom I live together forever and a day.

THE FNAL-E799 COLLABORATION

Katsushi Arisaka, Doug Roberts, William Slater, Matt Spencer, Matt Weaver
University of California at Los Angeles

Roy Briere, Elliott Cheu, Deborah Harris, Pat Krolak, Greg Makoff, Kevin McFarland, Aaron Roodman, Bernhard Schwingenheuer, Yau Wah, Bruce Winstein, Roland Winston
University of Chicago and The Enrico Fermi Institute

Tony Barker
University of Colorado

Earl Swallow
Elmhurst College and The Enrico Fermi Institute

Greg Bock, Rick Coleman, Mike Crisler, Janice Enagonio, Rick Ford, Yee Bob Hsiung, Doug Jensen, Erik Ramberg, Bob Tschirhart
Fermi National Accelerator Laboratory

Eric Collins, George Gollin
University of Illinois

Tsuyoshi Nakaya, Taku Yamanaka
Osaka University

Peter Haas, William P. Hogan, Sunkee Kim, John N. Matthews, Seong Sook Myung, Ping Gu, Steve Schnetzer, Sunil Somalwar, Gordon Thomson, Yu Zou
Rutgers University

Contents

List of Tables

List of Figures

ABSTRACT

This thesis presents new measurement of the $K_L \to e^+e^-\gamma\gamma$ branching ratio in Fermilab experiment E799. The decay $K_L \to e^+e^-\gamma\gamma$ is dominated by a K_L Dalitz decay, $K_L \to e^+e^-\gamma$, with an internal bremsstrahlung photon. In addition, the decay $K_L \to e^+e^-\gamma\gamma$ has a small fraction from the direct emission process. This decay is important in order to understand the long distance physics, such as the $K_L \to \gamma\gamma^*$ form factor and the $K_L \to \gamma\gamma\gamma^*$ direct emission process. This decay mode also has been a focus on general attention as the most serious background to the CP violating decay $K_L \to \pi^0 e^+e^-$. We observed 58 $K_L \to e^+e^-\gamma\gamma$ events, and measured the branching ratio to be:

$$BR(K_L \to e^+e^-\gamma\gamma, E^*_\gamma > 5MeV) = [6.5 \pm 1.2(stat.) \pm 0.6(sys.)] \times 10^{-7},$$

with a photon energy cutoff of 5 MeV/c^2 in the kaon center of mass frame. This is the first statistically significant measurement of the branching ratio. In addition, M_{ee} and $M_{\gamma\gamma}$ distributions were observed for the first time. We also searched for the direct emission process in the decay $K_L \to e^+e^-\gamma\gamma$, and set the upper limit on the branching ratio as:

$$BR(K_L \to e^+e^-\gamma\gamma[direct]) < 4.5 \times 10^{-8}\ (95\% C.L.).$$

We also set an indirect upper limit on the $K_L \to \gamma\gamma\gamma$ branching ratio as:

$$BR(K_L \to \gamma\gamma\gamma) < 1.7 \times 10^{-5}\ (95\% C.L.),$$

with an assumption of $BR(K_L \to \gamma^*\gamma\gamma \to e^+e^-\gamma\gamma) = \alpha_{QED} BR(K_L \to \gamma\gamma\gamma)$.

We also searched for a scalar particle (H) outside of the standard model, and set the upper limit on the branching ratio as:

$$BR(K_L \to He^+e^-, H \to \gamma\gamma) < 3.0 \times 10^{-8}\ (95\% C.L.),$$

for the mass between 30 and 450 MeV/c^2 with the life time of $c\tau < 10^{-2}$ m.

Chapter 1

Introduction

Kaon physics has had a long tradition of contributing many discoveries to the field of the particle physics. An introduction to kaon physics are presented in Section 1.1. Some technical terms in kaon physics are explained there, which are helpful for understanding physics of $K_L \to e^+e^-\gamma\gamma$ decay. Physics and motivation of $K_L \to e^+e^-\gamma\gamma$ is discussed in Section 1.2 in detail. An overview of this thesis is given in Section 1.3.

1.1 Introduction

At first, we should understand the general mechanism for predicting the branching ratio of each kaon decay. We do not have predictions of the branching ratios directly from the standard model for most of kaon decays because we do not know how to handle the non-perturbative aspects of the strong interaction in low energy. Usual way to predict them is through an effective field theory of the standard model, which requires some experimental results. For example, we do not have a prediction of the $K_L \to e^+e^-\gamma\gamma$ branching ratio from the standard model, but we can predict it from the effective theory by using the experimental value of the $K_L \to \gamma\gamma$ branching ratio [1]. Therefore, the decay $K_L \to e^+e^-\gamma\gamma$ is one of good laboratories for testing the effective field theory. Section 1.1.1 describes a general way of the prediction and an introduction of the effective field theory.

In addition, kaon decays are useful tools to study the symmetry properties of the weak interaction, and the manner in which these symmetries are broken. One of the important symmetries is CP symmetry which great interest is focused on. The violation of CP symmetry is found only in kaon system, and some kaon decays are sensitive to the search for the origin of the CP violation [2, 3]. The decay $K_L \to \pi^0e^+e^-$ is one of the decays which are expected to have large CP violating amplitude [3, 4]. The decay $K_L \to e^+e^-\gamma\gamma$ is noted as the most serious background of $K_L \to \pi^0e^+e^-$ [1, 3]. Therefore, the study of the decay $K_L \to e^+e^-\gamma\gamma$ is necessary to study the CP violation in the decay $K_L \to \pi^0e^+e^-$. Accordingly, the CP violation is described later in this section.

1.1.1 Prediction of Kaon Decays

The decays of kaons proceeds through two steps. The first step is the decay of a strange quark where the electroweak transition matrix element is calculated in terms of quark (and gluon) degrees of freedom. This process is referred to as a "short distance contribution". The second step is the hadronization of quarks and gluons where the matrix elements of this Hamiltonian are governed by non-perturbative confinement physics, or soft-QCD. This process is referred to as a "long distance contribution". Figure 1.1 shows the examples of both short distance contribution and long distance contribution for the decay $K_L \to \gamma\gamma$ [4, 5].

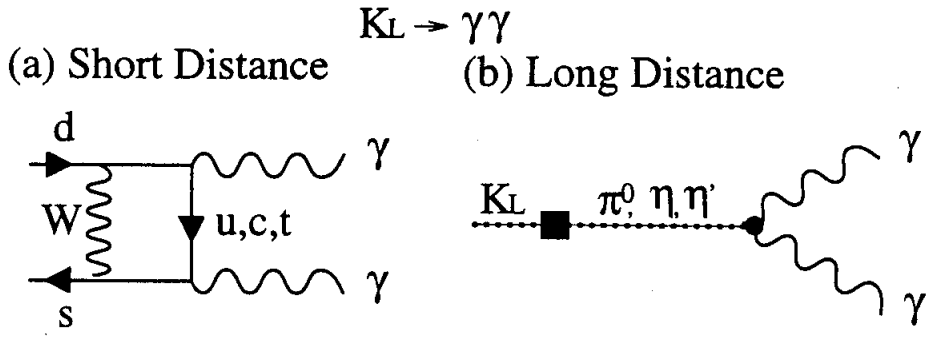

Figure 1.1: Examples of a short distance contribution (a), and a long distance contribution (b), for the decay $K_L \to \gamma\gamma$.

Short distance contribution

The short distance contribution can be calculated reliably from the standard model. In this contribution, $s-$quark decays to $u-$ or $d-$quark, and intermediately it can decay to $u-$, c^*-, or t^*-quark. Therefore, this process is related to the mixing between different generations of quarks and the mass of quarks. The mixing angles are defined as the Kobayashi-Maskawa (KM) Matrix in the standard model [6]. To order λ^3, the KM Matrix is parameterized by Wolfenstein as [7]:

$$M = \begin{pmatrix} V_{ud} & V_{us} & V_{ub} \\ V_{cd} & V_{cs} & V_{cb} \\ V_{td} & V_{ts} & V_{tb} \end{pmatrix} = \begin{pmatrix} 1-\lambda^2/2 & \lambda & A\lambda^3(\rho - i\eta) \\ -\lambda & 1-\lambda^2/2 & A\lambda^2 \\ A\lambda^3(1-\rho-i\eta) & -A\lambda^2 & 1 \end{pmatrix},$$

where λ is the sine of the Cabibbo angle, A is a quantity of order unity, and ρ and η are variables with a large uncertainty. Since the KM Matrix is a core of the standard model, the measurement of each element in KM Matrix is very important. Especially, the measurement of the parameters ρ and η is attracting much interests and efforts in the current particle physics [8].

Some kaon decays which are dominated by the short distance contribution has a sensitivity to measure the parameters in the KM matrix, and the mass of top quark. The representatives of these modes are the decays $K^+ \to \pi^+\nu\overline{\nu}$ and $K_L \to \pi^0\nu\overline{\nu}$ [9]. For some other decay modes, if the long distance contributions are calculated reliably or measured precisely from other decay modes, the above parameters can be derived [9].

Long distance contribution

Most kaon decays are dominated by the long distance contribution. These soft-QCD effects must be taken into account to make realistic predictions, and should be modelled in the most general way in order to test the underlying electroweak process from the data. In this regard, great progress has been achieved in the frame of Chiral Perturbation Theory (ChPT) [9, 10, 11] which is the effective field theory of the standard model in low energy. In this sense, it may be said that the long distance contribution is currently represented by ChPT which handles the non-perturbative aspects of QCD.

In the frame of ChPT, 8 psuedoscalar meson fields (π^+, π^-, π^0, K^+, K^-,K^0,$\overline{K^0}$, and η) and photon fields appear as following. At first, ChPT assumes the $SU(3)_L \times SU(3)_R$ chiral symmetry of QCD in the limit of massless $u-$, $d-$, and $s-$quarks. Then, the $SU(3)_L \times SU(3)_R$ symmetry spontaneously breaks down to $SU(3)_{L+R}$, and it generates the Goldstone bosons. These Goldstone bosons can be identified as π, K, and η which replace the quark and gluon fields of QCD. Then, ChPT admits an expansion of the effective Lagrangian in powers of the momentum of the psuedoscalar bosons π, K, and η. Generally, the momenta of these particles are given from a derivative. When the derivative is substituted by the covariant derivative, a photon field appears in the Lagrangian. In ChPT, the expansion of the Lagrangian is constructed from terms of even number of derivatives because of parity conservation in QCD. Therefore, the expansion starts at order $O(p^2)$ and has the form

$$L_{eff} = L_2 + L_4 + L_6 + \ldots .$$

In ChPT, the Lagrangian at order $O(p^2)$ and $O(p^4)$ has been constructed with some experimental information, which offer as parameters in meson decays. Therefore, ChPT gives good predictions for some kaon decays which are dominated by the $O(p^4)$ contribution. Although ChPT does not always give sufficient prediction for kaon decays dominated by the $O(p^6)$ or the higher order contributions, calculation of the higher order terms are proceeding at a reasonable rate. Therefore, experimental information of the higher order terms is useful to construct ChPT. If we can calculate the higher order contributions, the predictions of ChPT becomes more reliable. In case of the decay $K_L \to e^+e^-\gamma\gamma$, the amplitude is dominated by $O(p^6)$ contribution [5, 12]. In addition to $O(p^6)$ contribution, it also has the $O(p^8)$ contribution [13, 14]. Therefore, this decay is interesting and deserves an attention in the framework of ChPT.

The long distance contribution has traditionally been calculated by using various models, such as a vector meson resonance model. Recently, it also became possible to interpret the models in the frame of ChPT, too. Therefore, ChPT is becoming a standard model of the long distance contribution.

In consequence, each kaon decay is interesting in its own right because it yields information on the long distance contribution. In some case, a detailed understanding of the long distance contribution is also necessary in the analyses of other modes in which we look for CP violation, measure KM angles, or a search for new physics.

1.1.2 CP Violation

Kaon decays trigger off the idea of Parity (P) violation in the weak interaction where Parity is an operator to reverse the coordinate axes. Simultaneously, a violation of Charge conjugation (C) is found in the weak interaction where Charge conjugation is an operator to exchange a particle with the anti-particle. Although the combined operation CP should be a good symmetry in the weak interaction, it was discovered to be violated in a kaon decay.

The small violation of CP has been only seen in the neutral kaon system. Under the conservation of CP in the weak interaction, the neutral kaon would exist as the CP eigenstates: CP even state (K_1) and CP odd state (K_2). K_1 should decay to the CP even state, such as two pions ($\pi\pi$) , while K_2 should decay to the CP odd states, such as three pions ($\pi\pi\pi$) [15, 16]. Because of the larger phase space for the $\pi\pi$ final states, the K_1 would have a much shorter lifetime than the K_2. However, the long-lived kaon, supposedly K_2, was found to decay $\pi^+\pi^-$ of a wrong CP eigenstate and violates CP. This phenomena is interpreted that the long-lived kaon is actually a mixture of the CP eigenstates, $|K_L\rangle \sim |K_2\rangle + \varepsilon|K_1\rangle$ where ε is the parameter of the CP violation.

In the standard model, two kinds of CP violation are predicted. The simple diagram for the explanation of both types of CP violation is shown in Figure 1.2.

One is referred to as the indirect CP violation which causes the decay εK_1(CP even) $\rightarrow$ (CP even state). The indirect CP violation is observed in some kaon decays, such as $K_L \rightarrow \pi^+\pi^-$, $K_L \rightarrow 2\pi^0$, and the charge asymmetry of $K_L \rightarrow \pi^\pm e^\mp \nu$. The indirect CP violation is represented by only one parameter, ε, for all these decay modes, where $|\varepsilon| = (2.27 \pm 0.02) \times 10^{-3}$.

The other is referred to as the direct CP violation which causes the decay K_2(CP odd) $\rightarrow$ (CP even state). In contrast to the indirect CP violation, the parameter of the direct CP violation depends on the decay mode. The status of the direct CP violation is not clean at this moment, because the direct CP violation has been confirmed by one experiment [17] but it has never been confirmed by other experiment [18]. In addition, there is other theory [19] which does not predict the direct CP violation. Therefore, a search for the direct CP violation and a measurement of the parameter of the direct CP violation is a very attractive physics.

In the framework of standard model, the CP violation arises from a single imag-

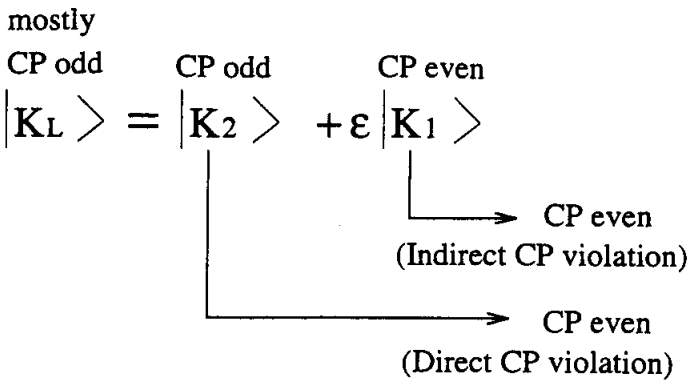

Figure 1.2: The simple diagram for the explanation of both direct and indirect CP violation on K_L.

inary phase η in the KM matrix [2, 3, 9]. Therefore, the measurement of the CP violation can determine the parameter η in the KM matrix.

In order to measure the direct CP violation, we have some desirable neutral kaon decays, such as $K_L \to 2\pi^0$, $K_L \to \pi^+\pi^-$, $K_L \to \pi^0 e^+ e^-$, $K_L \to \pi^0 \mu^+ \mu^-$, and $K_L \to \pi^0 \nu\overline{\nu}$ [2, 3, 9]. For the first two decay modes, the direct CP violation is searched for and is in a confusing situation as mentioned previously, while the last three decays have never been observed yet.

1.2 $K_L \to e^+e^-\gamma\gamma$ Decay

Among many kaon decays, a $K_L \to e^+e^-\gamma\gamma$ decay is an interesting decay to study the physics described in Section 1.1. The $K_L \to e^+e^-\gamma\gamma$ decay is a probe to see the long distance contribution and to test the ChPT at the higher order. In addition, the decay $K_L \to e^+e^-\gamma\gamma$ helps to see the long distance contribution in other decays, such as $K_L \to e^+e^-\gamma$. The $K_L \to e^+e^-\gamma\gamma$ also helps to see the effect of CP violation in the decay $K_L \to \pi^0 e^+ e^-$. In spite of the rich physics, the $K_L \to e^+e^-\gamma\gamma$ decay have never been well studied because of the low branching ratio ($= (6.6 \pm 3.2) \times 10^{-7}$).

We should understand a process of the decay $K_L \to e^+e^-\gamma\gamma$. For the decay $K_L \to e^+e^-\gamma\gamma$, there are following two processes in the standard model. One process is that the decay $K_L \to e^+e^-\gamma\gamma$ can arise from the decay $K_L \to e^+e^-\gamma$ with internal bremsstrahlung. The other process is that $K_L \to e^+e^-\gamma\gamma$ can arise by the direct emission contribution where the intermediate state is the decay $K_L \to \gamma\gamma\gamma$. Since the origins of these two processes are quite different, these processes are described separately in the first two sections.

K_L decays offer a potentially fruitful way to look for new particles that might arise naturally in some of the extension of the standard model. The advantage

of the K_L systems is, of course, its long life time. In addition, the K_L systems have a sensitivity to exotic particles strongly coupled to strangeness. The decay $K_L \to e^+e^-\gamma\gamma$ can have contributions from exotic particles, such as a Higgs-like particle, which can give rise to the decay $K_L \to e^+e^-\gamma\gamma$. We discuss this possibility in Section 1.2.3

The $K_L \to e^+e^-\gamma\gamma$ events have been observed in only one experiment [20], so far. We summarize the result of the previous experiment in Section 1.2.4.

Then, the effect from the decay $K_L \to e^+e^-\gamma\gamma$ to the CP violating decay $K_L \to \pi^0e^+e^-$ is described in Section 1.2.5. In that section, a brief introduction to the decay $K_L \to \pi^0e^+e^-$ is described at first. Then, the decay $K_L \to e^+e^-\gamma\gamma$ is discussed as a serious background for the decay $K_L \to \pi^0e^+e^-$.

Finally, we summarize the above descriptions in Section 1.2.6.

1.2.1 Radiative Dalitz $K_L \to e^+e^-\gamma\gamma$ Decay

Just as π^0 Dalitz decay, ($\pi^0 \to e^+e^-\gamma$), neutral kaon also has its own Dalitz decay, $K_L \to e^+e^-\gamma$. Thus, a $K_L \to e^+e^-\gamma\gamma$ process from the decay $K_L \to e^+e^-\gamma$ with internal bremsstrahlung is referred to as the radiative K_L Dalitz decay. This process has the largest contribution to the decay $K_L \to e^+e^-\gamma\gamma$. The origin of this process is the decay $K_L \to \gamma\gamma^*$ which gives useful information about the long distance contribution.

At first, we discuss the physics of $K_L \to \gamma\gamma^*$. The decay $K_L \to \gamma\gamma^*$ can arise from both short and long distance contributions shown in Figure 1.1. As far as we know, the decay $K_L \to \gamma\gamma$ is dominated by the long distance contribution [5]. In ChPT, the decay $K_L \to \gamma\gamma$ is dominated by $O(p^6)$ contribution. Therefore, the prediction for the branching ratio of this decay is very uncertain, which is $BR(K_L \to \gamma\gamma) \sim 10^{-4}$ in ChPT [4], whereas a measured value is $BR(K_L \to \gamma\gamma) = (5.7 \pm 0.27) \times 10^{-4}$ [21]. Therefore, the experimental value of the $K_L \to \gamma\gamma$ branching ratio is used for the prediction of the $K_L \to e^+e^-\gamma\gamma$ decay. The structure of the decay $K_L \to \gamma\gamma^*$ is more interesting, since the prediction for a $K_L\gamma^*\gamma$ vertex is more reliable than the $K_L \to \gamma\gamma$ branching ratio and gives more useful information about the long distance contribution. This information is derived from a energy spectrum of γ^* in the $K_L\gamma^*\gamma$ vertex, which is observed as a di-lepton mass ($M_{l^+l^-}$) spectrum in experiments. Knowledge of this long distance contribution is a key to solve the origin of the $\Delta I = \frac{1}{2}$ rule [22], and it is a key to derive the parameter ρ in KM matrix from the decay $K_L \to \mu^+\mu^-$ [9]. The probe to see the $K_L\gamma^*\gamma$ structure are decays $K_L \to e^+e^-\gamma$, $K_L \to e^+e^-\gamma\gamma$, or $K_L \to \mu^+\mu^-\gamma$.

Currently, the decay $K_L \to e^+e^-\gamma$ gives the most precise result for the $K_L\gamma^*\gamma$ structure. Let us discuss the decay $K_L \to e^+e^-\gamma$ as an example of the probes to see the structure. Generally, the differential decay spectrum for $K_L \to e^+e^-\gamma$ is [23]

$$\Gamma_{\gamma\gamma}^{-1}\frac{d\Gamma}{dx} = \frac{2\alpha_{QED}}{3\pi}\frac{(1-x)^3}{x}[1+\frac{2m_e^2}{xm_{K_L}^2}] \times [1-\frac{4m_e^2}{xm_{K_L}^2}]^{1/2} \times |f(x)|^2,$$

where $x = m_{ee}^2/m_{K_L}^2$ and the $f(x)$ is a form factor that parameterizes the dynamics of the $K_L\gamma^*\gamma$ vertex. The general parameterization of this form factor by Bergström, Massó, and Singer [22] is:

$$f(x) = \frac{1}{1-0.418x} + \frac{C\alpha_{K^*}}{1-0.311x} \times[\frac{4}{3} - \frac{1}{1-0.418x} - \frac{1}{9(1-0.405x)} - \frac{2}{9(1-0.238x)}]. \quad (1.1)$$

This form factor assumes vector-meson dominance of the photon coupling. The form factor is represented by the Feynman diagrams in Figure 1.3. The first term

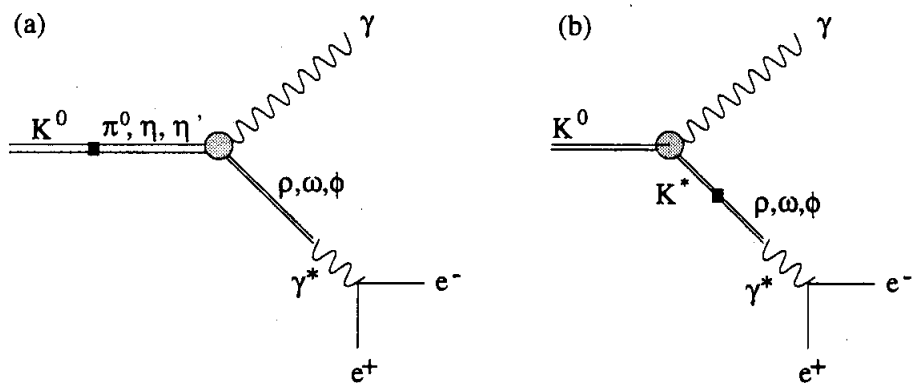

Figure 1.3: Feynman diagrams for the $K_L \to e^+e^-\gamma$ form factor are shown. The Feynman diagram (a) represents the first term in Equation 1.1, and the diagram (b) represents the second one in Equation 1.1.

represent the coupling of ρ, ω, and ϕ to the psedoscalars π^0, η, and η'. The second term represents the coupling of ρ, ω, and ϕ to K^*. A dimensionless parameter, C, is a combination of known coupling constants with the value $C = 2.5$. The dimensionless parameter α_{K^*} characterizes the strength of the vector-vector weak interaction (the second term) relative to the psedoscalar-psedoscalar interaction (the first term). This theory predicts the form factor through the above virtual meson contributions. The theory predicts the value of the form factor $|\alpha_{K^*}| = 0.2 \sim 0.3$. There is also other theory to describe a similar decay $K_L \to \mu^+\mu^-\gamma$ that predicts the similar form factor which corresponds to the above form factor with the parameter $\alpha_{K^*} = -0.31^{+0.08}_{-0.03}$ [24] [1]. The latter theory claims that another important contribution shown in Figure 1.4 should be included to the former theory, so that the form factor would be enhanced.

The measured value of α_{K^*} is -0.28 ± 0.08, which agrees with both theoretical predictions. However, a recent measurement of the muonic Dalitz decay

[1]This theory does not give a prediction for a $K_L \to e^+e^-\gamma$ form factor. However, it should be same as the $K_L \to \mu^+\mu^-\gamma$ form factor in principle.

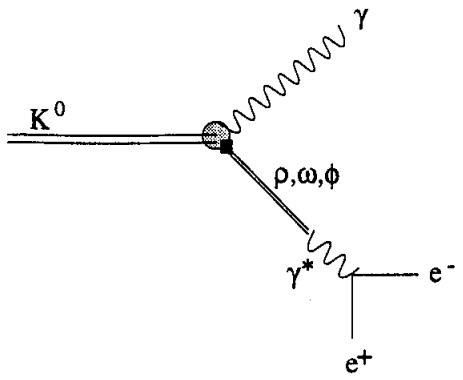

Figure 1.4: An additional Feynman diagram for the $K_L \to e^+e^-\gamma$ form factor is shown.

$K_L \to \mu^+\mu^-\gamma$ gives $\alpha_{K^*} = -0.018^{+0.131}_{-0.123}$ [25]. It disagrees with the latter theoretical prediction [22], but agree with the former prediction [23] within the error. Thus, the study of the form factor is inconclusive and further experimental results are necessary.

One of the possible sources which causes the above inconsistency is a radiative correction. The radiative correction is larger for the decay $K_L \to e^+e^-\gamma$ than to the decay $K_L \to \mu^+\mu^-\gamma$ because of the lighter mass of the electron. For this radiative correction, the BNL experiment E845, which is the most sensitive experiment to measure this form factor, reported that the measured form factor of $\alpha_{K^*} = -0.28^{+0.099}_{-0.090}$ changes its value to -0.18 ± 0.077 if the radiative correction is not included [26]. There are two reasons why α_{K^*} depends on the radiative correction. One is due to the disturbance to M_{ee} spectrum shown in Figure 1.5. Since expected M_{ee} spectrum depends on whether the radiative correction is included or not, the comparison between the measured quantity and the expected one depends on the correction, too. The other is caused by loosing the $K_L \to e^+e^-\gamma$ signal because there was an extra γ from its radiative decay, $K_L \to e^+e^-\gamma\gamma$.

In order to resolve the inconsistency mentioned previously, more precise measurements of the $K_L \to e^+e^-\gamma$ and $K_L \to \mu^+\mu^-\gamma$ form factor are necessary, which requires a good understanding of the radiative effects, $K_L \to e^+e^-\gamma\gamma$. Hence, I want to emphasize that the measurement of the $K_L \to e^+e^-\gamma\gamma$ form factor cast important information on this subject.

The matrix element of the radiative Dalitz decay was calculated by K. O. Mikaelian and J. Smith based on the Feynman diagrams shown in Figure 1.6 [27, 28]. Based on the $K_L \to \gamma\gamma$ branching with the above matrix element, the $K_L \to e^+e^-\gamma\gamma$ branching ratio was predicted to be 5.8×10^{-7} with the minimum photon energy cutoff of 5 MeV in the center of mass frame of the kaon [1]. We should verify the prediction by experiments because the real $K_L \to e^+e^-\gamma\gamma$ decay has the effects of the form

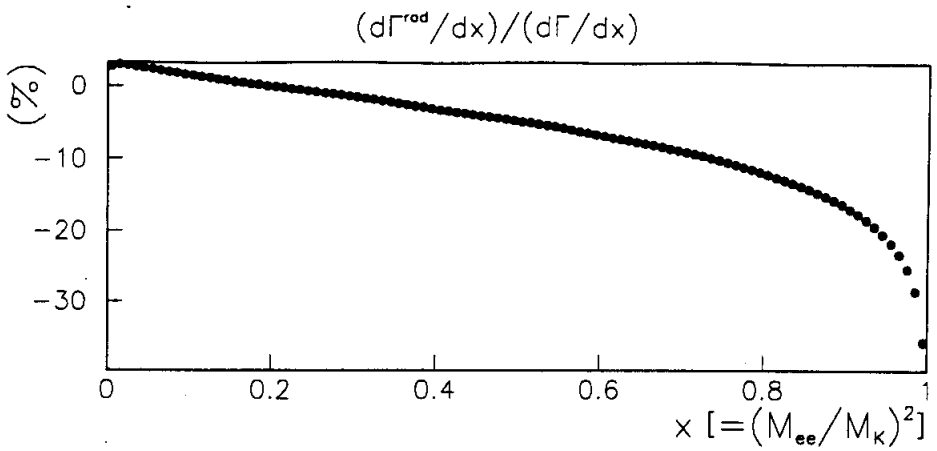

Figure 1.5: Expected effect of the radiative correction to the differential $K_L \to e^+e^-\gamma$ decay spectrum, $(d\Gamma^{rad}/dx)/(d\Gamma/dx)$.

factor shown in Figure 1.3 and Figure 1.4 which would change the prediction.

1.2.2 Direct Emission $K_L \to e^+e^-\gamma\gamma$ Decay

The decay $K_L \to e^+e^-\gamma\gamma$ can come from another process which is the decay $K_L \to \gamma\gamma\gamma^*$ with internal conversion. This decay is referred to as the direct emission $K_L \to e^+e^-\gamma\gamma$ decay. This decay is an unique process to test the amplitude and the structure of the $K_L\gamma^*\gamma\gamma$ vertex. In order to understand this aspect of $K_L \to e^+e^-\gamma\gamma$ process, we start from the decay $K_L \to \gamma\gamma\gamma$ at first where all photons are real. Then, we move on to the description of the decay $K_L \to \gamma\gamma\gamma^*$ where one photon is virtual. Finally, we discuss the decay $K_L \to e^+e^-\gamma\gamma$ through the decay $K_L \to \gamma\gamma\gamma^*$.

The decay $K_L \to \gamma\gamma\gamma$

The decay $K_L \to \gamma\gamma\gamma$ is not forbidden by any selection rules or any symmetry principles. At this point, it becomes important to consider normally forbidden process. Naively, we would imagine that the decay $K_L \to \gamma\gamma\gamma$ would occur at rates that are roughly a factor α_{QED} times the $K_L \to \gamma\gamma$ decay rate, $BR(K_L \to \gamma\gamma\gamma) \sim 4.2 \times 10^{-6}$ [29].

However, this naive expectation disregards the constraints of gauge invariance and Bose statistics. Gauge invariance dictates that in the decay $K_L \to \gamma\gamma\gamma$ no pair of photons can have angular momentum zero, since that would correspond to a $0 \to 0$ radiative transition, which is forbidden for a real photon. Similarly, no pair of photons can have $J = 1$, since that conflicts with Bose statistics. It follows that the

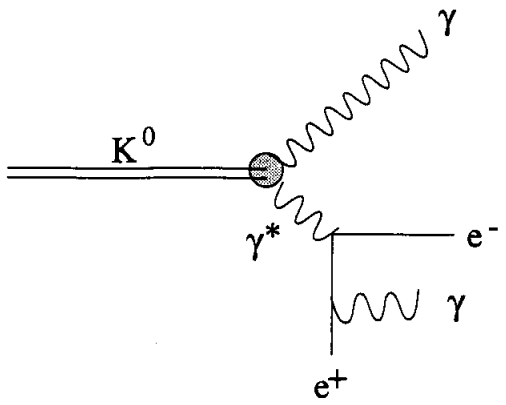

Figure 1.6: Feynman diagrams of the radiative Dalitz $K_L \to e^+e^-\gamma\gamma$ decay. The $K_L \to \gamma\gamma^*$ vertex is offered by the experimental value of the $K_L \to \gamma\gamma$ branching.

decay $K_L \to \gamma\gamma\gamma$ can only occur with at least two units of angular momentum. This gives rise to an extraordinary suppression. A prediction of the $K_L \to \gamma\gamma\gamma$ branching ratio is $BR(K_L \to \gamma\gamma\gamma) \sim 3 \times 10^{-19}$ with a simple model [29]. This prediction is far smaller than the sensitivity in experiments.

The decay $K_L \to \gamma\gamma\gamma^*$

In contrast to the decay $K_L \to \gamma\gamma\gamma$, the decay $K_L \to \gamma\gamma\gamma^*$ has no suppressions by gauge invariance and Bose statistics because there is a massive virtual photon. Therefore, we can expect the larger $K_L \to \gamma\gamma\gamma^*$ branching ratio than that of $K_L \to \gamma\gamma\gamma$ [30], or we would naively expect the branching ratio, $BR(K_L \to \gamma\gamma\gamma^*) \sim 4.2 \times 10^{-6}$.

The decay $K_L \to e^+e^-\gamma\gamma$ through the decay $K_L \to \gamma\gamma\gamma^*$

The decay $K_L \to \gamma\gamma\gamma^*$ would be observed as a decay $K_L \to e^+e^-\gamma\gamma$. The branching ratio of $K_L \to e^+e^-\gamma\gamma$ by the $K_L\gamma^*\gamma\gamma$ vertex is naively expected to be $BR(K_L \to e^+e^-\gamma\gamma) \sim \alpha_{QED} \times BR(K_L \to \gamma\gamma\gamma^*) \sim 3.1 \times 10^{-8}$. In addition to this naive expectation, we have some rough predictions for this decay by assuming some models.

In ChPT, this process starts at $O(p^8)$ contributions. There are mainly three kinds of $O(p^8)$ contributions, which are shown in Figure 1.7. The current ChPT or any theories do not give a certain prediction for these contributions, but they can give rough estimation. For the $O(p^8)$ contributions, there are some anomalous vertexes: $K_L - \gamma^* S^{*\,++}$, $K_L - \gamma^* P^{*\,--}$, and $K_L - \gamma V^{*\,++}$ vertexes in the decay where S^{++} is a scalar (0^{++}) state, P^{--} is a CP-even Psuedoscalar (0^{--}, e.g. K_S) state, and V^{++} is a C-even Axial-vector state. These contributions are suppressed compared to the

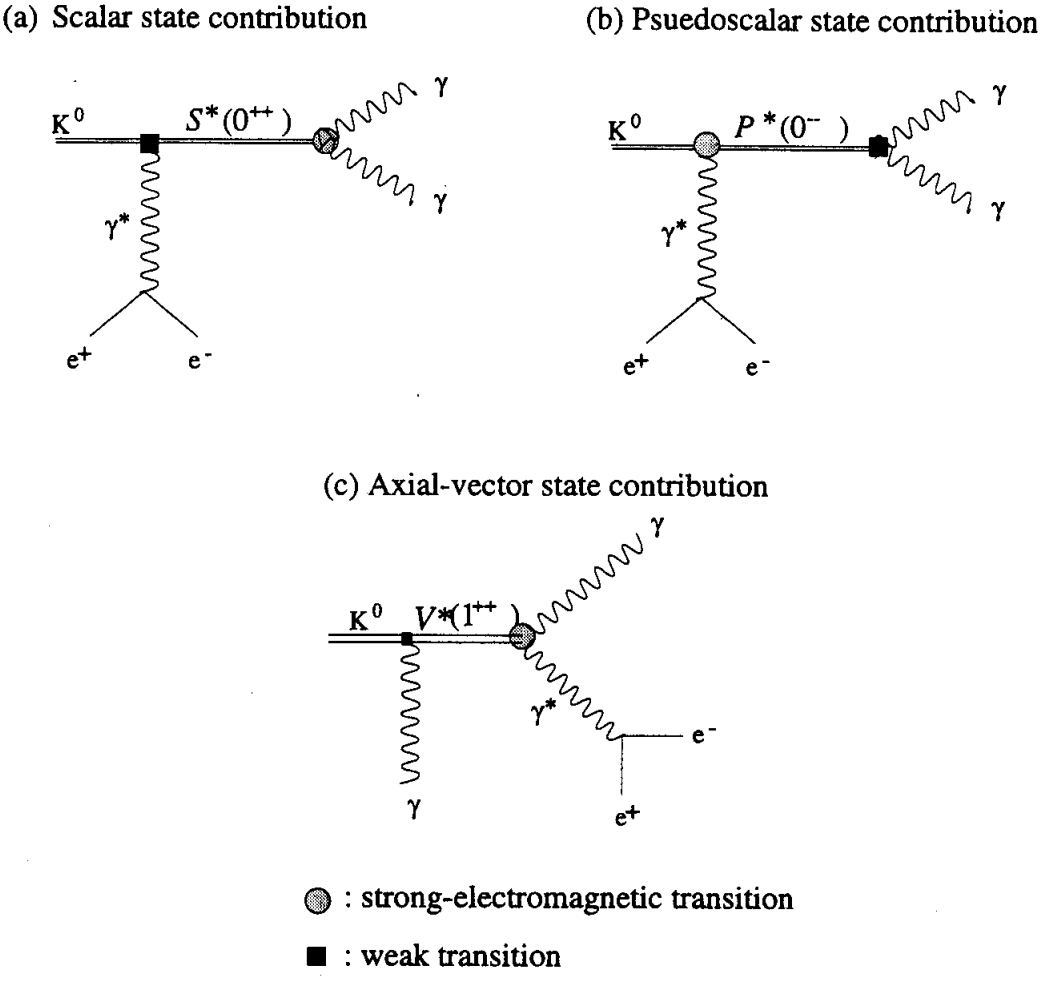

Figure 1.7: Feynman diagrams of the $K_L \to e^+e^-\gamma\gamma$ decay through $K_L \to \gamma\gamma\gamma^*$. The Scalar state contribution (a), psuedoscalar state contribution (b), axial-vector state contribution (c) are shown.

radiative K_L Dalitz decay by power counting of $O(p^8)$ versus to $O(p^6)$ and by lack of pole for $E_{\gamma^*} = 0$. This suppression is about a factor of $10^{-3} \sim 10^{-4}$ [13, 14]. In consequence, the order of the amplitude from these contributions is expected to be around 10^{-10}.

In addition to the above main contributions, the small CP-violating contribution would be expected in ChPT from the CP-violating $K_L \to (\pi^{0\,*}, \eta^*, \eta'^*)\gamma^* \to e^+e^-\gamma\gamma$ process. Because of the off-shell $\pi^{0\,*}, \eta^*, \eta'^* \to \gamma\gamma$ process, this process suppressed by a factor of 10^{-7} compared to the on-shell process. Therefore the branching ratio of the CP-violating $K_L \to e^+e^-\gamma\gamma$ would be so small ($10^{-17} \sim 10^{-18}$) [13] that we can neglect this contribution.

Besides ChPT, other model predicts the decay $K_L \to e^+e^-\gamma\gamma$ by a K_L charge radius contribution. Since a K_L have a small charge radius, where a $d-(\overline{d}-)$quark rotaes around a $\overline{s}-(s-)$quark, a transition from K_L to K_S with a virtual radiative photon is allowed. A typical example of these decays is $K_L \to \pi\pi e^+e^-$ where there is a decay chain $K_L \to K_S\gamma^* \to \pi\pi e^+e^-$ [31, 32]. From this contribution, the $K_L \to e^+e^-\gamma\gamma$ branching ratio is expected to be $\sim (10^{-13} \sim 10^{-15})$ by scaling the $K_L \to \pi\pi e^+e^-$ predictions [31, 32]. In fact, this contribution is same as the $O(p^8)$ CP-even Psuedoscalar contribution in ChPT.

In addition to the long distance contribution, the $K_L \to e^+e^-\gamma\gamma$ would have a contribution from the short distance effect. However, this contribution has not been calculated yet.

Although direct emission contributions for $K_L \to e^+e^-\gamma\gamma$ is smaller than the radiative Dalitz contribution, the interference between these two contributions would raise the effect of the direct emission contribution. Also it would be helpful to look into kinematical regions where the radiative Dalitz contribution is suppressed.

1.2.3 $K_L \to e^+e^-\gamma\gamma$ Outside of the Standard Model

There is another interesting contribution to the $K_L \to e^+e^-\gamma\gamma$ decay, which is a Higgs or Higgs-like (spin 0) particle (H) with the short life time. Here, a $H \to \gamma\gamma$ search is interesting since the virtual loop of heavy top quark would enhances this mode. We can search for the decay $K_L \to H(\gamma^*, \rho^*, \omega^*, \phi^*) \to He^+e^-$. Assuming the short life time of H ($\leq 5 \times 10^{-12}$ sec), H decays to $\gamma\gamma$ within 1 m from the K_L decay vertex in our experiment.

As for a Higgs particle, a standard model Higgs particle lighter than 60 GeV is excluded by LEP data, so the interest will have to focus on various extensions of the minimal Higgs sector. In two-doublet models there generally exists a neutral pseudoscalar Higgs. In supersymmetric models such a light Higgs is always accompanied by an even lighter scalar Higgs, so this scenario is ruled out by LEP. In the general two-doublet case, there is no such relation between the masses so that Z^0 data are less restrictive since the pseudoscalar Higgs does not couple directly to the Z^0. By same reasons, the excluded mass region by various particle decays depends sensitively on variety of theoretical assumptions and so it is important to derive

limits from as many sources as possible.

In kaon decays, Higgs ($H \to \gamma\gamma$) search was carried out in various decay modes, such as decays $K_L \to \pi^0\gamma\gamma$ and $K^+ \to \pi^+\gamma\gamma$. In $K^+ \to \pi^+\gamma\gamma$ decay, the upper limit on the branching ratio, $BR(K^+ \to \pi^+ H, H \to \gamma\gamma) < 10^{-7}$, gave a lower limit of 80 MeV/c^2 [33] on the mass of H. In $K_L \to \pi^0\gamma\gamma$ decay, the measured branching ratio at the mass range of $M_{\gamma\gamma} \geq 280 MeV/c^2$ is three times larger than the predition by ChPT [34]. The large $K_L \to \pi^0\gamma\gamma$ branching ratio could be due to a new physics.

The study of the decay $K_L \to e^+e^-\gamma\gamma$ is sensitive to such an exotic decay $K_L \to He^+e^-, H \to \gamma\gamma$ with a wide mass range of $30 < M_{\gamma\gamma}(MeV/c^2) < 400$.

1.2.4 Observed $K_L \to e^+e^-\gamma\gamma$ Events

So far, only one experiment, BNL experiment E845, observed the decay $K_L \to e^+e^-\gamma\gamma$ at the 2σ confidence level. The small branching ratio of the decay, $BR(K_L \to e^+e^-\gamma\gamma) \sim 6 \times 10^{-7}$, has prevented the detailed study of this decay so far. BNL E845 observed 30 $e^+e^-\gamma\gamma$ events with 13.28 ± 5.93 background events. Based on these numbers, they concluded that they observed 16.72 ± 8.07 $K_L \to e^+e^-\gamma\gamma$ events, and deduced the branching ratio to be $(6.6 \pm 3.2) \times 10^{-7}$. Although this result is consistent with the theoretical prediction of the radiative K_L Dalitz decay [1] within the error, they give no information for $K_L \to e^+e^-\gamma\gamma$ kinematics.

1.2.5 Backgrounds to $K_L \to \pi^0e^+e^-$

The decay $K_L \to \pi^0e^+e^-$ is an attractive decay mode as a window to search for the direct CP violation. The final state of the decay $K_L \to \pi^0e^+e^-$ has both kinds of CP eigenstate, either even or odd, which depends on the intermediate state. The process $K_L \to \pi^0\gamma^* \to \pi^0e^+e^-$ has the CP even final state, while $K_L \to \pi^0\gamma^*\gamma^* \to \pi^0e^+e^-$ has the CP odd final state. In addition, the intermediate states π^0Z^* and $\pi^0W^*W^*$ contribute to the CP even final state. Since a K_L is the mixture of two CP eigenstates, there are two kinds of CP violation: indirect CP violation and direct CP violation. In consequence, the $K_L \to \pi^0e^+e^-$ decay has three kinds of contribution which are direct CP violating, indirect CP violating and CP conserving. Among these contributions, the direct CP violating amplitude is expected to be as large as, or larger than other contributions. A prediction for each contribution is shown in Table 1.1.

The most sensitive search for $K_L \to \pi^0e^+e^-$ is achieved in our experiment E799 which set the upper limit of 4.3×10^{-9} ($90\% C.L.$) [38, 39]. Since this decay mode has a great possibility to observe the direct CP violation, the next generation of $K_L \to \pi^0e^+e^-$ experiment, KEK E162 [40] and FNAL KTeV [41] aim for the single event sensitivity of 10^{-10} and 10^{-11}, respectively.

Unfortunately, the formidable background to the $K_L \to \pi^0e^+e^-$ at the sensitivity of the standard model was found, which is the decay $K_L \to e^+e^-\gamma\gamma$. The level of the $K_L \to e^+e^-\gamma\gamma$ background to the decay $K_L \to \pi^0e^+e^-$ was studied theoretically,

Table 1.1: The expected $K_L \to \pi^0 e^+ e^-$ branching ratio and the lower limit of the expected $K_L \to e^+ e^- \gamma\gamma$ background level.

Mode	The expected branching ratio
$K_L \to \pi^0 e^+ e^-$ (direct CP-violating)	$1 \sim 62 \times 10^{-12}$ [12, 35, 36, 37]
$K_L \to \pi^0 e^+ e^-$ (indirect CP-violating)	$\leq 1.27 \times 10^{-12}$ [9, 12]
$K_L \to \pi^0 e^+ e^-$ (CP-conserving)	$0.01 \sim 4.1 \times 10^{-12}$ [35, 36, 37]
$K_L \to e^+ e^- \gamma\gamma$ with $M_{\gamma\gamma} = M_{\pi^0} \pm 5$MeV	22×10^{-12}

and the lower limit was found to be about 2.2×10^{-11} with a π^0 mass cut of ± 5 MeV/c^2 [1]. This background level is listed in Table 1.1 with the prediction of $K_L \to \pi^0 e^+ e^-$. Apparently, the contribution of this background is far larger than the contributions from both indirect CP violating and CP conserving process.

The $K_L \to e^+ e^- \gamma\gamma$ background contribution can be larger than the expectation of the decay $K_L \to \pi^0 e^+ e^-$. Therefore, the measurement of the background level of the decay $K_L \to e^+ e^- \gamma\gamma$ and the study of the decay kinematics are quite important in order to separate them from the direct CP violation in $K_L \to \pi^0 e^+ e^-$.

1.2.6 Summary

As mentioned above, physics in the decay $K_L \to e^+ e^- \gamma\gamma$ is very rich. The theoretical study for this decay is progressing remarkably [13, 14], but it is not conclusive yet. In addition, the experimental information was limited before this experiment.

In this thesis, we present the most precise measurement of the branching ratio of the decay $K_L \to e^+ e^- \gamma\gamma$ and the first observation of some kinematic variables, such as M_{ee}, $M_{\gamma\gamma}$, and etc.. Although there were not enough statistics to derive the $K_L \to e^+ e^- \gamma\gamma$ form factor, this measurement would help to measure the $K_L \to e^+ e^- \gamma$ form factor more precisely. In addition, we also set the constraint for the direct emission process and the process from the new physics in this decay. We also study the $K_L \to e^+ e^- \gamma\gamma$ background level in a search for the decay $K_L \to \pi^0 e^+ e^-$.

This result was already published on Physical Review Letter [42].

1.3 Overview

Physics and motivation of the decay $K_L \to e^+ e^- \gamma\gamma$ are discussed in this Chapter. The general introduction and a quick tour of our experiment, E799, are given in Chapter 2 with the detailed description of the detector. The Monte Carlo simulation is described in Chapter 3. Event selection and the technique for the measurement

of the branching ratio are described in Chapter 4 and 5, respectively. In Chapter 6, a search for the direct emission $K_L \to e^+e^-\gamma\gamma$ process and a search for the effect outside of the standard model are described. In addition, the $K_L \to e^+e^-\gamma\gamma$ background level for the decay $K_L \to \pi^0 e^+e^-$ are also studied in Chapter 6. At the end, the results and the conclusions are given and discussed in Chapter 7.

Chapter 2

Experiment and Detector

The principal goal of Fermilab experiment E799 was to search for the rare decay $K_L \to \pi^0 e^+ e^-$. In addition, many other multi-body rare K_L decays were studied. In Section 2.1, the overview of E799 experiment, and a brief introduction of the detector are given. In Section 2.2, the K_L beam production is described. The detailed description of principal components of the detector is given in Section 2.3. The trigger requirement is described in Section 2.4, and the data acquisition system is described in Section 2.5. Finally in Section 2.6, some special run, such as a calibration run, is described.

2.1 Rare K_L Decay Experiment, E799

This experiment was carried out at the Meson Center beamline at Fermilab from October, 1991 to January, 1992. The detector of E799 was optimized for the rare K_L decay experiment based on the detector of Fermilab experiment E731, whose aim was the measurement of the direct CP violation parameter, ϵ'/ϵ [18].

Two nearly parallel K_L beams were produced by an 800 GeV proton beam that struck a beryllium target. After collimation the neutral beams entered the detector volume where decays were selected in the interval between 90 and 160 m from the target. The schematic view of the detector is shown in Figure 2.1. The trajectories and momenta of charged tracks were measured with a spectrometer composed of four drift chambers and an analyzing magnet with a nominal transverse momentum kick of 200 MeV/c. The momentum resolution was $(\sigma_p/p)^2 = (5 \times 10^{-3})^2 + \{1.4 \times 10^{-4} \times [p(\mathrm{GeV}/c)]\}^2$. The energy and position of electrons and photons were measured with a lead-glass calorimeter composed of 804 blocks arranged in a circular array of 1 m radius with two beam holes in the center to allow the passage of the neutral kaon beams. Each block in the array was $(5.8\ \mathrm{cm})^2 \times 18.7$ radiation lengths deep. The energy resolution for electrons was typically 4.4% for this data sample. The detector had two scintillator hodoscopes between the downstream end of the spectrometer and the calorimeter, which were used for triggering. The detector also had a photon veto system used to reject events in which photons missed the calorimeter. At the

Table 2.1: Decay modes of the kaon observed in E799

Decay Mode	Interest
$K_L \to \pi^0 e^+ e^-$	CP violation
$K_L \to \pi^0 \mu^+ \mu^-$	CP violation
$K_L \to \pi^0 \nu\overline{\nu}(\pi^0 \to e^+ e^- \gamma)$	CP violation
$K_L \to e^+ e^- \gamma\gamma$	Radiative correction for $K_L \to e^+ e^- \gamma$, Search for $K_L \to \gamma\gamma\gamma^*$, Background of $K_L \to \pi^0 e^+ e^-$
$K_L \to e^+ e^- \gamma$	Form Factor, Normalization mode
$K_L \to \mu^+ \mu^- \gamma$	Form Factor
$K_L \to e^+ e^- e^+ e^-$	Form Factor
$K_L \to 3\pi^0(\pi^0 \to e^+ e^-)$	Unitarity Limit
$K_L \to \pi^0 \mu^\pm e^\mp$	Lepton number violation
$K_L \to 3\pi^0(\pi^0 \to e^\pm \mu^\mp)$	Lepton number violation
$K_L \to \pi^0 \pi^0 \gamma$	Chiral Perturbation Theory
$K_L \to 2\pi^0(\pi^0 \to e^+ e^- \gamma)$	Normalization mode
$K_L \to 3\pi^0(\pi^0 \to e^+ e^- \gamma)$	Normalization mode
$K_L \to \pi^+ \pi^- \pi^0$	Normalization mode
$K_L \to \pi^\pm e^\mp \nu$	Calibration

downstream end of the detector, there were scintillator counters behind a 3 m thick steel in order to tag a muon.

Observable K_L decays in this experiment are listed in Table 2.1. The use of the high energy kaons from an 800 GeV protons allows E799 to have a high acceptance and high energy resolution for a variety of multi-body decays.

Two types of triggers were used for this analysis to accept both $K_L \to e^+ e^- \gamma\gamma$ and $K_L \to e^+ e^- \gamma$ decays. The latter decay mode is used for normalization purpose. Both triggers required two hits in each hodoscope, drift chamber hits consistent with two tracks, and no veto counter hits. In addition, the $K_L \to e^+ e^- \gamma\gamma$ trigger required a minimum total energy of 55 GeV in the calorimeter and four clusters of energy in the calorimeter; each cluster having an energy threshold of 2.5 GeV. Likewise the $K_L \to e^+ e^- \gamma$ trigger demanded a minimum total energy of 6 GeV and three identified clusters. The $K_L \to e^+ e^- \gamma$ trigger was prescaled by 14.

The branching ratio of the decay $K_L \to e^+ e^- \gamma\gamma$ is basically measured by comparing the rate of $K_L \to e^+ e^- \gamma\gamma$ to that of $K_L \to e^+ e^- \gamma$ as shown in Equation 2.1,

$$BR(K_L \to e^+ e^- \gamma\gamma) = \frac{N_{e^+e^-\gamma\gamma}}{A_{e^+e^-\gamma\gamma}} \times \frac{A_{e^+e^-\gamma}}{N_{e^+e^-\gamma}} \times BR(K_L \to e^+ e^- \gamma), \qquad (2.1)$$

where $N_{e^+e^-\gamma\gamma}$ and $N_{e^+e^-\gamma}$ denote the number of observed $K_L \to e^+ e^- \gamma\gamma$ and $K_L \to$

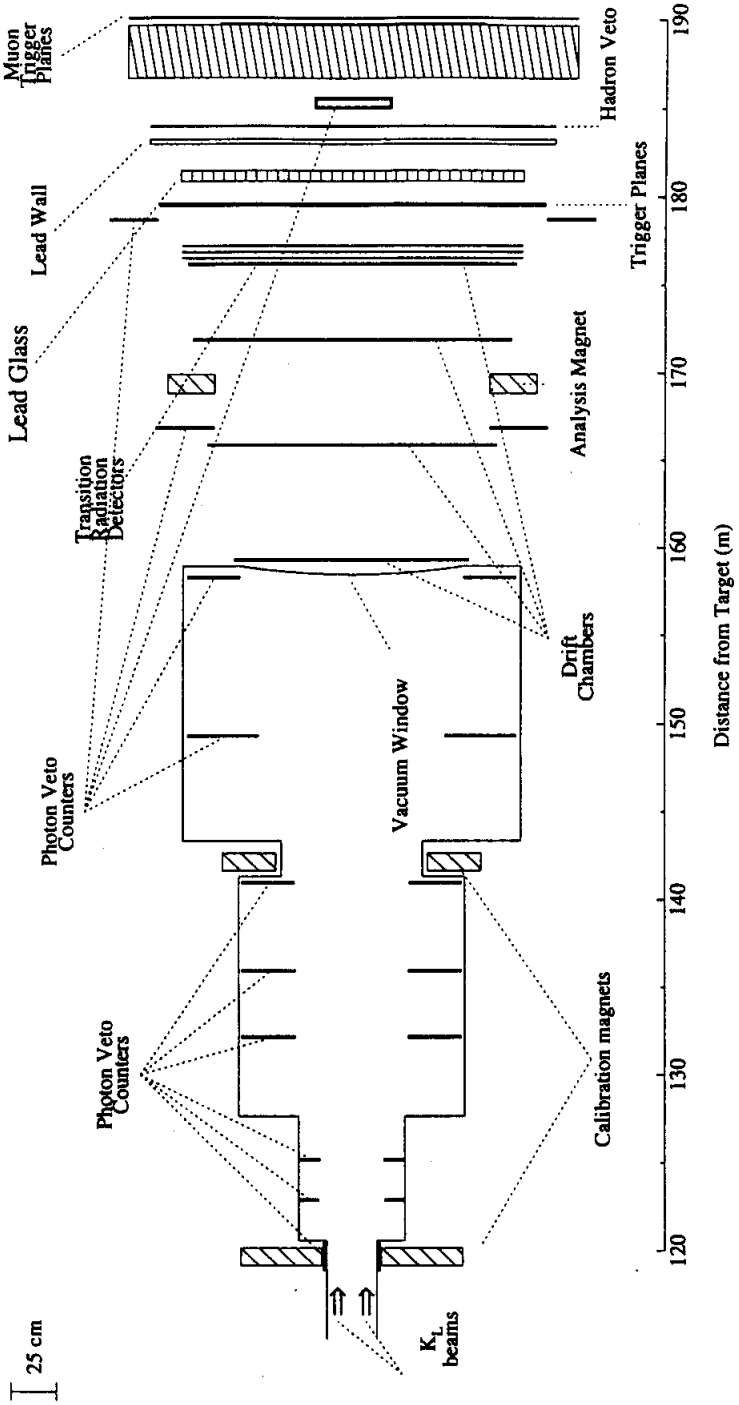

Figure 2.1: The E799 Detector

$e^+e^-\gamma$ decays, respectively, and $A_{e^+e^-\gamma\gamma}$ and $A_{e^+e^-\gamma}$ denote the acceptance of the detector for $K_L \to e^+e^-\gamma\gamma$ and $K_L \to e^+e^-\gamma$ decays, respectively. The $BR(K_L \to e^+e^-\gamma)$ is well known from other experiments, and the world average is $(9.1 \pm 0.5) \times 10^{-6}$ [43]. Since the decay $K_L \to e^+e^-\gamma\gamma$ has the same kinds of final state particles as the decay $K_L \to e^+e^-\gamma$, the efficiency for the trigger and the particle identification are nearly canceled in the ratio of acceptances, $A_{e^+e^-\gamma}/A_{e^+e^-\gamma\gamma}$, in Equation 2.1. The method, normalizing by another decay, is more reliable than normalizing by the absolute kaon flux.

2.2 K_L Beam Production

In the fixed target operation, the Fermilab Tevatron delivered 1.5×10^{12} protons in a 22 seconds spill during a 58 seconds cycle. The 800 GeV protons produce the high energy kaons whose energy spectrum at the target is shown in Figure 2.2. Within a spill, a 2 ns proton bucket per 18.8 ns arrived 10^9 times. This radio frequency (RF) substructure of the Tevatron provided the basic timing information used for the trigger. The amount of protons in each bucket varied by a factor of $2 \sim 5$ from bucket to bucket.

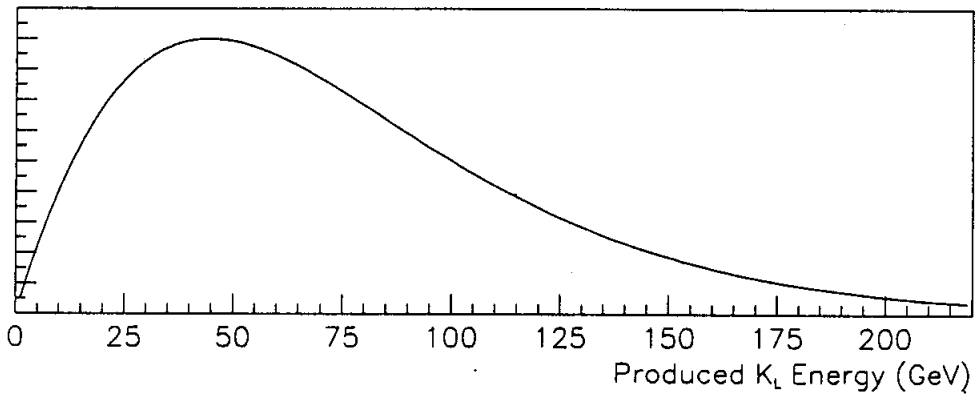

Figure 2.2: The energy spectrum of the kaons at the target.

The beryllium target was 36 cm long with the cross section of 3.2×3.2 mm^2. The profile of the incident proton beam at the target was roughly Gaussian with a width (σ) of 0.4 mm. The targeting angle was chosen to be 4.8 mrad in the horizontal plane in order to get both high kaon flux and good kaon to neutron ratio in the beams. Downstream of the target, there were some collimators, absorbers and sweeping magnets, which are shown in Figure 2.3. These collimators, absorbers and magnets removed charged particles and reduced photons and neutrons in the beams.

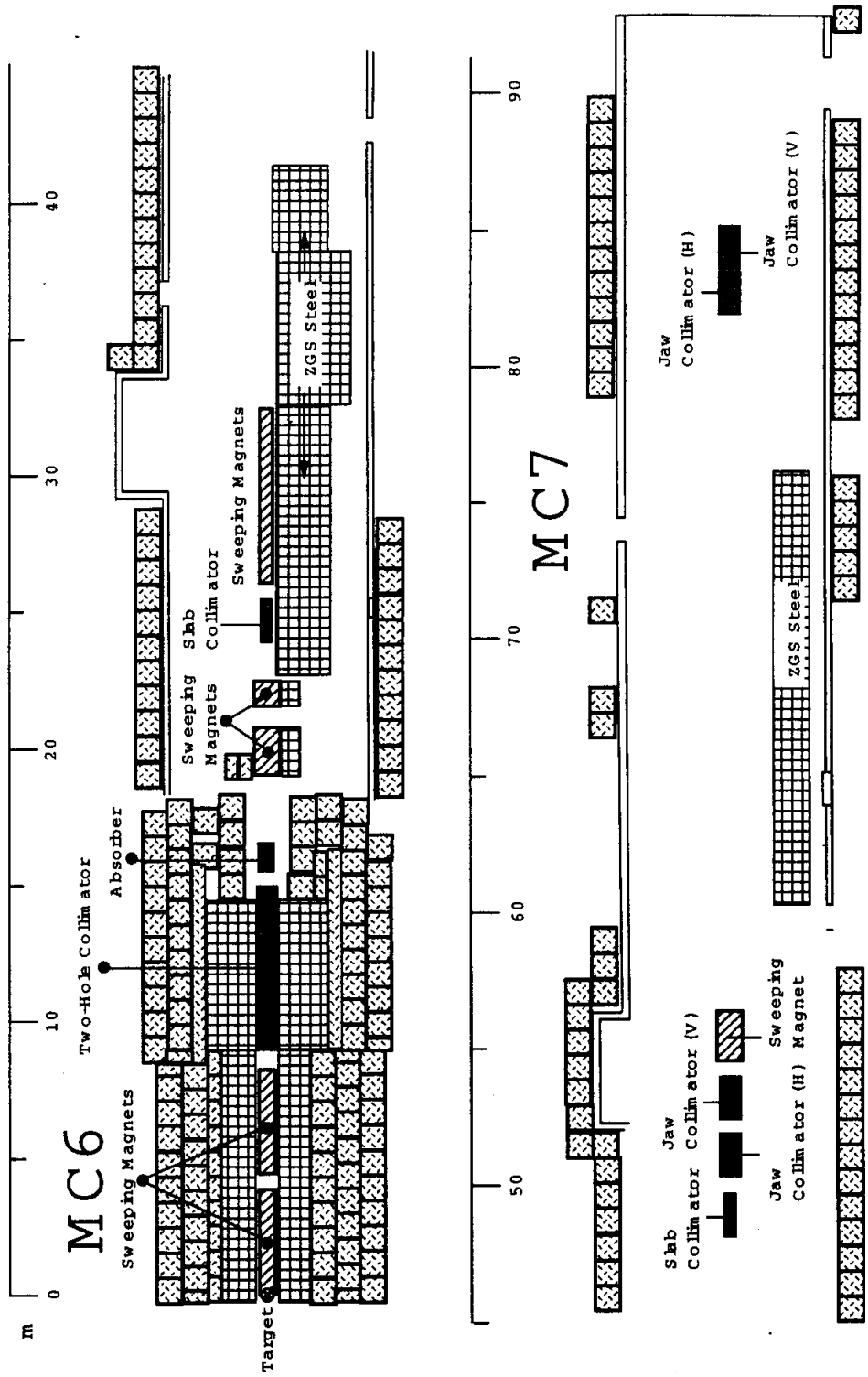

Figure 2.3: The target and collimators formed the beams in $y-$view.

Figure 2.4 shows the schematic picture of the collimation in the horizontal and vertical views. The first collimator began at 9 m downstream of the target, and was made of 5.8 m long copper with two holes, followed by a set of sweeping magnets. The size of the hole was 6.65×6.65 mm^2 each at the upstream end of the collimator, and the center of two holes were located 5.8 mm above and below the target. Additional collimator made of slabs were located 25.5 m and 49.2 m downstream of the target in order to define the inner edges and to eliminate the cross-talk between the two beams. Other two sets of horizontal and vertical collimators located 52 m and 83 m downstream of the target were used to define the outer edges of the beams. A block of 7.5 cm long lead absorber was located just downstream of the two-hole copper collimator.

In order to reduce the interactions of the beam with materials, the beams entered a vacuum region under 15 mTorr. The vacuum region started from 17 m downstream of the target, almost immediately downstream of the beam absorber, and ended at 160 m from the target. The end of the vacuum was sealed by a 1.22 m diameter window, referred to as vacuum window.

In the K_L decay region, the number of neutrons, Λ particles and K_S components were about 4, 5×10^{-4}, and 10^{-8} of the number of K_L, respectively.

2.3 Detector

The locations and dimensions of the individual elements of the detector are listed in Table 2.3, where each detector element is described in the following sections. In this thesis, we will use a coordinate system where the z axis is along the beam direction, the y axis to the upward vertical direction and the x axis is given in the clockwise system. The origin of the coordinates is the target position. The elements which played an important role for the trigger will be described first, and the elements used for background rejection will be described later.

2.3.1 Trigger Hodoscopes

In order to get the fast information of the passages of two electrons, two scintillator hodoscopes were used. These hodoscopes were located in front of the lead glass calorimeter, and were composed of 1 cm thick scintillators. The upstream hodoscope, called C bank, was segmented vertically and the downstream hodoscope, called B bank, was segmented horizontally, as shown in Figure 2.5. There were 24 counters in the C bank and 30 counters in the B bank.

There were no overlaps between the counters in each bank, so that a single particle could not make two hits at each bank.

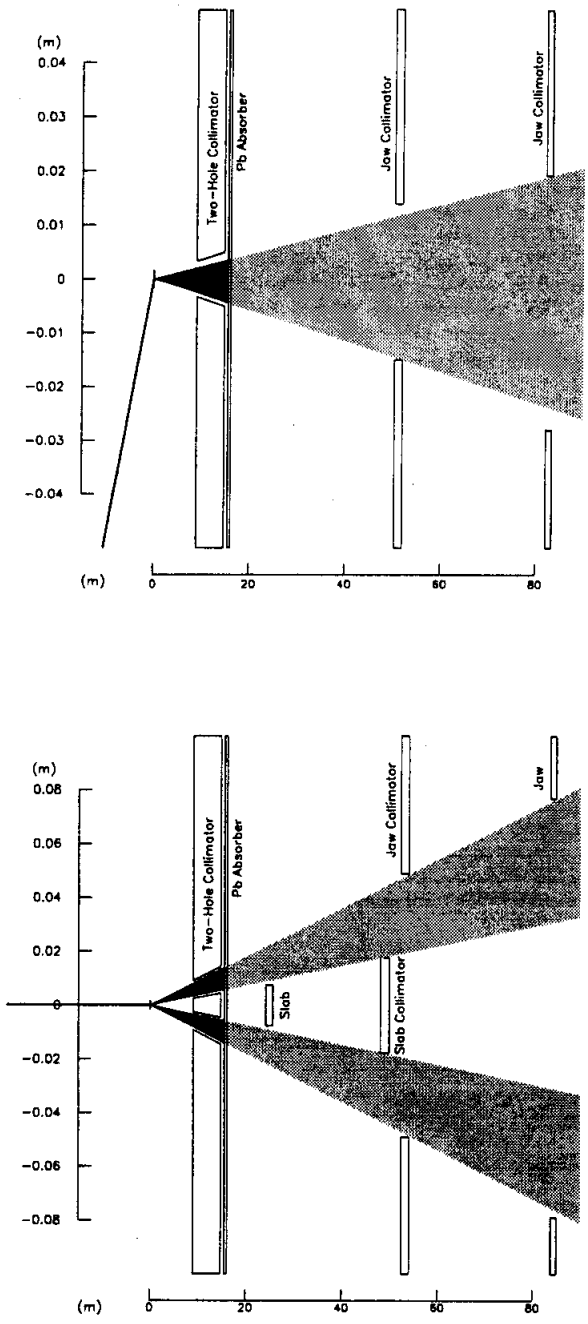

Figure 2.4: Target and collimators formed the beams in the horizontal view (up), and in the vertical view (down). Note that the horizontal and vertical scales are different.

Table 2.2: Positions and dimensions of the detector elements

Detector element	Distance from target (m)	Transverse dimensions (m)
VA -1	122.87	inner 0.0947×0.1782
		outer 0.2050×0.2863
VA 0	125.18	inner 0.0947×0.1721
		outer 0.2050×0.2889
VA 1	132.16	inner radius : 0.303
		outer radius : 0.595
VA 2	135.93	inner radius : 0.303
		outer radius : 0.595
DRA	140.94	inner 0.249×0.310
		outer radius : 0.605
VA 3	149.29	inner radius : 0.502
		outer radius : 0.885
VA 4	158.27	inner radius : 0.606
		outer radius : 0.889
Vacuum Window	158.94	radius : 0.61
Chamber 1	159.29	1.27×1.27
Chamber 2	165.86	1.42×1.57
MA	167.11	0.908×0.743
		1.057×1.067
Analyzing Magnet	168.86	$2.53 \times 1.46 \times 3.37$
Chamber 3	171.86	1.57×1.73
Chamber 4	176.20	1.78×1.78
LGA	178.71	0.908×1.403
Iron Ring	179.27	
C Bank	179.54	1.9×1.8
B Bank	179.62	2.0×2.1
Lead Glass	181.09	radius : ~ 0.91
MU1	183.97	2.0×2.2
BA	185.40	0.20×0.41
MU2	189.55	2.4×2.4
MU3	189.90	1.5×1.2

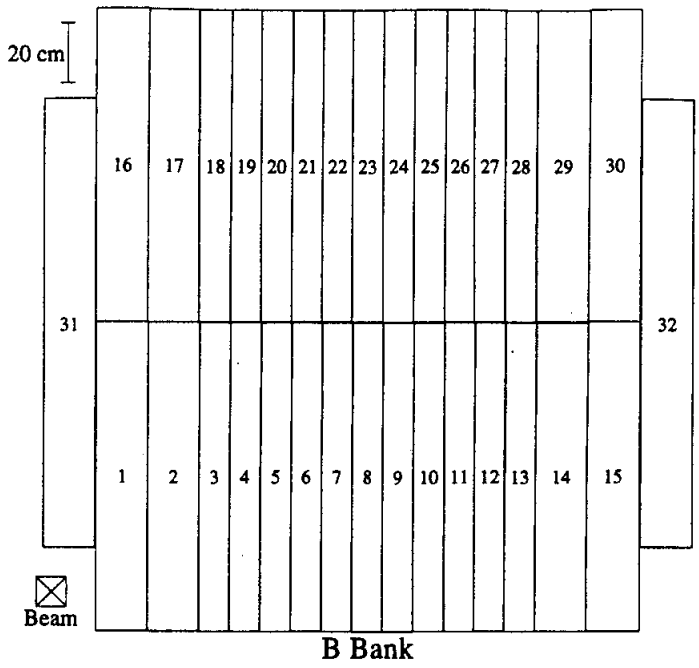

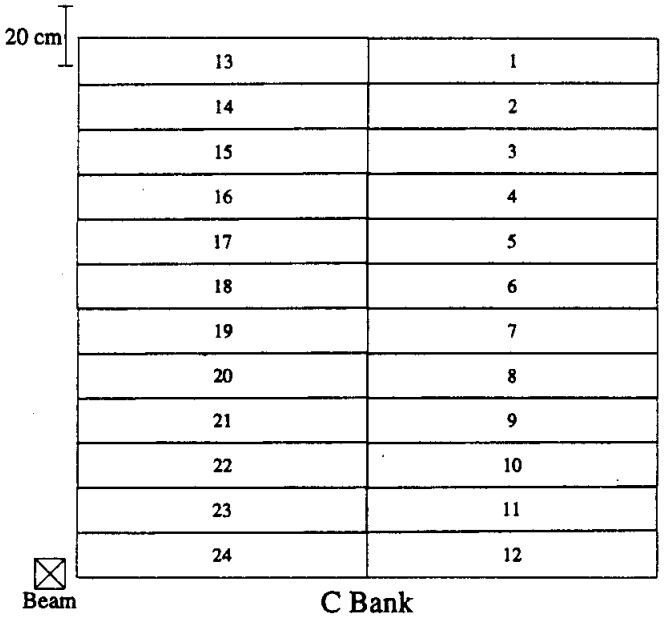

Figure 2.5: The schematic picture of the B bank and the C bank.

2.3.2 Spectrometer

Drift Chamber

The drift chambers were the main components of the spectrometer to measure the trajectories of charged particles. The principal function of the drift chambers is described in many literatures [44], and is not described here. A pair of chambers was located upstream of the magnet, and the other pair was located downstream. The size of the chambers successively increased from 1.26×1.26 m^2 (Chamber 1) to 1.77×1.77 m^2 (Chamber 4) (see Table 2.3). The drift chamber consisted of a gas filled volume, wire-supported Aclar (C_2ClF_3) windows, field-shaping wires with sense wires. Figure 2.6 shows the schematic diagram of the drift chamber components. In Figure 2.6, the field shaping wire formed a hexagon cell of the chamber, and a sense wire located at the center. The distance between adjacent sense wires was 12.7 mm, and each chamber consisted of two horizontal and two vertical sense planes. The two sense planes of the same direction had an offset by half the cell size, 6.35 mm, to solve the left-right ambiguity.

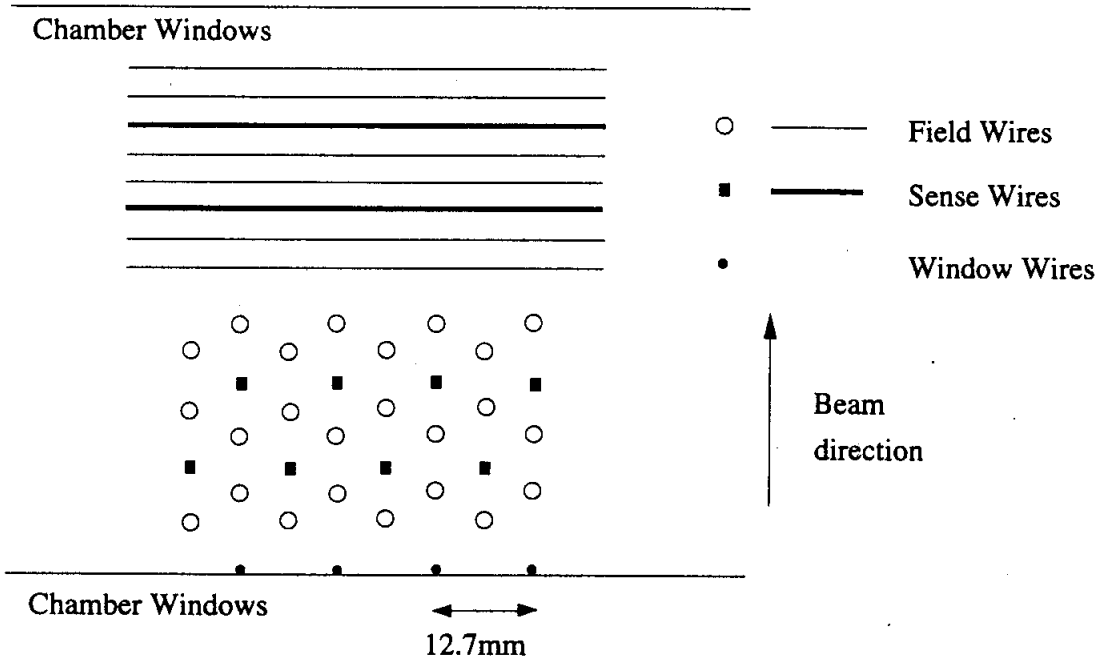

Figure 2.6: The sense and field wire geometry of the drift chamber in one view. The field shaping wire formed a hexagon cell with the sense wire located at the center.

The chamber gas consisted of 50% argon and 50% ethane by volume with 0.5% isopropyl alcohol for additional quenching. The chambers were operated with the voltage of about -2650 V, and the drift velocity was about 50 μm/ns.

The pulse from each sense wire was amplified and discriminated at the chamber. The signal was led to LeCroy 4291B time to digital converters, TDC, with a resolution of 1 ns. The same signal was led to track processor front-end boards which counted the number of hits of all chambers. The TDC's were operated in "common stop" mode where a pulse from the chambers triggered the start and the first level trigger signals stopped the operations. The time distribution of hits in a chamber plane is shown in Figure 2.7. Hits near 240 ns correspond to tracks passing near the sense wire, while those below 120 ns correspond to tracks passing farther from the wire.

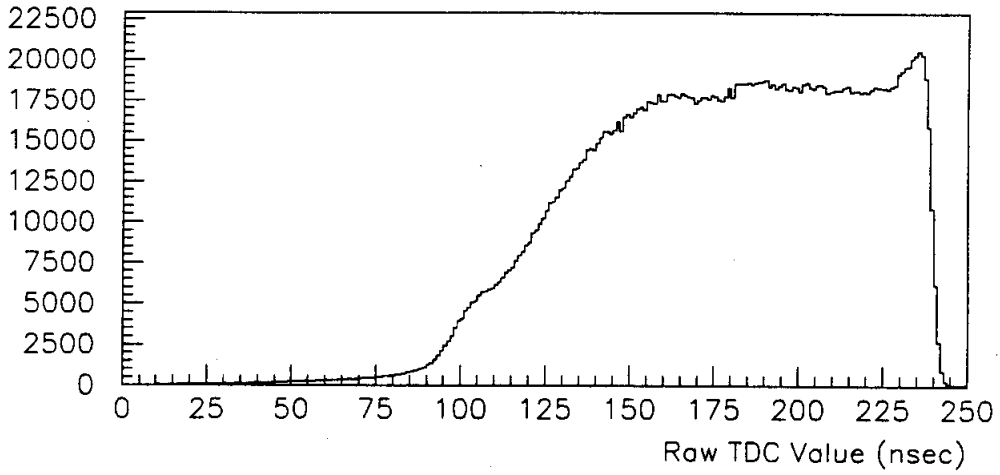

Figure 2.7: The time distribution of in-time chamber hits.

The measured time by the TDC can be translated into a distance between the sense wire and the closest point of charged trajectory with a calibration described in Reference [45]. The position resolution of each chamber can be determined from the measurement of the sum of the two drift distances in each view of a chamber. Figure 2.8 shows the schematic diagram of the drift chamber where the sum of the two drift distances should be equal to 6.35 mm which was the offset of two sense planes of the same direction. Figure 2.9 shows the distribution of the deviation from this measured sum to the offset value. There is a clear peak at 0 mm in Figure 2.9 with a width of about 150 μm. Since the width has an effect of the resolution from two planes, the resolution of each plane was approximately $150\mu m \times 1/\sqrt{2} \sim 100$ μm. The hits outside of the peak was rejected in the offline analysis. The minimum distance to resolve two tracks was about 1 cm.

Analyzing Magnet

The analyzing magnet was located between two pairs of chambers, and gave a momentum kick to passing charged particles in order to measure the momenta. The

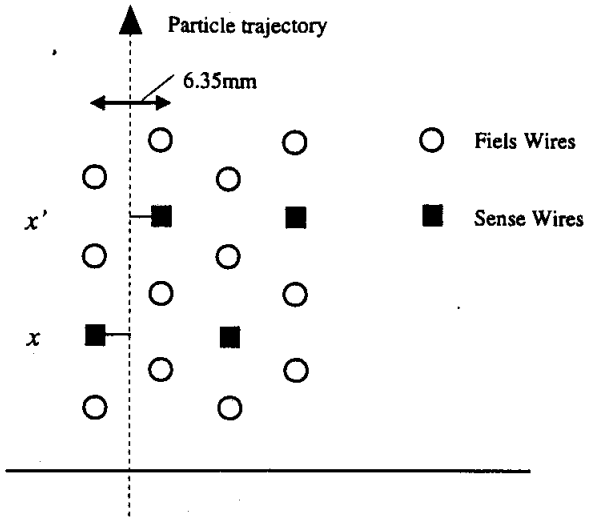

Figure 2.8: The schematic picture of the drift chamber and the passing particle.

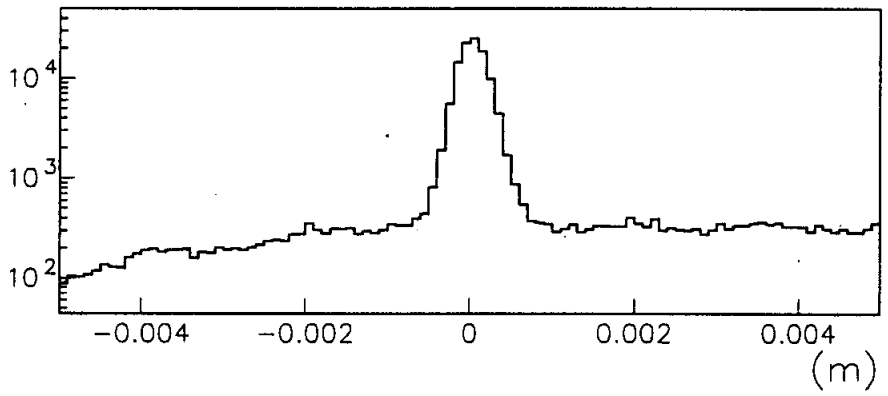

Figure 2.9: The typical deviation of sum of distances of the chamber.

Table 2.3: Material and the Radiation Length of the Spectrometer

Detector Element	Material	Thickness (cm)	Radiation Length
Vacuum Window	Kevlar-29 Fibers and Mylar	—	1.58×10^{-3}
Air Gap	Air	39.1	1.29×10^{-3}
Chamber 1	Ar, C_2H_6, Aclar, BeCu and W	—	1.48×10^{-3}
Air Gap	Air	35.6	1.17×10^{-3}
Helium Bag	He, Mylar and Polyethylene	587	1.99×10^{-3}
Air Gap	Air	26.4	0.87×10^{-3}
Chamber 2	Ar, C_2H_6, Aclar, BeCu and W	—	1.48×10^{-3}
Air Gap	Air	35.6	1.17×10^{-3}
Helium Bag	He, Polyethylene	537	1.53×10^{-3}
Air Gap	Air	30.0	0.99×10^{-3}
Chamber 3	Ar, C_2H_6, Aclar, BeCu and W	—	1.48×10^{-3}
Air Gap	Air	21.8	0.71×10^{-3}
Helium Bag	He, Polyethylene	379	1.25×10^{-3}
Air Gap	Air	25.4	0.83×10^{-3}
Chamber 4	Ar, C_2H_6, Aclar, BeCu and W	—	1.48×10^{-3}

Kevlar-29: $(C_{14}H_{10}N_2O_2)$
Mylar: $(C_{14}H_8O_4)$
Aclar: (C_2ClF_3)

size of the magnet gap was $2.53m \times 1.46m \times 3.37m$ in $x \times y \times z$ directions. This magnet provided a vertical field of approximately 4 KGauss, so that the passing charged particles were given a momentum kick of approximately 200MeV in the x direction. The horizontal magnetic field was very small, and the leakage of the magnetic field was negligible at the second and third drift chambers.

Material in the Spectrometer

In order to achieve a good momentum resolution and to suppress extra interactions like multiple scattering, bremsstrahlung and photon conversion in the detector, the amount of material in the spectrometer was minimized. The radiation length of all components of the spectrometer are listed in Table 2.3.2. The momentum resolution from the multiple scattering was calculated to be 0.5%. The resolution from the intrinsic chamber resolution was calculated to be $0.014 \times p\%$, where p is the momentum of a charged particle in GeV/c. Adding individual components in quadrature, the momentum resolution of the spectrometer was $(\sigma_p/p)^2 = ((5 \times 10^{-3})^2 + (1.4 \times 10^{-4} \times p(\mathrm{GeV/c}))^2$.

2.3.3 Electromagnetic Calorimeter

The general character of the lead glass is described in many literatures [44], and is not described here. Figure 2.10 shows blocks stacked in a roughly circular array of 0.92 m radius. In the calorimeter, electrons and photons produce electromagnetic showers. The electromagnetic shower produced the Cerenkov light, which was observed using photomultiplier tube mounted on the back of each block. Each lead glass block was wrapped in 0.0013 cm thick aluminized mylar to optically isolate a block each other and to increase the efficiency of the light collection. The phototubes were 10 stage Amperex 2202 tubes with bialkali photocathodes. They were operated at approximately $1200V$. At the above voltage the order of 1.2×10^5 gains were obtained. Optical contact between the glass and the phototube was provided by a silicon gel with an index of refraction of 1.45, which lay between that of the glass (1.6) and that of the phototube window (1.4). Additionally, there embedded a Wratten 2A filter in a gel in order to cut off the short wavelength part of the Cerenkov light, below 400 nm, which caused a significant non-linearity and degradation of energy resolution to the energy measurement. This non-linearity is caused by the following effect. The shower depth depends on the energy of the incident particle. Since the absorption of the Cerenkov light is dependent on the shower depth, the absorption caused the non-linearity of the observed light to the energy. In addition, the absorption also decreased the energy resolution because of the fluctuation of the shower depth. The light attenuation in the glass depends on the wavelength of the light, and in addition, it was strongly enhanced at the short wavelength. Therefore, the part of the short wavelength light was cut off in order to suppress the non-linearity and to achieve a good energy resolution. In spite of the 50% light loss, the resolution was improved.

The array was placed in a light-tight house to exclude the extra light from outside. The house was under temperature control within 1.5°C, so that the gain fluctuations due to temperature were effectively limited.

Next, let us discuss the signal from a lead-glass block. The analogue signal from the phototube was split into three parts. The first part had most charge and was led to a LeCroy 1885 Analog-to-Digital Converter, ADC, module through an 80 m RG-58 cable. The second part had a small portion of the signal and was used in order to sum up energy of blocks. The third part had also a small portion and was led to a hardware cluster finder (HCF), which counted the number of the energy clusters in the calorimeter.

The signal which entered the ADC was integrated over a 100 ns gate and converted to a digital number by a 12-bit ADC operated with a dual range. Though the signal from the Cerenkov light in a lead glass is very fast, the wide gate was needed because of the pulse broadening in the delay cables and also because of the scintillation light in the lead glass, which has a long term components. The dual range operation of the ADC could extend the effective dynamic range from 12 bits to 15 bits where the ratio of gains between the two ranges was 8. In the low range

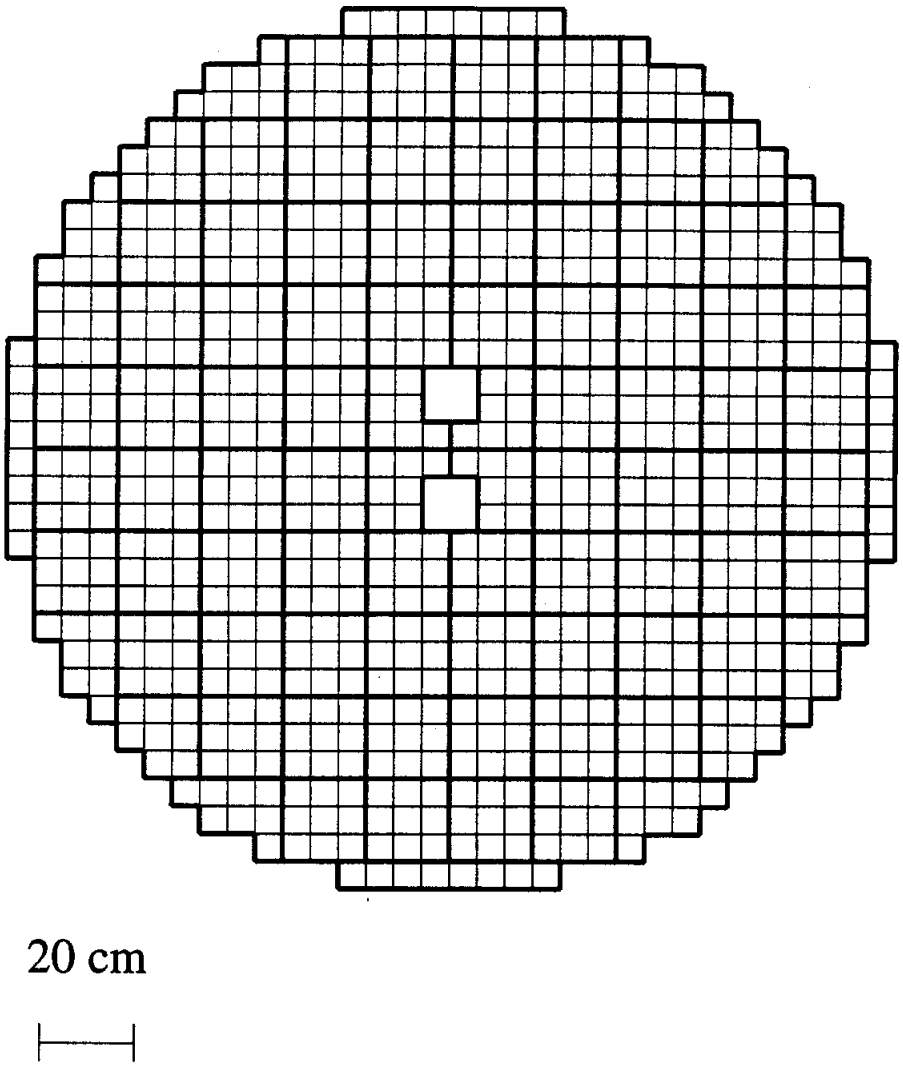

Figure 2.10: The front view of the lead glass calorimeter

the ADC gain is 20counts/pC, corresponding to about 5MeV energy/count. The high range was used when the ADC count in the low range exceeded about 3700 counts, corresponding to roughly 18GeV.

The signals for an energy sum were added in groups of approximately nine blocks each. The signal from the group was called "Adder" signal, and 92 "Adder signal"s were led to the ADC which operated with 30 ns gate. The 92 copies of the "Adder signal"s were summed up to calculate the total energy deposit in the calorimeter, called "E_t". The short gate width of the ADC for "Adder signal" allowed the identification of in-time clusters. The E_t signal was then discriminated to form a signal for the trigger. Three copies of the E_t signal were led to a same ADC as Adder signal with three different delays. Therefore, the total energy deposits at the three different time window could be measured. One time window was before the event, the other was in-time and the rest was after. These information was useful to reject the out of time accidental events.

The signals led to HCF were digitized by a 30 MHz 6 bit flash ADC. A block registered a hit if its energy was above a threshold. The threshold was set to be 2GeV and was set to be 3GeV later. The algorithm of the cluster counting are described in the reference [46, 47]. The information of the number of the clusters was used to form a signal for the trigger.

The gain of each phototubes was monitored by viewing the light from a xenon flasher. The light was distributed to each lead glass block through optical fiber which was connected to the front face of a block. The spectrum of a xenon flasher light is similar to the Cerenkov light. The amount of the light at a block corresponded to the Cerenkov light of 40GeV energy deposit by using the same gate width (100 ns). From the monitoring information, the gain of tube was corrected by changing the supplied high voltage. In addition, the phototubes viewed the DC light supplied by the light emitting diodes, LEDs, together at all time. This light suppresses the sudden gain change of a phototube at the beginning of a spill due to the sudden change of current in the phototube. This gain change is really caused by the hysteresis effect.

In the high rate environment of this experiment, the radiation damage of the lead glass was serious especially around the beam holes. The radiation damage colors the lead glass to yellow, so that the absorption length of the glass is changed from the initial value. This change decreased the light output and decreased the energy resolution. In order to cure this damage, the ultraviolet light from two 400 W mercury vapor lamps was sometimes applied to the damaged blocks.

2.3.4 Veto Counters

Photon Vetoes

Most of veto counters were built in to detect the escaping particles to the outside of the spectrometer and the lead glass acceptance. There were 6 Vacuum Anti-s (VA's), a Decay Region Anti (DRA), a Magnet Anti (MA) and a Lead Glass Anti (LGA).

The VA's were located in the evacuated volume and were built on the wall. The DRA was located just before the protrusion in the evacuated volume in which there was a magnet for a calibration run by electrons. The MA was located before an analyzing magnet in order to detect the particle which would hit the magnet. The VA's, MA and LGA consisted of a thin scintillator and two modules of 3 radiation length lead-lucite sandwiches to detect both charged particles and photons. The schematic picture is shown in Figure 2.11. The DRA consisted of two scintillation counters and a lead sheet between them, which converted a photon to be detected by the following scintillator.

In order to reject events with high-angle photons escaping through the gap between the calorimeter and the LGA, an iron ring was located just downstream of the LGA. The ring overlapped with the outer edge of the calorimeter, and was 2.9 radiation lengths thick. The schematic picture of the LGA and the iron ring is shown in Figure 2.12.

The shapes of veto counters were classified into two shapes; square and round. These shapes are shown in Figure 2.13. The VA-1, VA0, DRA, MA belonged to the square type, and the rest belonged to the round type. The dimension and the position of each veto detector is listed in Table 2.3

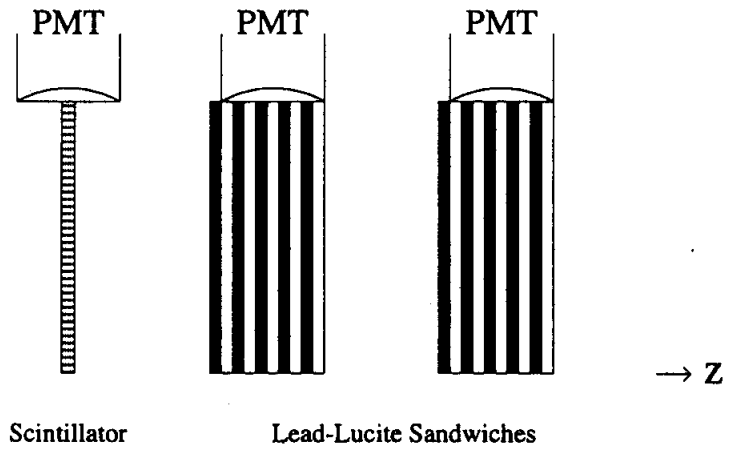

Figure 2.11: Photon veto counter

There was an another photon veto called "Back Anti (BA)" in neutral beams downstream of the calorimeter in order to reject events in which a photon missed the calorimeter through beam holes. The BA composed of 48 layers lead-lucite sandwich, and the cross section was 0.298×0.502 m^2 and the depth was 28.1 radiation length. These layers were divided into 3 parts longitudinally, so that this counter could measure the longitudinal shower development, which can distinguish between

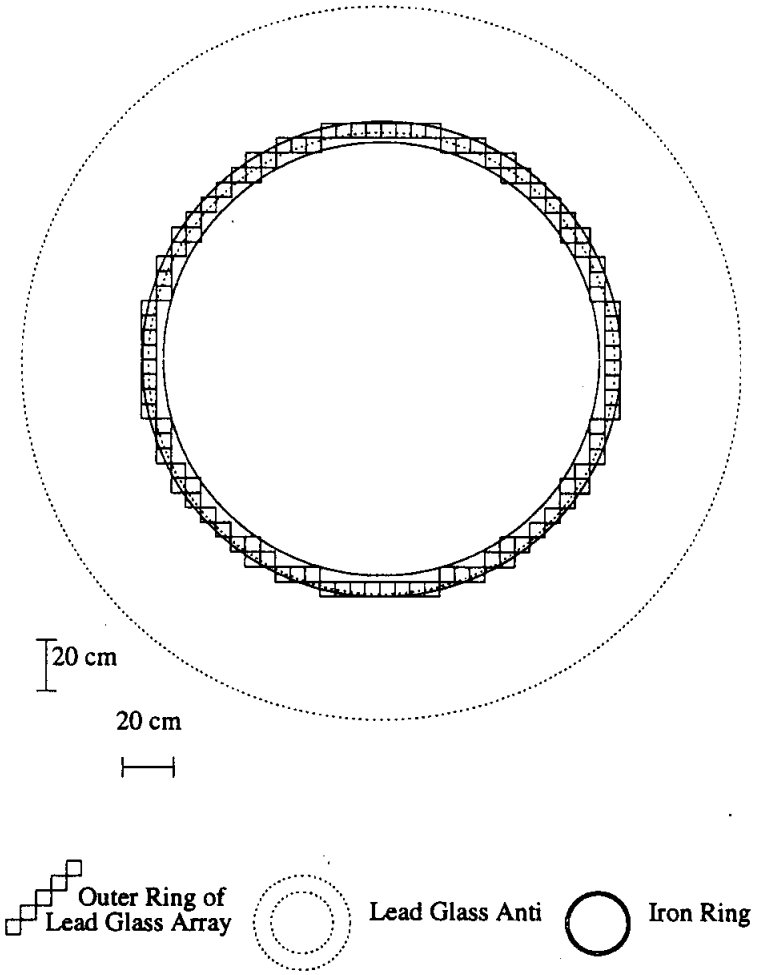

Figure 2.12: The LGA with the iron ring. The iron ring was designed to convert photons which entered the gap between the lead-glass and the LGA.

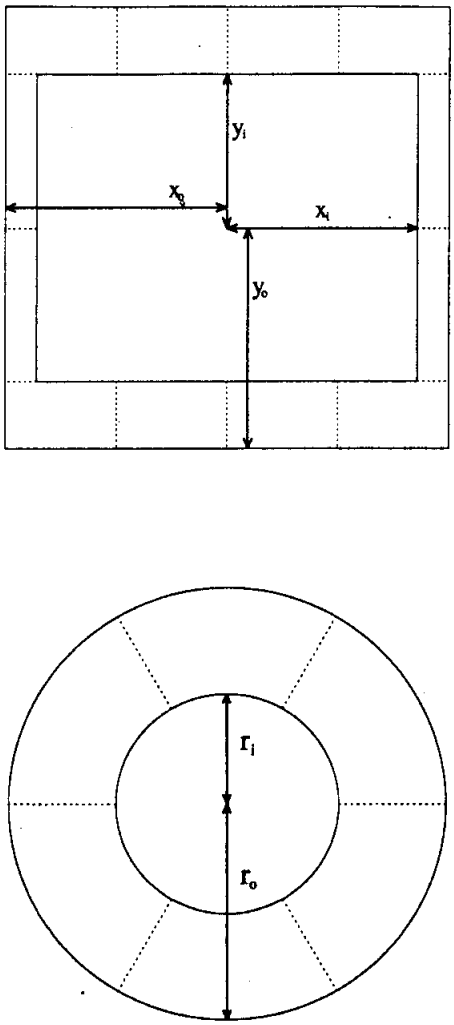

Figure 2.13: The square (up) and the round (down) photon veto counter. The MA is shown as an example of the square photon veto counter, and the VA0 is shown as an example of the round one.

electromagnetic shower and hadronic shower. The BA was used as the veto for electromagnetic shower in the $K_L \to e^+e^-\gamma\gamma$ and $K_L \to e^+e^-\gamma$ triggers.

Muon Counters

For the charged particle identification at the trigger level, there were 3 counters downstream of the calorimeter, which were referred to as MU1, MU2 and MU3.

The MU1 counter followed the lead wall of 22 radiation length behind the calorimeter, and was composed of 45 scintillators. The schematic picture of the MU1 counter is shown in Figure 2.14. The combination of the lead glass and lead wall were 42 radiation length deep, so that electromagnetic showers were absorbed in them. However the depth of the combination was 2.4 interaction length, so that hadronic showers cannot be completely absorbed and tended to deposit larger energy than the passage of the minimum ionizing particle at the MU1 counter. By setting the threshold of the analog sum from the MU1 counters to the equivalence as the passage of three minimum ionizing particle, the hadronic shower was identified at the trigger level.

The MU2 and MU3 counters followed the 3m thick steel behind of the MU1 counter. Since the 3 m steel is thick enough to absorb hadronic showers, mostly a muon hit the MU2 and MU3 counters. The MU2 was composed of 32 scintillators overlapping each other without gap. The size of composed MU2 was 2.4×2.4 m^2, large enough to reject events with a muon. The MU3 was composed of 16 non-overlapping counters, and was designed to count the number of muons at the trigger level. This counter was used to trigger events with two muons. The schematic picture of the MU2 and Mu3 counter is shown in Figure 2.15.

2.3.5 Other Detector Elements

Muon Telescope

The muon telescope was located about 30 m downstream of the target at an angle of 25 mrad isolated from all other detector elements in order to form an accidental trigger signal. The diagram is shown in Figure 2.16. The detection of a muon by this telescope was independent of the signal from other detector elements, so that the signal triggered by this telescope correctly sampled the accidental activity in other detector elements.

2.4 Trigger

In E799 experiment, the trigger was formed in two stages. The trigger at the first stage provided a decision every 19ns of the RF, by using information from fast detectors, such as the scintillation counters and lead-glass. This trigger was referred to as the Level 1 trigger. The signals from the Level 1 trigger opened the gate for

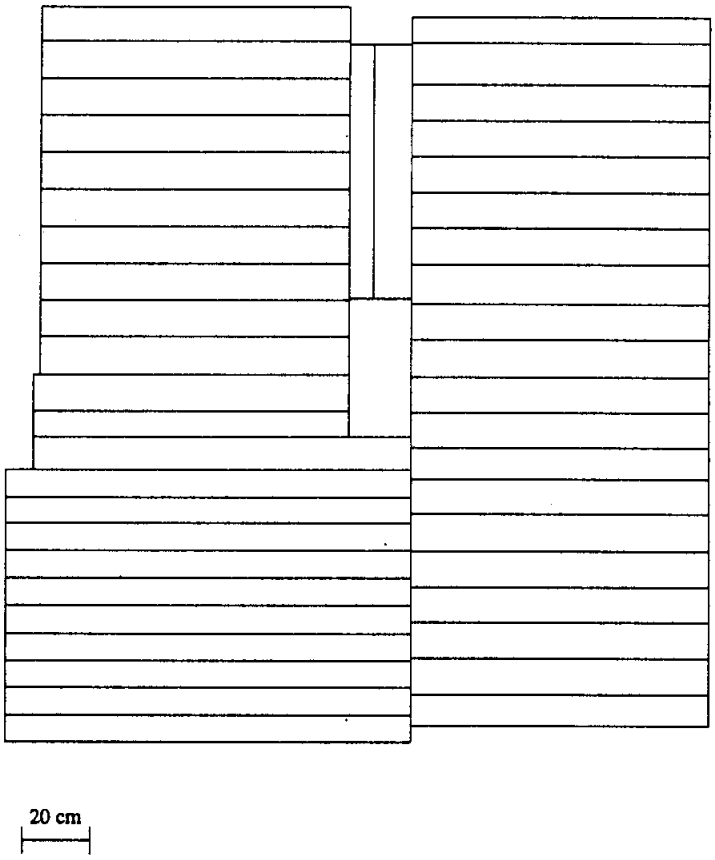

Figure 2.14: MU1 counters.

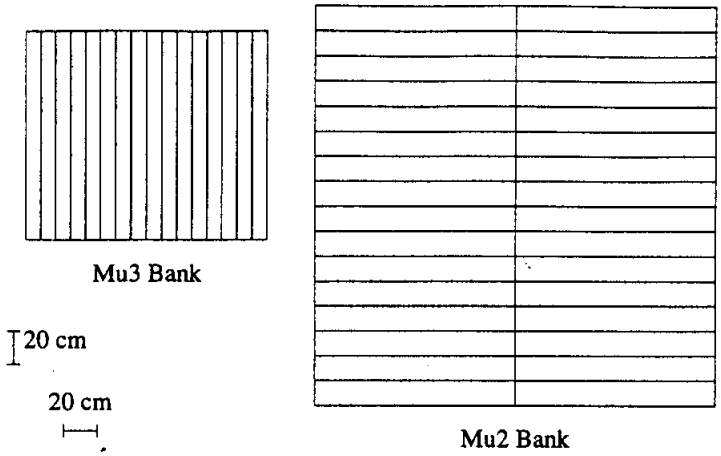

Figure 2.15: MU2 and MU3 counters.

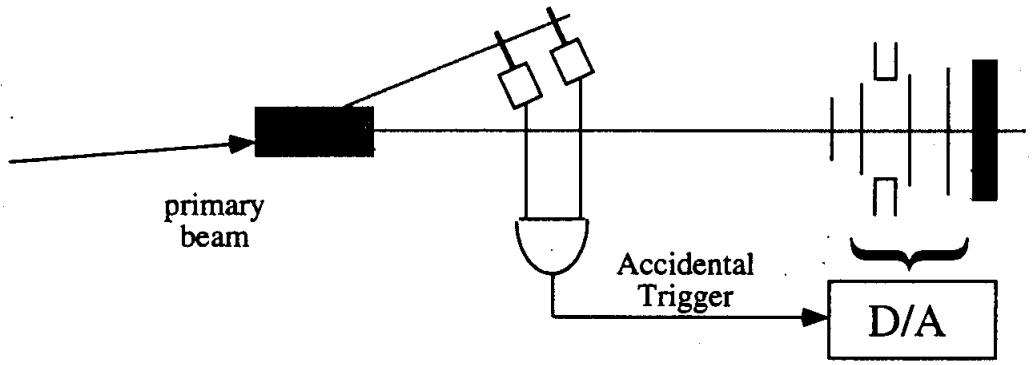

Figure 2.16: The muon counters for the accidental trigger and the diagram

Table 2.4: Sources of the Level 1 trigger

The detector	Source Name	Description
Trigger hodoscopes	2B	two or more hits at the B bank
	2C	two or more hits at the C bank
Lead-Glass	E_t Low	sum energy above the low threshold ($\approx$ 6 GeV)
	E_t High	sum energy above the high threshold ($\approx$ 50 GeV)
Photon Vetoes	VA-1 $\sim$ VA4	a hit by the charged particle at the veto counter
	DRAC, LGA	a hit by the charged particle at the veto counter
	BA12	energy above $\approx$ 2.5 GeV at the first 2/3 of BA
	BA3	energy above $\approx$ 5 GeV at the last 1/3 of BA
Muon Counters	MU1	sum energy above the threshold
	MU2	a hit in any counters
	MU3	two hits in non-adjacent counters

ADCs and gave the stop signals to TDCs. When the events passed the Level 1 trigger, the digitization of signals started. The trigger at the next stage, called the Level 2 trigger, determined whether to write events onto 8mm tapes or to abort them. The sources for the Level 2 trigger were not so fast as ones for the Level 1, but the logic of the Level 2 was more intelligent.

2.4.1 Level 1 Trigger

The trigger sources for the $K_L \to e^+e^-\gamma\gamma$ and $K_L \to e^+e^-\gamma$ Level 1 triggers are listed in Table2.4.1. The signal from each source was strobed by using Memory Lookup Unit (MLU) with the RF signal which had 53 MHz bucket structure of the beam. The pattern of the Level 1 trigger sources generated Level 1 trigger by memory lookup. The logical "OR" of these trigger bits generated the Level 1 trigger signal. The definition of the trigger at the Level 1 was programmed and changed remotely by using PDP 11 computer.

2.4.2 Level 2 Trigger

If the event passed the Level 1 trigger requirement, the digitization of the lead glass and the drift chambers information, the drift chamber hit-counting processor and the hardware cluster finder were started. If the event rate was too high after the Level 1 trigger, the type of the trigger was prescaled by an additional module with an integral prescaling factor between 2 and 16 before the Level 1 trigger. The $K_L \to e^+e^-\gamma$ trigger was typically prescaled by a factor 14.

The Level 2 trigger sources were provided by the two sets of hardware trigger devices, the track processor and the hardware cluster finder. The main function of

Table 2.5: Trigger Rate at the Level 2

Stage	Rate (Hz)
After Level 1	32,000
After Track Processor	2,300
After HCF	450

the track processor was to count the number of hits at each drift chamber, while that of the hardware cluster finder was to count the number of clusters at the calorimeter. It typically took about 20 μs to reach the final decision at the Level2. The typical trigger rate at each stage was listed in Table 2.4.2, where the proton intensity was 1.43×10^{12} protons per spill on average.

Each Level 1 trigger signal generated a $20\mu s$ dead time before the final decision by the Level2 was made. Since the trigger rate after the Level 1 was 3.2 kHz in Table 2.4.2, the dead time was $3.2(\text{kHz}) \times 20(\mu\text{s}) = 6.4\%$. After the Level 2 decision, the typical digitization time of the ADCs and the TDCs was $700 \sim 900\mu s$. The fraction of the dead time was $450(Hz) \times 900(\mu s) = 40.5\%$. The total dead time was $6.4 + 40.5 \sim 47\%$.

2.4.3 Experimental Triggers

Two Electron Trigger

The $K_L \to e^+e^-\gamma\gamma$ trigger at the Level 1 was composed of the following trigger requirement:

$2B \cdot 2C \cdot E_t\text{High} \cdot \overline{MU1} \cdot \overline{MU3} \cdot \overline{PHV} \cdot \overline{BA_\gamma}$,

where $\overline{PHV}$ was defined as $\overline{VA\ {-1}} \cdot \overline{VA\ 0} \cdot \overline{VA\ 1} \cdot \overline{VA\ 2} \cdot \overline{VA\ 3} \cdot \overline{VA\ 4} \cdot \overline{DRAC} \cdot \overline{LGA}$ and $\overline{BA_\gamma}$ was defined as $BA12 \cdot \overline{BA3}$, and all trigger sources are listed in Table 2.4.1.

At the Level 2, the number of drift chamber hits was required to be two hits per plane per view in each drift chamber, and the name of this source was defined as Hitcnt(2track). In addition, the number of the clusters on the calorimeter was required to be equal to four, six, seven or eight, and this source was defined as HCF(4,6,7,8). This trigger was designed to accept the decays $K_L \to \pi^0e^+e^-$, $K_L \to e^+e^-\gamma\gamma$, $K_L \to e^+e^-e^+e^-$, $K_L \to 3\pi^0$ with a decay $\pi^0 \to e^+e^-$ and the decay $K_L \to 3\pi^0$ with a decay $\pi^0 \to e^+e^-\gamma$. This trigger was established as "two electron trigger" as following.

$2B \cdot 2C \cdot E_t\text{High} \cdot \overline{MU1} \cdot \overline{MU3} \cdot \overline{PHV} \cdot \overline{BA_\gamma} \cdot \text{Hitcnt(2track)} \cdot \text{HCF}(4,6,7,8)$

The typical rate of the two electron trigger was 180 Hz, and the amount of the events passed the trigger corresponded to the 33% of all the accepted events.

The trigger for the decay $K_L \to e^+e^-\gamma$ was included in an another trigger called "Dalitz trigger" made for three and five cluster events.

Dalitz Trigger

The requirement of the "Dalitz trigger" was:

$2B \cdot 2C \cdot E_t Low \cdot \overline{MU1} \cdot \overline{MU3} \cdot \overline{PHV} \cdot \overline{BA_\gamma} \cdot Hitcnt(Dalitz) \cdot HCF(3,5)$,

where *Hitcnt*(Dalitz) was similar as *Hitcnt*(2track) except for the loosened requirement of only one hit in the Y-view of the chamber 1.

This trigger was optimized in order to catch the decay $K_L \to \pi^0\nu\overline{\nu}$ with $\pi^0 \to e^+e^-\gamma$ which is interesting as the probe of the direct CP violation [2]. The $K_L \to e^+e^-\gamma$ decay was also included in this trigger because the decay has same final state as the decay $K_L \to \pi^0\nu\overline{\nu}$ with $\pi^0 \to e^+e^-\gamma$. The decay $K_L \to \pi^0\nu\overline{\nu}$ has a large missing energy because of the undetected neutrinos. Therefore, the threshold of the energy sum of the calorimeter was lowered to about 6 GeV (E_t Low), in contrast to about 50 GeV (E_t High) for the two electron trigger. In addition, in order to accept two electrons of a small opening angle from the Dalitz decay efficiently, the hit counting requirements was loosened. The decay $K_L \to 2\pi^0$ with $\pi^0 \to e^+e^-\gamma$ was also acceptable in this trigger, which was used for the normalization.

Because of the lower energy threshold, the trigger rate at the Level 1 was 30 kHz due to the K_{e3} decay and the decay $K_L \to \pi^+\pi^-\pi^0$. In order to accept the events at the Level 2, the trigger was prescaled by a factor of 14 at the Level 1. The typical rate of the Dalitz trigger was 43 Hz. The amount of the events passed the trigger was 8% of all accepted events.

2.4.4 Other Triggers

There were variety of triggers in E799 corresponding to various K_L decay modes, and details of other trigger requirements are described elsewhere [48]. Besides physical motivation, some triggers were needed to understand the detector condition, basic detector response and the rejection efficiencies by each trigger requirement. These triggers were "Minimum Bias trigger", "Accidental trigger", "One-track trigger" and "Flasher trigger". In addition, the hardware ADC pedestals were recorded between spills.

The Minimum Bias trigger was defined as:

$2B \cdot 2C \cdot \overline{PHV} \cdot Hitcnt(2track)\cdot$,

which is common to all the two track triggers in order to accept the K_{e3} and $K_L \to \pi^+\pi^-\pi^0$ decays. The decay $K_L \to \pi^+\pi^-\pi^0$ was used for the normalization to other decay modes, such as $K_L \to \pi^0\mu^+\mu^-$ and $K_L \to \mu^+\mu^-\gamma$ decays. In addition, an electron in the K_{e3} decay was used for the calibration of the calorimeter. The Minimum Bias trigger rate at the Level 1 was about 1000 kHz. It was so high that this trigger was prescaled by 3600. The rate at the Level 2 was 14 Hz, and the amount of the data was 2% of all accepted data.

The Accidental trigger was formed by the signal from the muon telescope described in Section 2.3.5. This trigger was designed to collect the events uncorrelated with kaon decays but that the trigger rate was proportional to the incident proton flux at the target. This data set allowed us to study the data from all components of

the detector and to understand the accidental activity in the detector. In addition, this data was embedded in Monte Carlo events to make the event realistic with some noises and accidental activity.

The One-track trigger required at least one hit in each trigger hodoscope with MU1 in veto. Since this trigger did not use the track processor, the data by this trigger could be used to study the trigger efficiency of the track processor.

The Flasher trigger was made by the flashes of the Xenon lamp described in Section 2.3.3 to monitor the lead glass gains.

The last three trigger rates were low, and the fraction of the total data to all collected events was a few percent.

2.5 Data Acquisition

When an event passed the trigger requirements, all signals from each detector elements were digitized by the ADC's, the TDC's and the Latch modules. The ADC's were located in FASTBUS crates, and TDC's, some Latch modules and the scalers were in CAMAC crates. CAMAC is a very popular data bus in the high energy physics and has been used for many years. FASTBUS was intended to be faster than CAMAC. The data on CAMAC were shipped to the FASTBUS memory modules where the event was built by the Event Builder on the FASTBUS. Then the assembled event was shipped to VME crate where the event was buffered on the memories, and was written on the 8mm tapes. VME is very popular in general, and also faster than CAMAC. The buffering of events on memories allowed the events to be written onto tapes during the off-spill as well as during the spill. The dead time of the data acquisition was dominated by the digitization time of the ADC's, and the typical dead time was 47% (see Section 2.4.2).

2.6 Special Run

Aside from the normal physics run, some special runs were performed to monitor the detector and to calibrate the detector. These runs were the "Chamber alignment run" and the "Special electron calibration run". The Chamber alignment run and the Special electron calibration run were important to determine drift chamber positions accurately and to calibrate the lead glass, respectively.

2.6.1 Chamber Alignment Run

In order to determine the drift chamber positions accurately, straight tracks were needed. The Chamber alignment run was performed once a day with the analyzing magnet turned off to collect the straight muons tracks in the spectrometer. These data were triggered by the requirement of any hit in the B bank and of a hit in the MU2 counters. By using these muons, the chambers could be calibrated and the

position could be determined to within $2\mu m$ for the offset and within 6 μrad/m for the rotation [48].

2.6.2 Special Electron Calibration Run

In order to calibrate the lead glass calorimeter, many electron samples were needed. The electrons from K_{e3} decays were used for the calorimeter calibration at the range of high energy. In addition, the special electron calibration runs were performed six times during the experiment in order to get the lower energy electron samples. The electrons were created by photon conversion at the sheet made of 0.13 mm copper and 0.08 mm titanium located in the neutral beams. The sheet was inserted at the 77 m downstream from the target. To increase the ratio of photons to the neutral hadrons in the beams, the 7.62 cm lead and 51 cm beryllium absorber was replaced by a $119cm$ beryllium absorber. This exchange decreased the radiation length from 15 to 3.4, however the nuclear interaction length increased from 1.7 to 2.9. In addition, the proton intensity was about a factor 10 lower than that of the normal operation. Therefore, the the accidental activity on the calorimeter was lower.

The electron-positron pairs created by photon conversion tend to have the same direction of the parent photon. In order to illuminate the full surface of the calorimeter, the pair was spread by additional magnets. One magnet was located at 119 m downstream from the target, and split the pair vertically. Other magnet was located at 142 m, and split the pairs horizontally. By changing the magnet current, electrons were distributed to all surface of the calorimeter with various energies.

In order to accept the electrons, the trigger for the Special electron calibration run was typically,

$2B \cdot 2C \cdot \overline{PHV} \cdot$ Hitcnt(2track).

Chapter 3

Simulation of the Detector Acceptance

In High Energy Physics, a Monte Carlo simulation of the detector is an ordinary tool to obtain the detector response for the incoming particles. In our experiment, the Monte Carlo simulation of the detector is used to calculate the acceptance of the kaon decays. Based on the acceptance of the kaon decays, we can measure the kaon flux in the detector, we can estimate the background level in the events, and finally we can measure the branching ratio of the object. In order to measure the branching ratio, we do not have to calculate the absolute acceptance of our detector, but only calculate the relative acceptances of two similar decay modes as shown in Equation 2.1. In the ratio of the acceptances, the efficiency for the trigger and the particle identification is nearly canceled, which minimizes the systematic error due to the Monte Carlo simulation.

The E799 Monte Carlo simulation consisted of the production of the K_L beams, decays of K_L's, the tracing of the decay products, and the response of the detector. In addition, the noise of the detector and the accidental activity in the detector were embedded into the Monte Carlo events. Finally, the event from the Monte Carlo simulation was written in the same format as the real data, which made it possible to use the same analysis code between the real events and the Monte Carlo events. Along this outline, the production of K_L beams, the decays of K_L and the tracing of the decay products are described in Section 3.1, Section 3.2 and Section 3.3, respectively. In Section 3.4, the simulation of the detector response is described. Finally, in Section 3.5, the simulation of the accidental activity in the detector is described.

3.1 Production of K_L Beams

In the Monte Carlo simulation, a K_L was generated at the target ($z = 0$ m) with the energy distribution shown in Figure 2.2. The K_L with an appropriate range of the production angle and the energy was traced through the collimator described

in Section 2.2. If the K_L hits a collimator, the K_L is discarded, and the new K_L is generated from the beginning. Typically, about 15% of generated K_L's reached the detector volume without hitting the collimators.

In order to calculate the detector acceptance in the detector volume. The decay region in Monte Carlo was selected to fully cover the acceptable range for kaon decays in experiment with the smearing due to the detector resolution. The selected region was between 90 and 160 m from the target. In the same fashion, the momentum of the decayed kaon was chosen within the momentum range between 35 and 220 GeV/c. In the above ranges, the K_L decayed with the probability dependent on its lifetime and energy.

3.2 Decay of K_L's

Once the decay point and the energy of the K_L were determined, the K_L decayed to a specific mode. In our Monte carlo simulation, the K_L decayed in the center of mass frame, and then the daughter products were boosted to the lab frame with the initial K_L momentum. In this section, the models of the decays used in this analysis are discussed.

3.2.1 Radiative $K_L \to e^+e^-\gamma\gamma$ Decay and Decay $K_L \to e^+e^-\gamma$

We first describe the decay $K_L \to e^+e^-\gamma$, and then, adopt a radiative correction to the decay $K_L \to e^+e^-\gamma$, which automatically generates the decay $K_L \to e^+e^-\gamma\gamma$.

Without any radiative corrections, the differential decay spectrum of the decay $K_L \to e^+e^-\gamma$ is derived from the Feynman diagram shown in Figure 3.1 (a), which is expressed by the Kroll-Wada formula [23] as:

$$\Gamma_{\gamma\gamma}^{-1}\frac{d\Gamma}{dx} = \frac{2\alpha}{3\pi}|f(x)|^2\frac{(1-x)^3}{x}[1+\frac{2m_e^2}{xm_{K_L}^2}]\times[1-\frac{4m_e^2}{xm_{K_L}^2}]^{1/2}, \qquad (3.1)$$

where $\Gamma_{\gamma\gamma}$ is the width of the decay $K_L \to \gamma\gamma$, $f(x)$ is the form factor, and $x = m_{ee}^2/m_{K_L}^2$.

The radiative correction changes the above spectrum, which is shown in Figure 1.5. The radiative correction was composed of two parts which are shown in Figure 3.1. One part is referred to as a virtual correction which is shown in Figure 3.1 (b) and (c). This correction is caused by the virtual photon or electron loop. The other is a bremsstrahlung correction as shown in Figure 3.1 (d) and (e), where a bremsstrahlung photon is emitted. The radiative $K_L \to e^+e^-\gamma\gamma$ decay is generated by the bremsstrahlung correction. The generation of the real $K_L \to e^+e^-\gamma\gamma$ decay requires the bremsstrahlung photon energy cutoff because of the infrared divergent structure of QED. This energy cutoff divides the bremsstrahlung correction into two parts. The first part is referred to as a "hard bremsstrahlung correction", where $M_{\gamma\gamma}$ is above the cutoff. In this case, $K_L \to e^+e^-\gamma\gamma$ decay with four decay products is

(a) $K_L \to e^+e^- \gamma$

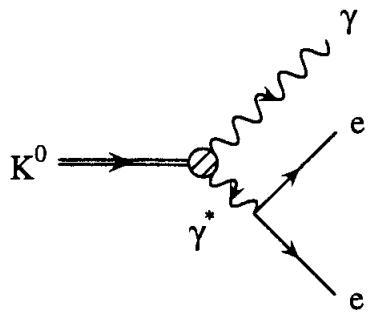

Radiative Corrections

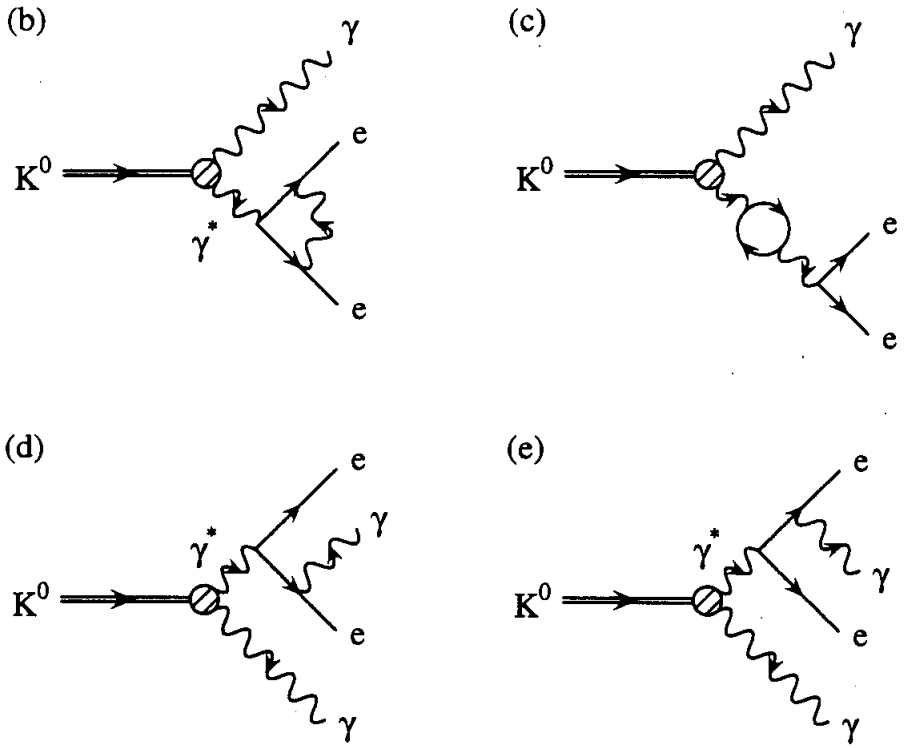

Figure 3.1: Feynman diagrams of the radiative corrections for the decay $K_L \to e^+e^-\gamma$, (a) Lowest order Feynman diagram, (b)-(c) the virtual corrections and (d)-(e) the bremsstrahlung corrections.

generated. The other part is referred to as the "soft bremsstrahlung correction", where $M_{\gamma\gamma}$ is below the cutoff. In this case, the $K_L \to e^+e^-\gamma\gamma$ decay is not generated, but M_{ee} spectrum of the decay $K_L \to e^+e^-\gamma$ is varied by this correction. We adopt the cutoff value of $x_\gamma \equiv M^2_{\gamma\gamma}/M^2_{K_L} = 20m_e^2/m^2_{K_L}$ as customarily done. This energy cutoff is far below our detector threshold, so that the dependence of the $K_L \to e^+e^-\gamma\gamma$ acceptance to the cutoff is negligible.

In order to see the characteristics of these decays, the phase space variables of the decays $K_L \to e^+e^-\gamma$ and $K_L \to e^+e^-\gamma\gamma$ were defined as follows:

$$\begin{aligned}
x &= \frac{(p_1+p_2)^2}{m^2_{K_L}} = \frac{m^2_{ee}}{m^2_{K_L}} && [\ K_L \to e^+e^-\gamma, K_L \to e^+e^-\gamma\gamma\ ], \\
y &= \frac{2P\cdot(p_1-p_2)}{m^2_{K_L}\lambda^{1/2}(1,x,x_\gamma)} && [\ K_L \to e^+e^-\gamma, K_L \to e^+e^-\gamma\gamma\ ], \\
x_\gamma &= \frac{(k_1+k_2)^2}{m^2_{K_L}} = \frac{m^2_{\gamma\gamma}}{m^2_{K_L}} && [\ K_L \to e^+e^-\gamma\gamma\ ], \\
y_\gamma &= \frac{2P\cdot(k_1-k_2)}{m^2_{K_L}\lambda^{1/2}(1,x,x_\gamma)}, && [\ K_L \to e^+e^-\gamma\gamma\ ], \\
\phi &= \text{angle between } \boldsymbol{p}_1\times\boldsymbol{p}_2 \text{ and } \boldsymbol{k}_1\times\boldsymbol{k}_2 && [\ K_L \to e^+e^-\gamma\gamma\ ], \\
&\quad \text{in the center of mass,}
\end{aligned} \tag{3.2}$$

where $\lambda(a,b,c) = a^2+b^2+c^2-2(ab+bc+ca)$, and p_1 and p_2 are the four-momenta of the electron and positron, respectively, k_1 and k_2 are the four-momenta of the two photons and P is the four momenta of the parent kaon. The x_γ is equal to 0 for the decay $K_L \to e^+e^-\gamma$. In Equation 3.2, the variables x and x_γ are related with M_{ee} and $M_{\gamma\gamma}$, respectively, and y and y_γ are related with the energy asymmetry of an electron-positron pair and two photons, respectively. The phase space distribution of these variables are shown in Figure 3.2 for the decay $K_L \to e^+e^-\gamma$ and in Figure 3.3 for the decay $K_L \to e^+e^-\gamma\gamma$. The standard Kroll-Wada formula in Equation 3.1 is also shown in the figure as a reference.

The exact formula of the decay $K_L \to e^+e^-\gamma\gamma$ is too complicated to be shown here. The formula is shown in the references [27, 28]. However the characteristics of each variable is not so difficult to be discussed here. For the decay $K_L \to e^+e^-\gamma$ and $K_L \to e^+e^-\gamma\gamma$, the x variable has a sharp peak at 0 (or x is enhanced at the low x region) because x is proportional to the mass square of the virtual photon. The x distribution of the decay $K_L \to e^+e^-\gamma$ has a sharper peak at 0 than that of the decay $K_L \to e^+e^-\gamma\gamma$ and the Kroll-Wada formula. The reason is following. The emission of the bremsstrahlung photon is suppressed at $x = 0$ because an electron-positron pair moves in the same direction, which is equivalent to 0 current. In other words, the virtual photon is close to the real photon at $x = 0$, which cannot emit a bremsstrahlung photon. The virtual correction enhances the peak for the decay $K_L \to e^+e^-\gamma$ as the counter part. The y distribution is explained by the characteristics of the internal photon conversion.

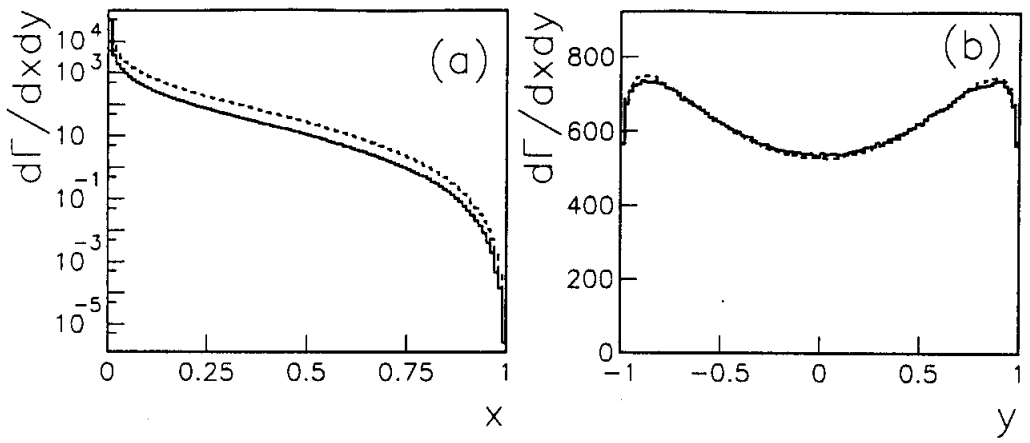

Figure 3.2: The phase space distribution of the x (a) and y (b) variables for the decay $K_L \to e^+e^-\gamma$ (solid line) with an arbitrary normalization. The x and y distributions expected from the standard Kroll-Wada formula are shown by the dashed line.

The variables x_γ, y_γ and ϕ are unique for the decay $K_L \to e^+e^-\gamma\gamma$. The x_γ distribution has a peak at 0 and is enhanced at the low x_γ region because one of two photons tends to have a very low energy because of bremsstrahlung. The same reason applies to the very asymmetric y_γ distribution. The ϕ distribution can be explained by the characteristics of bremsstrahlung. The radiative photon tends to move in the same direction as the parent electron, which is in the same plain composed by an electron-positron pair. The other photon remains in the same plane because of the momentum conservation. This is the reason why ϕ distribution has a peak at 0 or π.

Finally, both $K_L \to e^+e^-\gamma$ and $K_L \to e^+e^-\gamma\gamma$ decays were generated with the weight proportional to the matrix element with the radiative correction.

Form Factor $f(x)$

The structure of the form factor depends on the internal structure in the kaon. One of the motivations to study the decay $K_L \to e^+e^-\gamma\gamma$ is to measure the form factor. We did not adopt any special form factor, and used a constant form factor $f(x) = 1$. Therefore, the observation of any deviations between the Monte Carlo expectation and the real data is an evidence for the non-constant form factor. In addition, by fitting the deviation with Equation 1.1, we can measure the parameter α_{K^*}.

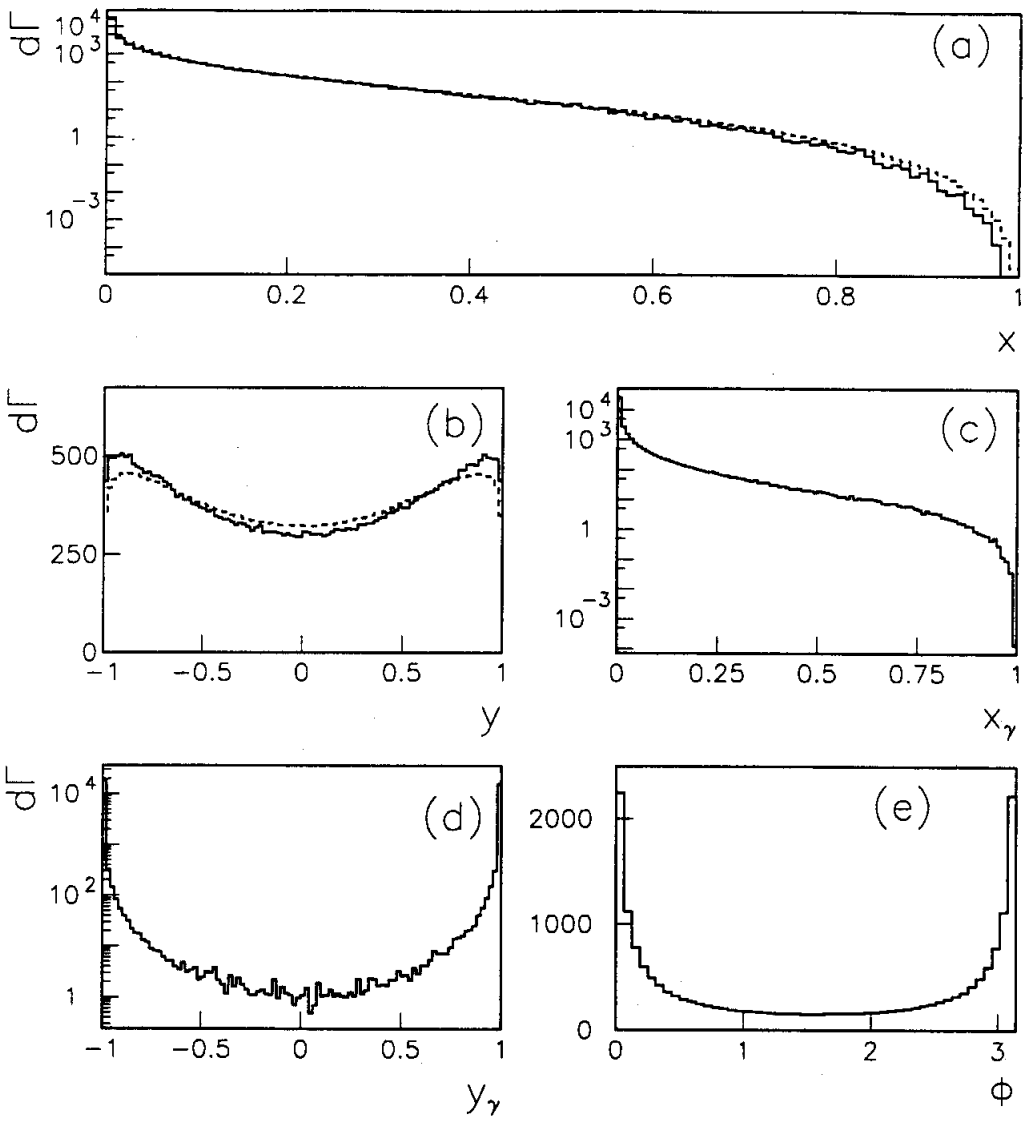

Figure 3.3: The phase space distribution of the x (a), y (b), x_γ (c), y_γ (d) and ϕ (e) variables for the decay $K_L \to e^+e^-\gamma\gamma$ (solid line) with an arbitrary normalization. The x and y distributions expected from the standard Kroll-Wada formula are shown by the dashed line.

3.2.2 Direct Emission $K_L \to e^+e^-\gamma\gamma$ Decay

In case of the direct emission $K_L \to e^+e^-\gamma\gamma$ decay, we have no exact calculations except for two general features. One feature is that the e^+e^- pair does not have a pole at $E_{\gamma^*} = 0$. The other feature is that photons are more symmetric, unlike the radiative $K_L \to e^+e^-\gamma\gamma$ decay.

Therefore, the direct emission $K_L \to e^+e^-\gamma\gamma$ decay was generated flat over the available four-body phase space.

3.2.3 $K_L \to e^+e^-H, H \to \gamma\gamma$ Decay

Similar to the direct emission $K_L \to e^+e^-\gamma\gamma$ decay, the decay $K_L \to e^+e^-H$ was generated flat over the available three-body phase space. After the decay, the Higgs-like particle, H, decayed to $\gamma\gamma$ with a finite life time.

3.2.4 Other Decays

Besides the decay $K_L \to e^+e^-\gamma$ and $K_L \to e^+e^-\gamma\gamma$, many kaon decays were generated as the backgrounds. All decays were generated with the own matrix element which are well understood currently. In these decays, a π^0 decayed into $\gamma\gamma$ or $e^+e^-\gamma$ immediately. In case of $K_L \to \pi^\pm e^\mp \nu$, the radiative correction, or the decay $K_L \to \pi^\pm e^\mp \nu(\gamma)$, was included, but the radiative correction was not included in other decays.

3.3 Tracing of Decay Products

Once the kaon decayed in the center of mass frame, the daughter products were boosted to the lab frame. These daughter particles started propagation from the kaon decay point until they went out the detector fiducial, or hit a veto counter, or reached the calorimeter. Charged pion decay, $\pi^\pm \to \mu^\pm\nu(\overline{\nu})$, was also treated correctly. The interaction at the material, the decay, or the momentum kick at the analyzing magnet changed the direction of the motion of the particles.

The charged particles were deflected by multiple scattering in the detector materials. The scattering angle distribution had the Gaussian shape and did not have tails caused by δ-rays. Monte Carlo simulation included the effect of bremsstrahlung by electrons, but not by charged pions. A bremsstrahlung photon was emitted depending on the probability based on the Bethe-Heitler cross section, and the emission angle was determined from the same formula which was represented as $d\sigma/d\theta_\gamma \sim 1/\theta_\gamma^4$ and $\overline{\theta_\gamma} = m_e/E$, where θ_γ is the angle between the electron and the photon and E is the energy of the electron. In addition, Monte Carlo simulation included the photon conversion at the material for photons with energy above 0.1 GeV. The photon conversion probability was $\frac{9}{7}e^{-(7/9)t}$ where t was the radiation length of the

material, and the energy distribution of the produced electron and positron was followed by the Coulomb-corrected Bethe-Heitler formula [50]. However, Monte Carlo simulation did not include the electro-magnetic shower simulation except for the calorimeter.

The particles generated by the above interaction propagated in the detector exactly in the same way as the daughter particles from the kaon decay. If the particles did not go out of the detector and did not hit a veto counter, the particles stopped at the calorimeter and generated a shower there.

3.4 Detector Response

In this section, we describe how active components of our detector were simulated.

3.4.1 Drift Chamber

When the charged particles crossed the drift chambers, the hit position at each plane of the chamber was smeared with the measured position resolution, and the hit was stored according to the wire efficiency. If multi hits were recorded at the same wire, only the earliest hit was kept.

The effect of δ-rays was not included in Monte Carlo simulation. The effect resulted in a tail in the chamber position measurements at approximately 0.5% level in the data. Since this effect occurred with nearly the same probability between the signal mode $K_L \to e^+e^-\gamma\gamma$ and the normalization mode $K_L \to e^+e^-\gamma$, the most parts of the effect was cancelled at the ratio of the acceptances, $A_{e^+e^-\gamma}/A_{e^+e^-\gamma\gamma}$. In addition, the tail in the position measurements was cut in the analysis.

3.4.2 Photon Veto Counters and Trigger Hodoscopes

When a charged particle hit a photon veto counter, the hit information was stored as the relevant trigger latch bit. When a photon hit a photon veto, the energy was smeared by a Gaussian whose mean and width was measured from the data. Then, the information was converted to the ADC counts.

If a charged particle went through the trigger hodoscopes, the hit was recorded according to the efficiency of the counter, and the relevant trigger latch bit was set.

3.4.3 Lead-Glass Calorimeter

The profile of the electromagnetic shower of the lead-glass by an electron was given by a shower library, a set of energy deposition pattern in 5×5 blocks, made for various hit position and energy of electron. The shower library was made from data and EGS Monte Carlo simulation. In case of photons, they were first converted to electron-positron pair at a finite depth, and the shower library was used for each of

them. The conversion depth, t, in the unit of the radiation length was determined according to the probability, $\frac{9}{7}e^{-(7/9)t}$.

The pion shower was simulated as same as that of electron.

Measured Energy

Once the energy deposition was determined, the next step was to convert the energy deposition to the collected light yield at the attached phototubes, or the measured energy. The measured energy depended on the initial energy, the light absorption coefficient of the lead-glass block and depth of the shower. The depth of the shower was constant for electrons, but varied for photons depending on the depth of the first conversion.

At first, the distribution of the measured energy should accord with a standard Gaussian whose mean and width depends on the initial energy deposit. In addition, there were two effects from the absorption coefficient of the blocks and the length of the block. The light absorption caused the light collection efficiency to be higher when the shower started closer to the phototubes. This effect resulted in the high side tail on the standard Gaussian. In contrast, if the shower was too close to the phototubes, there was a shower leakage from the back of the blocks. This effect resulted in the low side tail on the Gaussian, which was in the opposite direction to the effect of the light absorption. In order to include these effects, the measured energy distribution of electrons in K_{e3} decays or in special electron calibration run was parameterized by the following function called as "asymmetric Gaussian":

$$f(x) = \exp[-\frac{1}{2}(\frac{x - x_0}{\sigma - A(x - x_0)})^2],$$

where A represents the tail from the standard Gaussian. The positive sign of A means that the asymmetric Gaussian has a low-side tail, and the negative means that the Gaussian has a high-side tail. The function "asymmetric Gaussian" is shown in Figure 3.4. If the effect of the absorption was stronger than that of the leakage, the measured energy tends to be higher than the initial deposition, which means A is negative. In contrast, if the energy leakage was larger than the effect of the absorption, the smaller measured energy corresponds to $A > 0$. The A for each block was determined from the data.

Then, the measured energy was smeared by the photo-statistics, and was shared by 5×5 lead glass blocks. The transverse profile of the shower, or the sharing by 5×5 blocks, was determined based on a cluster library which contained many samples of real electron clusters measured in E731 experiment with EGS. Finally, these energy were translated into ADC counts.

Base on the measured energy, the total energy deposit, "E_t", and the energy deposit at "Adder" were simulated also. Furthermore, the Hardware Cluster Finder (HCF) was simulated.

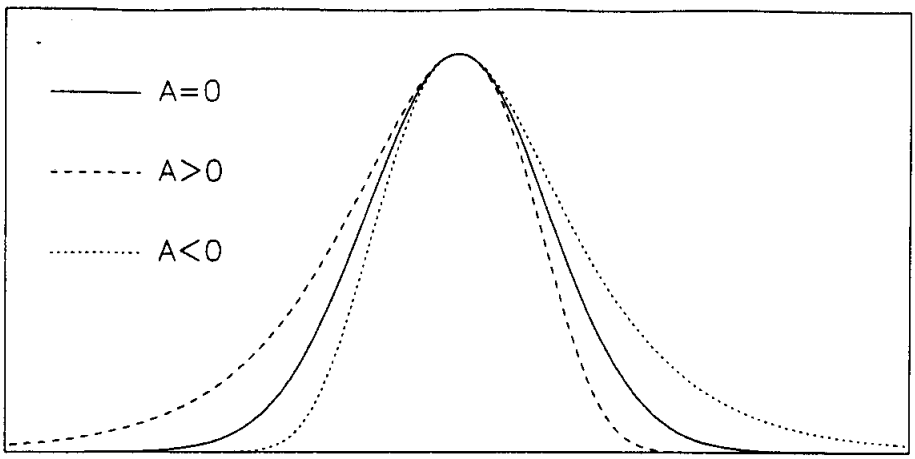

Figure 3.4: "Asymmetric Gaussian" function form

3.5 Accidental Activity

Once a Monte Carlo event was generated, the next procedure was to simulate the noise of the detector and the accidental activity from the neutral beams. The noise of the detector was independent of the beam parameters, while the accidental activity from the neutral beams depended on the beam flux. The data by accidental trigger was recorded simultaneously with the physics trigger to give a sample of both the noise and the accidental activity. The trigger rate was proportional to the incident proton flux which should be also proportional to the neutral beam flux. By embedding this data into the Monte Carlo events, the effect of the accidental activity was well simulated.

3.5.1 Accidental Overlay

Here we describe how to embed the accidental data into the Monte Carlo events. Once the kaon decay was generated in the Monte Carlo simulation, all data were in the form of the ADC counts, the TDC counts and the latch information like a real data. Then, the accidental data was read in from data tapes. The ADC values and energies from the Monte Carlo events and the accidental events were simply added together. The trigger and latch bits were "OR"ed together. As the TDC value, the earlier hit was chosen. After the overlay, the trigger requirement was checked. Once the trigger requirement was satisfied, the Monte Carlo events were recorded.

This accidental overlay was a very important process in the Monte Carlo simulation. As we saw in the accidental data, there were sometimes extra cluster or energy

on the calorimeter, extra hits on the drift chamber or extra hits on a veto counter. The real events could be disturbed by these activities and fail to satisfy the trigger requirement or analysis cuts. Also the energy resolution and the momentum resolution would be worsened. We found from MC that the accidental activity decreased the signal acceptance by about a factor 2.

In addition to the above effect, the accidental activity made new backgrounds. An example of such backgrounds was the decay $K_L \to \pi^{\pm} e^{\mp} \nu$ with two extra clusters where the pion was misidentified as an electron. This example would pass the two electron trigger requirement which required four clusters. Without the accidental activity, it was hard for the decay $K_L \to \pi^{\pm} e^{\mp} \nu$ to make a four cluster event.

All Monte Carlo events were generated with the accidental overlay.

The accidental effect was different run by run. The Monte Carlo events were generated run by run, where the kaon flux at each run was determined from the decay $K_L \to 3\pi^0$ with a $\pi^0 \to e^+e^-\gamma$, which is referred to as $K_L \to \pi^0\pi^0\pi^0_D$. At first, the events of the $K_L \to \pi^0\pi^0\pi^0_D$ were generated for every run with the same weight, and the acceptances were calculated for every run. Then the $K_L \to \pi^0\pi^0\pi^0_D$ events were observed in the real data for every run. Once the acceptance and the number of observed events were given, the kaon flux in every run was measured. The kaon flux in every run is shown in Figure 3.5 with the acceptance for every run. The number of generated Monte Carlo events in each run was proportional to the

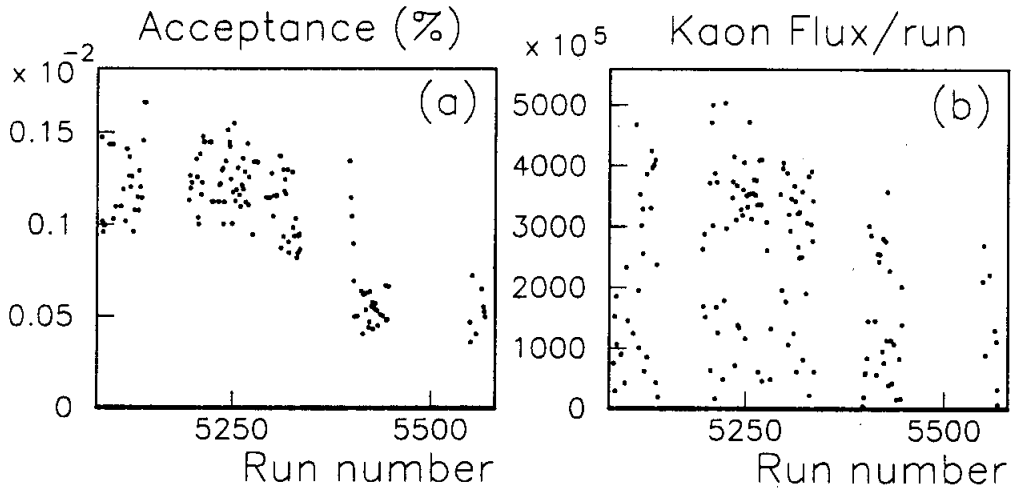

Figure 3.5: The $K_L \to \pi^0\pi^0\pi^0_D$ acceptance (a) and the measured kaon flux (b) in each run. The run number was started from 5086 and ended at 5567. The large fall of the acceptance around run = 5400 corresponds to the change of the HCF threshold. The kaon flux varies because of different lengths of runs.

measured kaon flux.

Chapter 4

Event Selection

The amount of data collected by the two electron trigger and the Dalitz trigger was over 300 Gbytes, which corresponded to about 1.8×10^8 triggers. The goal of this analysis was to extract the clean $e^+e^-\gamma\gamma$ and $e^+e^-\gamma$ samples from this huge data set in order to measure the relative branching ratio of the $K_L \to e^+e^-\gamma\gamma$ decay to that of the $K_L \to e^+e^-\gamma$ decay. In this analysis, Monte Carlo simulation was used in order to study the efficiency of the selection criteria. In Monte Carlo simulation, the model of the radiative K_L Dalitz decay was used as the $K_L \to e^+e^-\gamma\gamma$ decay which is dominated by this process. Other process in the decay $K_L \to e^+e^-\gamma\gamma$, such as direct emission contribution, should be observed as the deviation from the model of the radiative K_L Dalitz decay. In Section 4.1, the procedures of the event reconstruction are described. In Section 4.2, the events selection by using the kinematics is described in detail. In Section 4.3, we estimate the number of background events in selected signal events.

4.1 Event Reconstruction

In the analysis, the events were reconstructed in the following order.

1. The event with two good tracks were selected.
2. The event with either three or four clusters of energy on the calorimeter were selected.
3. Two tracks were matched to with the clusters.
4. Electrons were identified by requiring the track momentum (p) to match the calorimeter cluster energy to within 15% ($0.85 \leq E/p \leq 1.15$).
5. The vertex of the tracks which corresponds to the kaon decay point was required to be in the fiducial volume of the detector.

6. The trigger condition was verified. In addition, the events with an activity in the photon veto counters were rejected by applying a threshold lower than that of trigger. Finally, the trigger requirement for the decay $K_L \to e^+e^-\gamma$ was required to be exactly that same as that for the decay $K_L \to e^+e^-\gamma\gamma$ by using the software.

7. The transverse profile of each cluster was required to be consistent with that of a single electromagnetic shower. The events with a photon cluster with the energy less than 600 MeV were also rejected. In addition, the events with a cluster close to the beam holes were rejected.

In the following sub-sections, each procedure of the above event reconstruction is described in detail. The efficiency at each stage is summarized at the end of this chapter.

4.1.1 Track Finding

Track finding was carried out in $x-$view and $y-$view separately.

In the $y-$view, the hits in Chamber 1 and Chamber 4 were grouped to make segments. A track was required to have hits at the extrapolated position in Chamber 2 and Chamber 3 for each segment.

In the $x-$view, a track was bent in the analyzing magnet. Therefore, the upstream hits in Chamber 1 and Chamber 2 were grouped, and the downstream hits in Chamber 3 and Chamber 4 were grouped to make segments. The upstream segments and the downstream segments were required to match within 1 cm (10 times the resolution for a 3 GeV track) at the center of the magnet to form a track.

The number of $x-$view tracks versus the number of $y-$view tracks are shown in Figure 4.1. The events were required to have at least two tracks in both $x-$view and $y-$view. As shown in Figure 4.1, two-thirds of the events did not satisfy this requirement, and about half of the events had no tracks. The origin of the events with no track was from the interaction of the neutron in the beams with the detector material.

Next, the quality of track was checked. There would be a wrong reconstruction of track because of mis-matching at the magnet, a wrong hit caused by a $\delta-$ ray in the chambers or by an accidental activity in the chambers. In the $y-$view, because the track formed a straight line through the four chambers, the track requirement was more stringent than in $x-$view. Therefore, the cut on the track of quality was imposed in only $x-$view.

As a track quality, the distance between a straight track and hit positions obtained from drift distance, were added in quadrature at each plane in Chamber 1 and Chamber 2. This variable was referred to as the segment χ^2. The segment χ^2 was also calculated for the pair of Chamber 3 and Chamber 4. Figure 4.2 shows the distribution of the segment χ^2 for upstream tracks. The mean segment χ^2 was $\sim 2 \times 10^{-8}$ m because of the typical chamber resolution was 100 μm. The segment

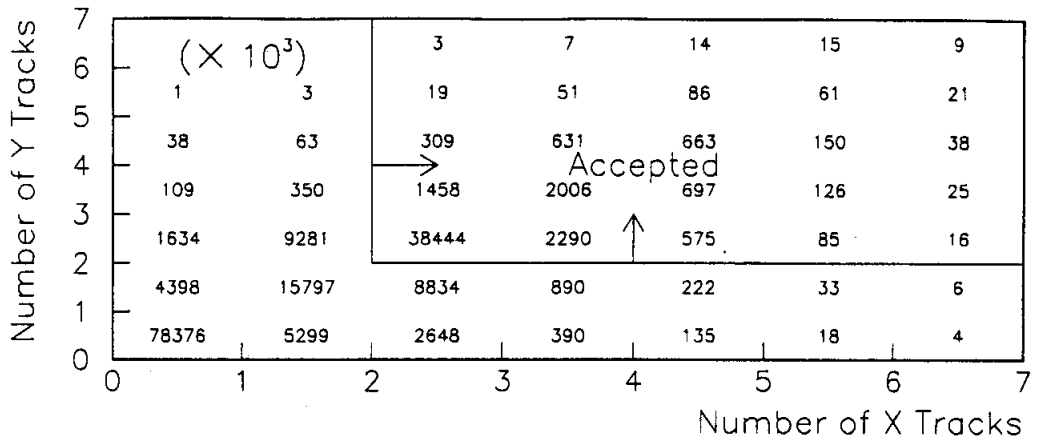

Figure 4.1: The number of $x-$view tracks versus the number of $y-$view tracks for all the events. The accepted region is shown there.

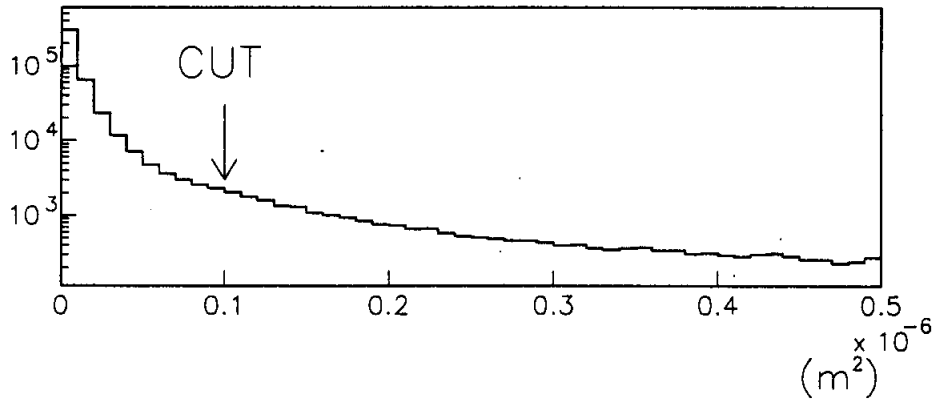

Figure 4.2: The segment χ^2 distributions for the upstream tracks. The cut was indicated there.

χ^2 for each upstream and downstream track was required to be less than 1.0×10^{-7} m.

In addition, a cut was made on the offset between upstream and downstream tracks at the center of the magnet. The resolution of the offset was formalized as:

$$\sigma_{offset} = (240 + \frac{2700}{p(GeV/c)}) \times 10^{-6}[m],$$

where the first term is from the chamber resolution and the second term is from multiple scattering and p is the momentum of the track. The offset distribution in the unit of the resolution (σ) is shown in Figure 4.3. The absolute value of the offset was required to be within 6σ for each track.

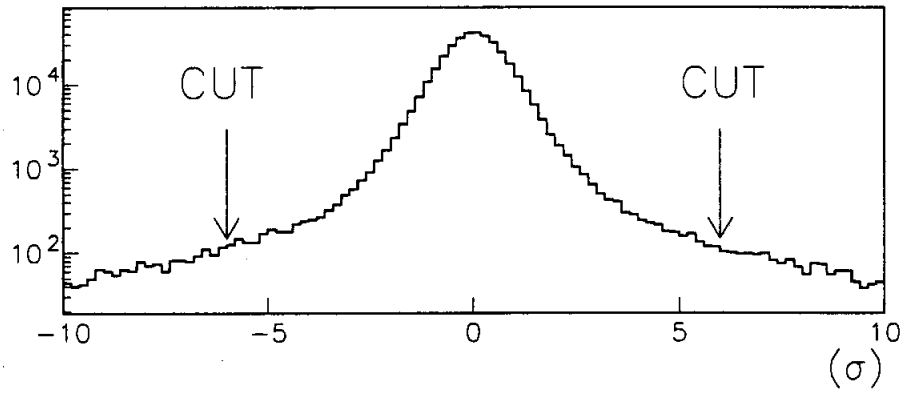

Figure 4.3: The offset between the upstream and the downstream tracks extrapolated to the plane of the analyzing magnet in the units of resolution (σ).

4.1.2 Cluster Finding

At the trigger stage, Hardware Cluster Finder (HCF) counted the number of clusters with the energy threshold of 2.5 GeV on the calorimeter, and also provided a list of the seeds of all the clusters. In analysis, for each HCF cluster, the lead-glass block with the local energy maximum was defined as the cluster center. If there were two local maxima within the single HCF cluster, it was counted as two clusters by the software (software cluster finder). The cluster was formed by 3×3 blocks around the block with the cluster center.

The energy of a cluster was measured by adding the energy in the 3×3 blocks. After track-cluster matching was done later (Section 4.1.3), a correction was applied

to the cluster energy depending on whether it was generated by an electron and a photon.

The position of the cluster was measured as followings. In the $x-$direction, the energy of the blocks in the cluster were summed in columns. The energy ratio of the center column to either side column with the larger energy determined the correct cluster position. In the $y-$view, the same procedure was carried out in rows independently. The average position resolution ($\sigma_x(y)$) in one view was approximately 3.2 mm for electrons in this data sample.

In the analysis, events were requested to have three or four clusters found both by hardware and software cluster finders. Figure 4.4 shows the distribution of the number of clusters. The events with three and five clusters were collected with the Dalitz trigger which was being prescaled by 14.

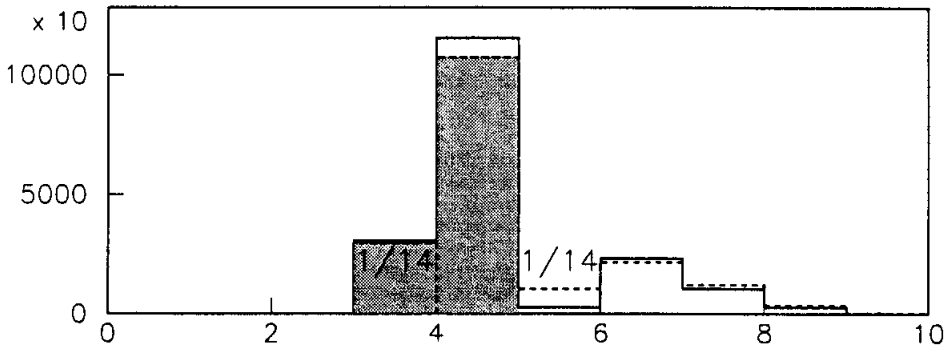

Figure 4.4: The number of clusters for the two electron and the Dalitz trigger. The number of clusters given by the HCF is shown by the solid line, and that by the software cluster finder is shown by the dashed line. The events with three or five clusters were being prescaled by 14. The selected events are shaded.

4.1.3 Track-Cluster Matching

Once the tracks and the clusters were found separately, the next step is to match the tracks to the clusters. The procedure was to consider all possible combination of two $x-$view tracks, two y-view tracks and clusters, and to find the combination with the smallest distance between tracks and clusters. As the quantity of the distance,

$$\begin{aligned} D_{(i,j=1,2)(k,l=1,\#Cluster)} &= (x_{track\ 1} - x_{cluster\ k})^2 + (x_{track\ 2} - x_{cluster\ l})^2 \\ &\quad +(y_{track\ i} - y_{cluster\ k})^2 + (y_{track\ j} - y_{cluster\ l})^2, \end{aligned}$$

was calculated for all combinations where the $x(y)_{track\ i}$ is the $x(y)-$ position on the calorimeter extrapolated from the $x(y)-$view of track i, and the $x(y)_{cluster\ k}$ is the $x(y)$ position of the cluster k on the calorimeter. The quantity $D_{(i,j)(k,l)}$ was required to be within $(7\text{cm})^2$ (the position resolution of the calorimeter is less than $6mm$ in the worst case), and the combination with the minimum $D_{(i,j)(k,l)}$ was selected. If no successful match of two tracks to two distinct clusters was found, the event was discarded. The clusters associated with the tracks were considered as electron candidates, and other clusters were considered as photon candidates. The events with two electron clusters were selected.

Once the track-cluster matching was done, the x-view tracks were also matched to the $y-$view tracks.

4.1.4 Electron Identification

Electrons deposit most of their energy in the calorimeter, while pions generally deposit only a small fraction of their energy there because of leakage from the back. Therefore, electrons were identified by requiring the track momentum (p) to match the calorimeter cluster energy to within 15% ($0.85 \leq E/p \leq 1.15$). Figure 4.5 shows the E/p distribution for each track. In Figure 4.5, the events outside of the peak

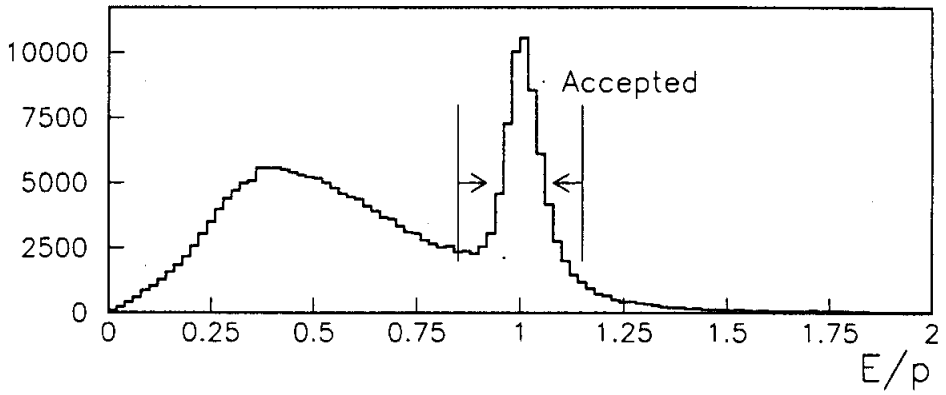

Figure 4.5: The E/p distribution for each track. The peak at 1 is from electrons, and the events outside of the peak is from charged pions or due to overlapped clusters on the calorimeter.

at 1 is from charged pions or overlapping clusters. The origin of the rejected events with pions were the decay $K_L \to \pi^+\pi^-\pi^0$ and the decay $K_L \to \pi^\pm e^\mp \nu$.

4.1.5 Fiducial Volume Requirement

Once the events with two electron tracks were selected, the next step was to calculate the vertex from two tracks. The tracks with the same sign charge were rejected before this calculation.

At first, the z location which gives the minimum distance between the two tracks was calculated. The minimum distance is shown in Figure 4.6, and was required to be less than 6σ of the resolution. The resolution was $\sigma = 0.245 \times 10^{-4} + 0.0085[(1/p_1)^2 + (1/p_2)^2]$ m where each track momentum was in the units of GeV/c.

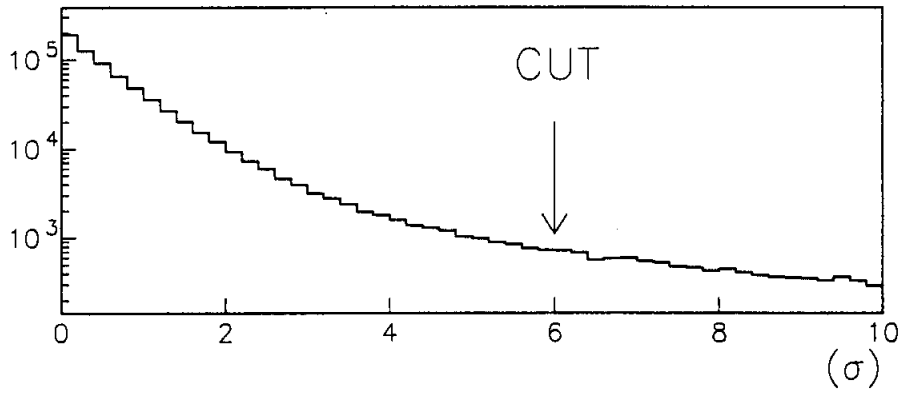

Figure 4.6: The minimum distance between the two tracks in the units of the resolution (σ).

At second, the average x and y locations of two tracks at the above z position were calculated. By using the location as a starting point, the two upstream tracks were re-fitted assuming that the two tracks originated at the common vertex. This fit took the eight measured position of the two tracks in the upstream chambers, and it returned the best fit vertex point, along with the new x and y slopes of the two tracks. The fit also returned a χ^2, which was referred to as the vertex χ^2. The vertex χ^2 is shown in Figure 4.7, and it was required to be less than 15.

The vertex was required to originate in the kaon beams and in the fiducial volume of the detector. Figure 4.8 shows the x, y and z vertex distributions for the data and the $K_L \to e^+e^-\gamma\gamma$ Monte Carlo events. The x vertex was required to be between -0.05 and 0.05 m, the y vertex was required to be between -0.16 and -0.03 m or between 0.03 and 0.16 m, and the z vertex was required to be between 100 and 160 m. The rejected bump in the data at $x = -0.08$ m and $z = 125$ m is due to the electron-positron pair created by the photon conversion at the edge of $VA0$ counter. In addition, the sharp peak at $z = 160$ m in the data is also rejected, which was

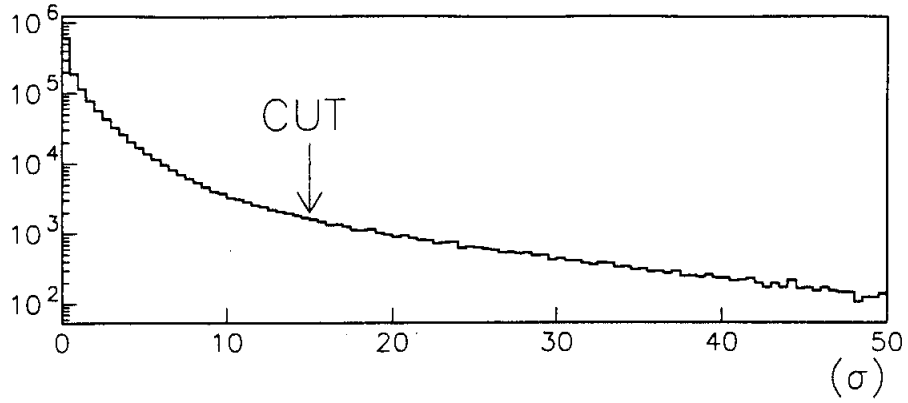

Figure 4.7: The vertex χ^2 distribution

caused by interactions of photons in the vacuum window material.

4.1.6 Trigger Verification

Trigger Counter

In order to reduce the trigger events caused by the accidental, the hodoscope counters crossed by the tracks were required to have hits. In addition, the number of hits generated by the tracks at each hodoscopes was required to be two. The events with the tracks which crossed some inefficient counters on hodoscopes or drift chamber cell were removed.

Photon Veto

In order to remove the events in which a photon missed the calorimeter, the cut on the photon veto counters was applied. Although the photon veto counters were used as the trigger source, a lower threshold was applied in the software. The threshold for each veto counters was determined from the the fully reconstructed $K_L \to 3\pi^0$ decay samples where one π^0 decays to $e^+e^-\gamma$ ($K_L \to \pi^0\pi^0\pi^0_D$). The threshold was chosen such that the loss of acceptance was less than 5% by the accidental activity. The response of each photon veto counter for the decay $K_L \to \pi^0\pi^0\pi^0_D$ is shown in Figure 4.9 with the applied threshold. The threshold on each photon veto was between 0.8 and 1.8 minimum ionizing particle equivalence, which corresponds to the energy between 0.11 and 0.25 GeV for photons.

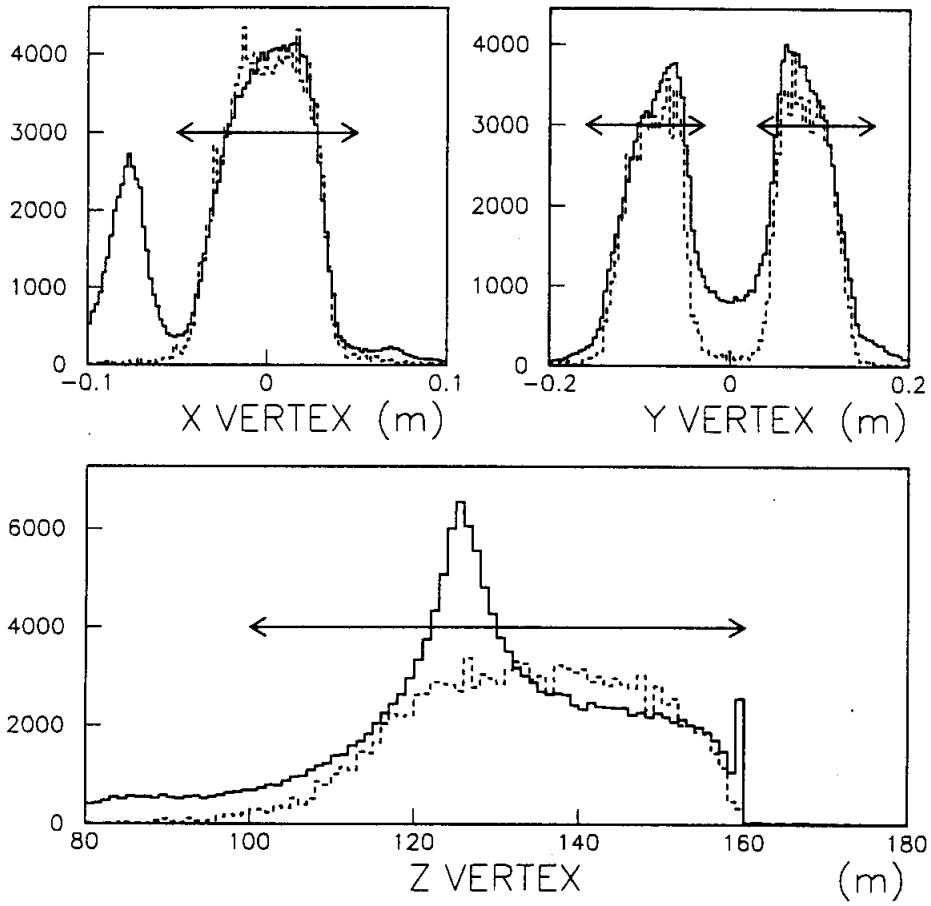

Figure 4.8: The x, y and z vertexes distributions for the data (solid line) and the $K_L \to e^+e^-\gamma\gamma$ Monte Carlo (dashed line). The accepted regions are shown by the arrows. The x axis is horizontal, the y axis is vertical, and the z axis is along the beam direction where the origin of the coordinates is the target position.

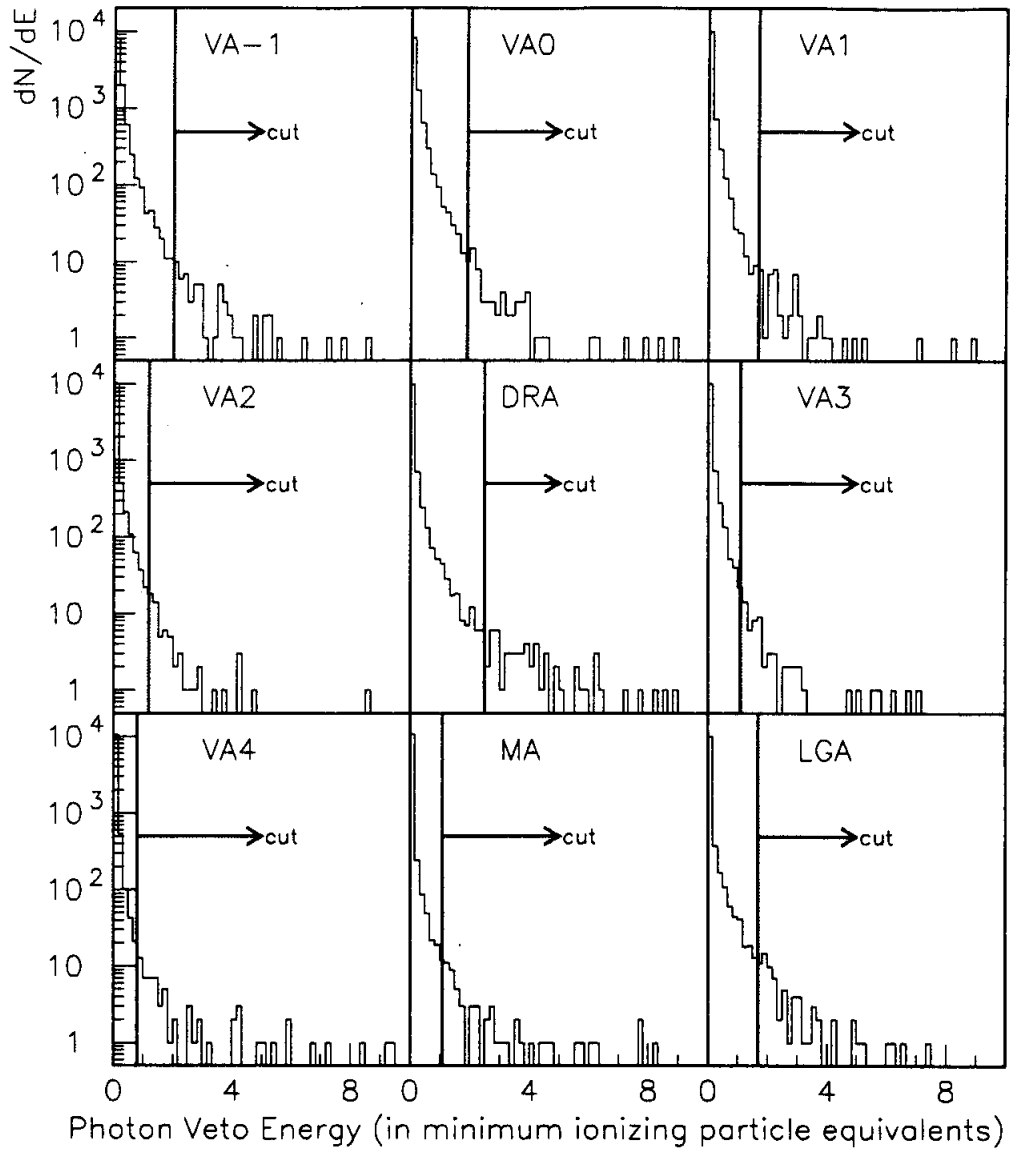

Figure 4.9: The Photon Veto Energy for the decay $K_L \to \pi^0\pi^0\pi^0_D$, and the analysis cuts are shown there.

Dalitz Trigger

In order to minimize the systematic uncertainty in the trigger efficiency between the signal events and the normalization events, the events collected by the Dalitz trigger were required to satisfy the two electron trigger except for the number of the clusters. Actually, the events collected by both two electron and Dalitz triggers were required to satisfy the triggers of "E_tHigh" and "*Hitcnt*(2track)" by checking the trigger latch. These triggers are described in Section 2.4.3.

Figure 4.10 shows the total energy distributions for the data and $K_L \to e^+e^-\gamma$ Monte Carlo events corrected by the Dalitz trigger. The higher E_t threshold sup-

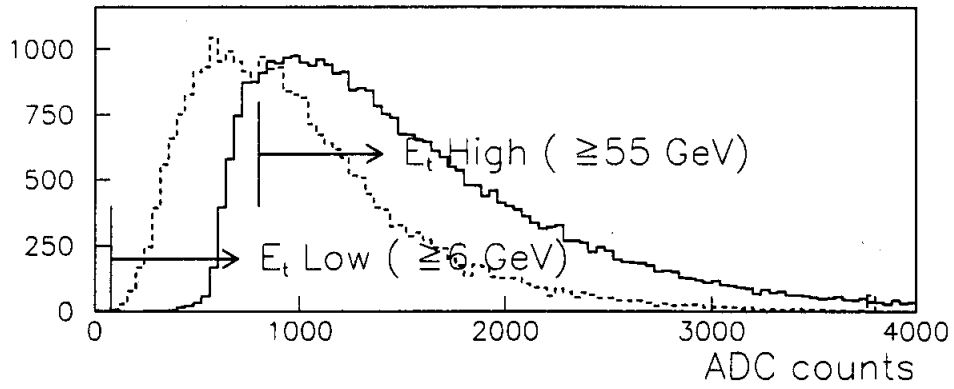

Figure 4.10: The energy deposit by the decay $K_L \to e^+e^-\gamma$ Monte Carlo events is shown (solid line) with the E_t High (> 55GeV) and the E_t Low (> 6GeV) thresholds. The events collected by the Dalitz trigger are shown by the dashed line. The normalization for the Monte Carlo is arbitrary.

pressed the low energy backgrounds which mainly came from the K_{e3} decay, while the *Hitcnt*(2track) did not affect both events.

4.1.7 Fusion Cut

Fusion Cut

Because of the discrete transverse segments of the calorimeter, two or more particles close to each other formed a single cluster in the calorimeter. This effect was referred to as the "fusion" of clusters.

If a cluster was associated with a track, the fusion was found easily by the mismatch between track and cluster positions, and by a large E/p. For clusters not

associated with tracks, the transverse profile of the cluster was useful to find the "fusion". There were three algorithms to find the fusion.

In the first algorithm, we used the 5×5 leadglass blocks with the maximum energy deposit in the center block. In the outer edge blocks (5×5 ring blocks), each energy sum of all adjacent pair blocks was measured. If the energy sum of one of the pairs exceeded 0.8 GeV, the event was discarded. The example of this fusion is shown in Figure 4.11 (a).

In the second algorithm, the energy of the 3×3 blocks in the cluster were summed in columns, and the ratio among the energy sums was calculated. The event which did not satisfy the following relations were discarded:

$$\begin{aligned} R_{max}(R_{min} - 0.02) &< 0.025(\text{if } E_{cluster} > 20\text{GeV}) \\ &< 0.015(\text{if } 20\text{GeV} > \text{E}_{\text{cluster}} > 4\text{GeV}), \end{aligned}$$

where the R_{max} is the larger ratio and the R_{min} is the smaller ratio of the two. In addition, the same algorithm was applied to the rows. This example is shown in Figure 4.11 (b).

In the last algorithm, the energy of each corner blocks was measured and compared with the adjacent edge blocks in the 3×3 cluster blocks. If the corner block had more than twice the energy of the adjacent edge blocks, the event was discarded. This example is shown in Figure 4.11 (c).

These fusion cuts were applied for every cluster including the clusters associated with the tracks. Since the fusion cuts were tuned for single electromagnetic shower, these were also effective to reject the events with hadron shower, such as the neutron interaction in the calorimeter or charged pion shower from the K_{e3} and $K_L \rightarrow \pi^+\pi^-\pi^0$ decays.

Low Energy Photon Cut

Low energy photons below the HCF threshold (2.5 GeV) were sometimes not detected as clusters in the calorimeter. These events were rejected as followings.

Among the blocks which did not fire HCF, the block with the maximum energy was searched for. The energy of adder which included the above block was required to match the sum of energy of all blocks in the adder within 40%. This requirement selected the in-time photon hit since the energy of adder was integrated with the shorter gate than for the energy of blocks. The event was rejected if the maximum energy block had energy larger than 600 MeV.

Events around Beam Holes

Since clusters at the blocks around beam holes might have energy leakage to the beam hole, the energy and the position of the clusters were not measured correctly. The event whose clusters were located within 5.8 mm (1/10 block size) from the beam holes were rejected.

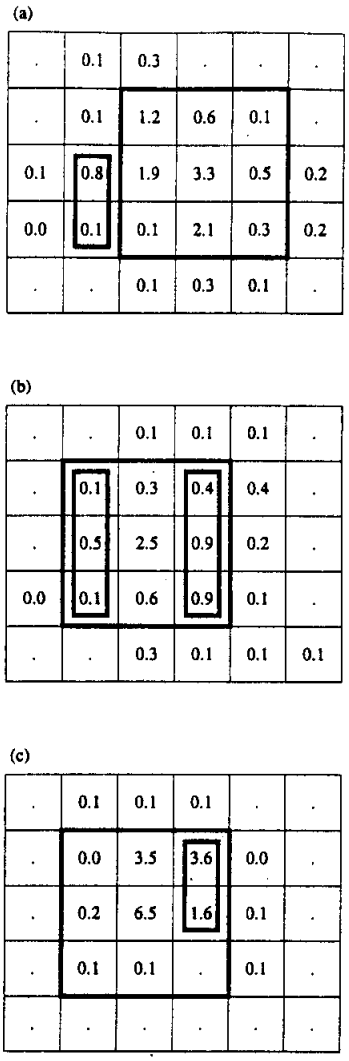

Figure 4.11: Examples of fusion events. The energy deposits in GeV are shown for the subsets of the lead-glass array. The 3×3 blocks of the cluster and the blocks whose energy deposits were caused by the fusion are outlined. (a) This event was classified as the first kind of the fusion in the text. Since the maximum energy deposit of the pair blocks in the 5×5 ring blocks is greater than 0.8 GeV, this event was rejected as a fusion. (b) This was classified as the second kind of fusion. The ratio of the energy sum of the column lines , which are outlined in the figure, satisfied the second definition of fusion. (c) This was the third kind of fusion. There is the excessive energy deposit in the corner block.

4.1.8 Summary

Finally, 151,700 $e^+e^-\gamma\gamma$ events and 56,965 $e^+e^-\gamma$ events passed all above cuts.

4.2 Event Selection

In this section, the decays $K_L \to e^+e^-\gamma\gamma$ and $K_L \to e^+e^-\gamma$ are selected by using the kinematics of these decays. In Section 4.2.1 and Section 4.2.2, the $K_L \to e^+e^-\gamma\gamma$ and $K_L \to e^+e^-\gamma$ events were selected without assuming decay models; the radiative $K_L \to e^+e^-\gamma\gamma$ decay, the direct emission $K_L \to e^+e^-\gamma\gamma$ decay, or the $K_L \to e^+e^-\gamma\gamma$ decay through unknown process. In Section 4.2.3, these events were further selected by using the models of $K_L \to e^+e^-\gamma$ and the radiative $K_L \to e^+e^-\gamma\gamma$ decays.

The summary of the event selection is described at first in order to define the outline of this analysis.

1. The square of the transverse momentum sum respect to the K_L direction was required to be less than 1000(MeV/c)^2.

2. The invariant mass cut was performed. For the $e^+e^-\gamma\gamma$ events, the $\pi^+\pi^-\gamma\gamma$ invariant mass was calculated to reomve $K_L \to \pi^+\pi^-\pi^0$ events. Then, the kaon mass window was set to be between 466 and 530 MeV/c^2 for both $e^+e^-\gamma\gamma$ and $e^+e^-\gamma$ events.

3. The following cuts were applied on the phase space distribution of the $K_L \to e^+e^-\gamma$ and $K_L \to e^+e^-\gamma\gamma$ decays to select a clean sample of $K_L \to e^+e^-\gamma\gamma$ and $K_L \to e^+e^-\gamma$ events. One cut used the relation among the angles between a electron and a photon, which removed the background events from K_{e3}. The other cut used the minimum angle between electrons and photons in the center of mass frame of the kaon. The minimum angle was required to be less than 0.5 radian in order to suppress the background from $K_L \to 2\pi^0$. In addition, the minimum angle was also required to be greater than 0.06 radian to suppress the background from $K_L \to e^+e^-\gamma$ with external bremsstrahlung.

The details are described in the following sub-sections. The efficiency at each stage is summarized at the end of this chapter.

4.2.1 Square of Transverse Momentum Sum (p_t^2)

By requiring a momentum conservation in the plane transverse to the K_L direction, we can reject background events which have a missing particle or an accidental activity. The transverse momentum (p_t) was defined as the sum of transverse momentum to the initial K_L direction of all observed particles. The K_L direction was measured as the vector from the target to the decay vertex. The momenta of photons were calculated by using the energy and the direction from the K_L decay vertex to the cluster position in the calorimeter.

Figure 4.12 shows the p_t^2 distributions for the data and Monte Carlo events. The sharp peak in the $e^+e^-\gamma\gamma$ events was due to the $K_L \to \pi^+\pi^-\pi^0$ decays where two pions were misidentified as electrons. In Monte Carlo simulation, the peak was well reproduced by the $K_L \to \pi^+\pi^-\pi^0$ MC events. The $K_L \to e^+e^-\gamma\gamma$ Monte Carlo events also have a peak at 0. Events were required to have p_t^2 of less than 1000(MeV/c)^2, which keeps 80% of $K_L \to e^+e^-\gamma\gamma$ Monte Carlo events.

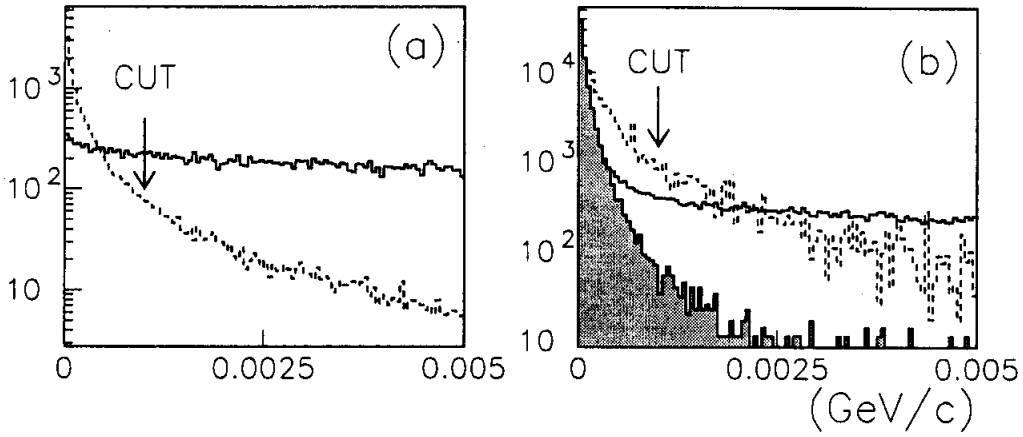

Figure 4.12: p_t^2 distributions for $e^+e^-\gamma$ events (a) and $e^+e^-\gamma\gamma$ events (b). The solid line is data, and the dashed lines are the expectations from the $K_L \to e^+e^-\gamma$ and $K_L \to e^+e^-\gamma\gamma$ Monte Carlo events, respectively, with an arbitrary normalization. The shaded region shows $K_L \to \pi^+\pi^-\pi^0$ Monte Carlo events.

In the $e^+e^-\gamma$ events, the rejected events were mainly K_{e3} background events ($K_L \to \pi^\pm e^\mp \nu(\gamma)$ background) where a pion was misidentified as an electron, and an extra photon came from bremsstrahlung or accidental activity. These background events have a flat p_t^2 distribution. In the $e^+e^-\gamma\gamma$ events, the events rejected by this cut were mainly the following backgrounds. One background came from the K_{e3} decay, referred to as $K_L \to \pi^\pm e^\mp \nu(2\gamma)$ background, where a pion was misidentified as an electron, and two extra photons came from bremsstrahlung or accidental activity. Other background came from the decays $K_L \to 2\pi^0$ or $K_L \to 3\pi^0$ where one π^0 decayed to $e^+e^-\gamma$, and photons were missed or overlapped with other photons. These $K_L \to 2\pi^0$ and $K_L \to 3\pi^0$ backgrounds were referred to as $K_L \to \pi^0\pi^0_D$ and $K_L \to \pi^0\pi^0\pi^0_D$ backgrounds, respectively.

4.2.2 Invariant Mass Cut

$K_L \to \pi^+\pi^-\pi^0$ Cut

A large amount of $K_L \to \pi^+\pi^-\pi^0$ background events were contained in the $e^+e^-\gamma\gamma$ events. Figure 4.13 shows the $\pi^+\pi^-\gamma\gamma$ invariant mass, $M_{\pi\pi\gamma\gamma}$, distribution for the $e^+e^-\gamma\gamma$ events. The events with the $M_{\pi\pi\gamma\gamma}$ between 450MeV/c^2 and 550MeV/c^2 were rejected in the $e^+e^-\gamma\gamma$ events. The loss of the $K_L \to e^+e^-\gamma\gamma$ signal was negligible.

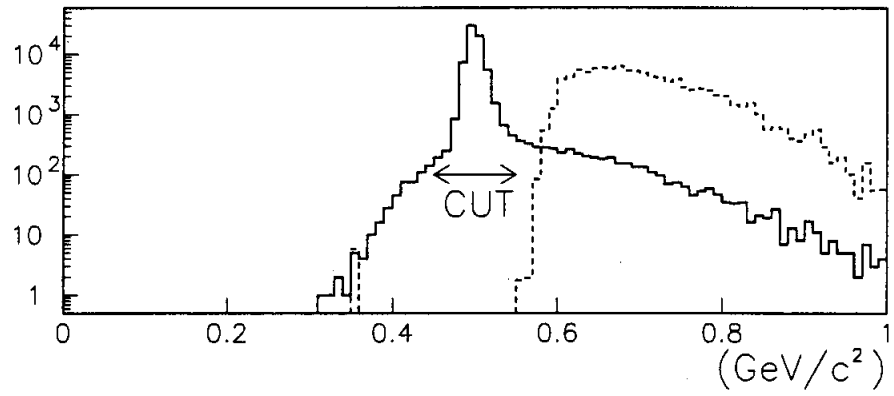

Figure 4.13: The $\pi^+\pi^-\gamma\gamma$ invariant mass distribution of $e^+e^-\gamma\gamma$ events. The solid line is data, and the dot one is the expectation from the $K_L \to e^+e^-\gamma\gamma$ Monte Carlo simulation with an arbitrary normalization.

Kaon Mass Selection

Figure 4.14 shows the $e^+e^-\gamma\gamma$ and $e^+e^-\gamma$ mass distributions for the $e^+e^-\gamma\gamma$ events and $e^+e^-\gamma$ events, respectively. By using the Monte Carlo simulation, the kaon mass window was set to be between 466 and 530 MeV/c^2 (2.3σ). We can see the $K_L \to e^+e^-\gamma$ peak in Figure 4.14, but not the $K_L \to e^+e^-\gamma\gamma$ signal at this stage.

In Figure 4.14, the scatter plots of $M_{ee\gamma\gamma}$ (and $M_{ee\gamma}$) versus M_{ee} distributions are shown for $K_L \to e^+e^-\gamma\gamma$, to isolate contributions from various backgrounds. As shown in Figure 4.14, the kaon mass region is dominated by the $K_L \to \pi^\pm e^\mp \nu(2\gamma)$ and the $K_L \to \pi^0\pi^0_D$ background. Figure 4.16 shows the scatter plots of M_{ee} versus $M_{ee\gamma}$ for the Monte Carlo simulation for $K_L \to e^+e^-\gamma$ and the major backgrounds, where the $K_L \to \pi^\pm e^\mp \nu(\gamma)$ background events dominated in the kaon mass region.

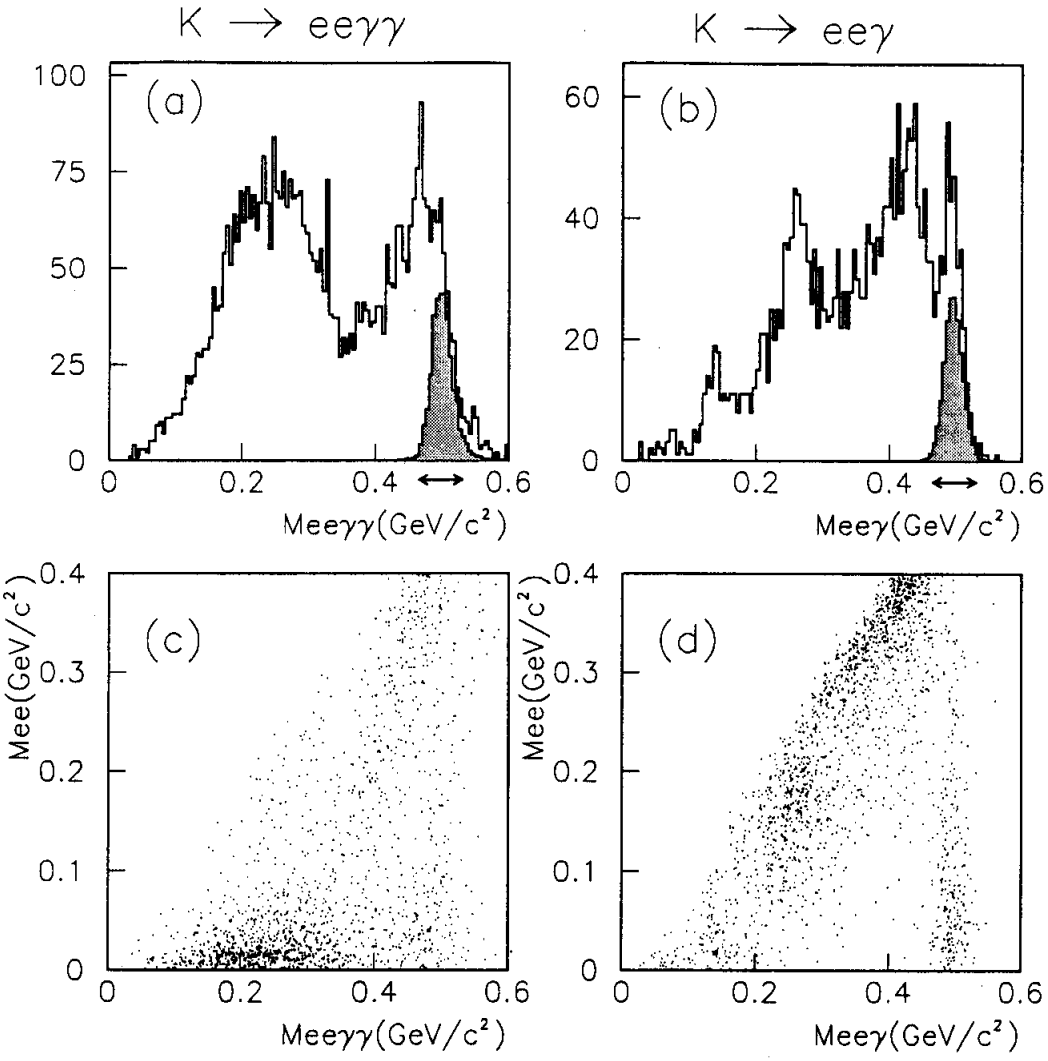

Figure 4.14: The $M_{ee\gamma\gamma}$ (a) and $M_{ee\gamma}$ (b) distributions. The expected signals from the Monte Carlo simulation are shown by shading with an arbitrary normalization where the selected kaon mass windows are shown by the arrows. In addition, the scatter plot of $M_{ee\gamma\gamma}$ versus M_{ee} distribution (c) and the scatter plot of $M_{ee\gamma}$ versus M_{ee} (d) are shown.

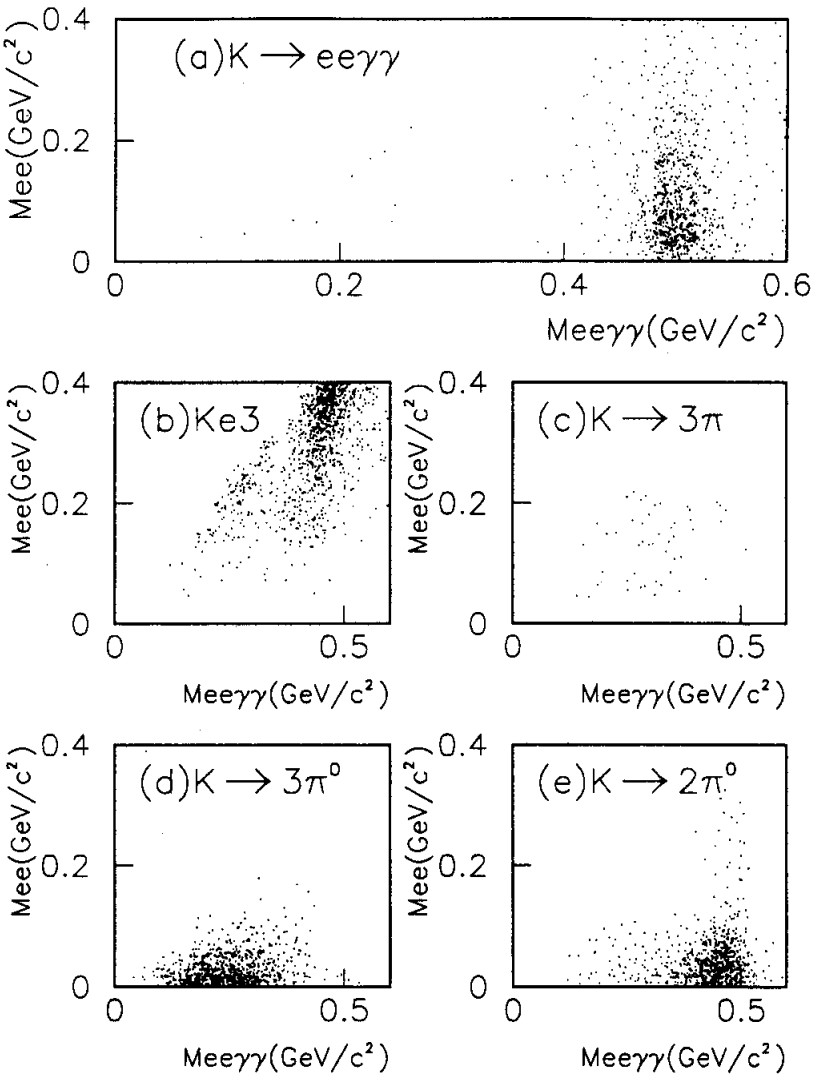

Figure 4.15: Scatter plot of $M_{ee\gamma\gamma}$ versus M_{ee} distributions for the Monte Carlo simulation for the signal $K_L \to e^+e^-\gamma\gamma$ (a), the backgrounds $K_L \to \pi^\pm e^\mp \nu(2\gamma)$ (b), $K_L \to \pi^+\pi^-\pi^0$(c), $K_L \to \pi^0\pi^0\pi^0_D$ (d) and $K_L \to \pi^0\pi^0_D$ (e). The populations of Monte Carlo events are arbitrary scales.

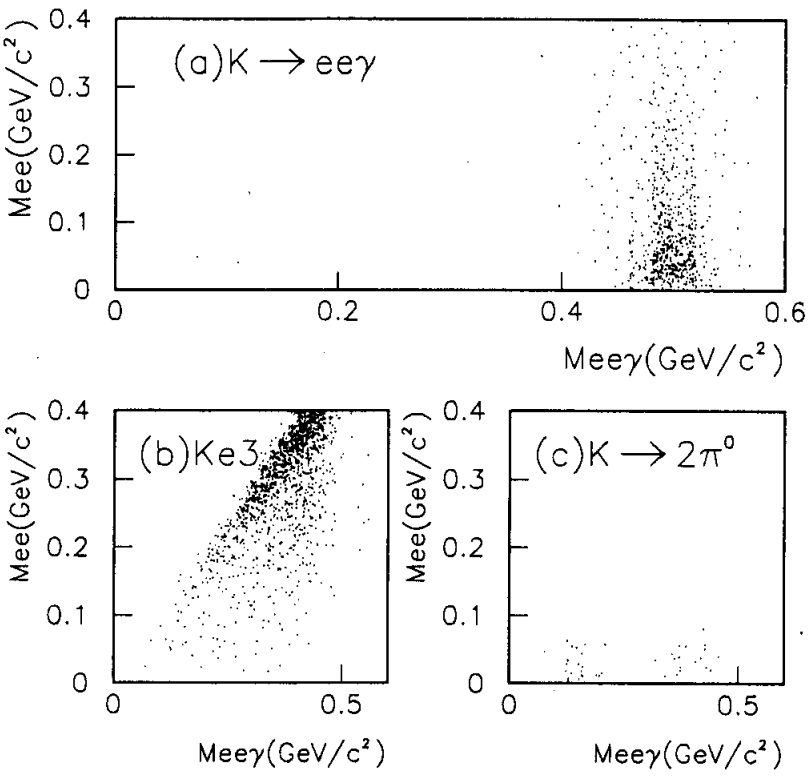

Figure 4.16: Scatter plot of $M_{ee\gamma}$ versus M_{ee} distributions for the Monte Carlo simulation for the signal $K_L \to e^+e^-\gamma$ (a), the backgrounds $K_L \to \pi^\pm e^\mp \nu(\gamma)$ (b) and $K_L \to 2\pi^0$(c). The populations of Monte Carlo events are arbitrary scales.

These plots show that additional cuts on the phase space distribution were necessary in order to extract the clean $e^+e^-\gamma\gamma$ and $e^+e^-\gamma$ samples.

4.2.3 Cut on Phase Space

Here, we will introduced phase space cuts which distinguishes $K_L \to e^+e^-\gamma\gamma$ decay from backgrounds. These cuts are based on the characteristics of the radiative Dalitz decay. Therefore, the direct emission contribution in the decay $K_L \to e^+e^-\gamma\gamma$ should be searched for without these cuts, as described in Chapter 6.

minΣcos Cut

A useful quantity distinguishes the Dalitz decay from $K_L \to \pi^\pm e^\mp \nu(2\gamma)$ background is minΣcos, which is defined as:

$$\text{min}\Sigma\text{cos} \;=\; \mathit{Minimum}(\cos\theta_{11} + \cos\theta_{21}, \cos\theta_{12} + \cos\theta_{22}),$$

where θ_{ij} is the angle between the ith electron and the jth photon in the center of mass frame of the kaon. Figure 4.17 shows the minΣcos distributions for both the data and the Monte Carlo simulation for $K_L \to e^+e^-\gamma\gamma$ and the $K_L \to \pi^\pm e^\mp \nu(2\gamma)$ background events. For the $K_L \to e^+e^-\gamma\gamma$, one of photons is usually emitted nearly

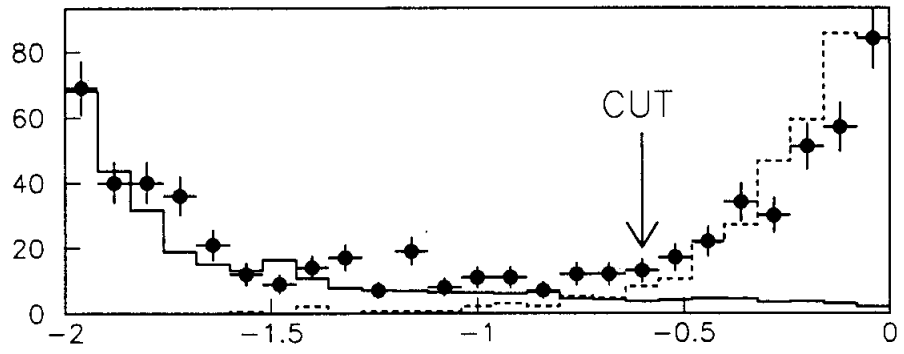

Figure 4.17: The minΣcos distribution for the $K_L \to e^+e^-\gamma\gamma$ sample and the Monte Carlo events. The data is shown by the dots with error bar. The $K_L \to e^+e^-\gamma$ Monte Carlo events are shown by the solid line, and they are normalized at the leftmost bin. The $K_L \to \pi^\pm e^\mp \nu(2\gamma)$ Monte Carlo events are shown by the dashed line, and they are normalized at the rightmost bin. The cut on the minΣcos is shown.

opposite to the e^+e^- momentum. Therefore, the angle between the photon and the

electrons should be close to π, which results in $min\Sigma cos \approx -2$ as shown in Figure 4.17. For the $K_L \to \pi^{\pm}e^{\mp}\nu(2\gamma)$ background, two charged particles tend to have a large opening angle and the photons are less correlated. Therefore, minΣ cos is close to 0, which is well separated from the signal events.

In order to keep the signal events as many as possible and to reject the $K_L \to \pi^{\pm}e^{\mp}\nu(2\gamma)$ background, the minΣ cos was required to be less than -0.6.

For the $K_L \to e^+e^-\gamma$ events, a very similar quantity was defined as:

$$\Sigma cos \;\; = \;\; \cos\theta_{11} + \cos\theta_{21},$$

where θ_{ij} is the angle between the ith electron and the $j(=1)$th photon in the center of mass frame of the kaon. Figure 4.18 shows the Σ cos distributions for the data and the Monte Carlo simulation for $K_L \to e^+e^-\gamma$ and $K_L \to \pi^{\pm}e^{\mp}\nu(\gamma)$. The

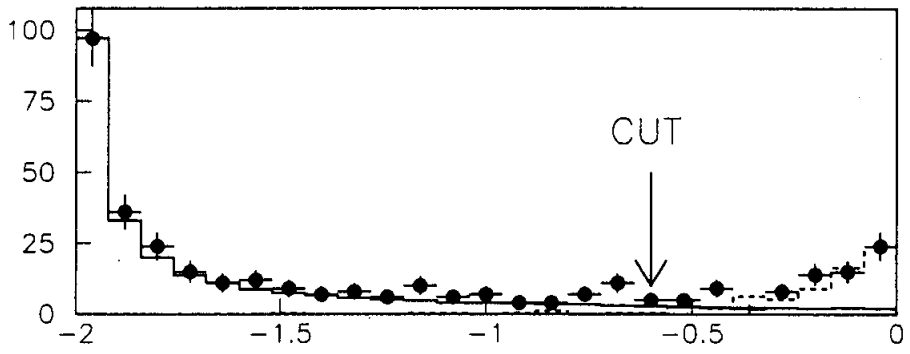

Figure 4.18: The Σ cos distributions for the $K_L \to e^+e^-\gamma$ sample and the Monte Carlo events. The data is shown by the dots with error bars. The $K_L \to e^+e^-\gamma$ Monte Carlo events are shown by the solid line, and they are normalized at the leftmost bin. The $K_L \to \pi^{\pm}e^{\mp}\nu(\gamma)$ Monte Carlo events are shown by the dashed line, and they are normalized at the rightmost bin. The cut on Σ cos is shown, too.

Σ cos was also required to be less than -0.6 in order to reject the $K_L \to \pi^{\pm}e^{\mp}\nu(\gamma)$ background.

Figure 4.19 shows the invariant mass distribution after this cut with the events without the kaon mass cut to show the background level. Although we can see the clean $K_L \to e^+e^-\gamma$ signal, we should impose an additional cut to the $e^+e^-\gamma\gamma$ events in order to extract clean $K_L \to e^+e^-\gamma\gamma$ events.

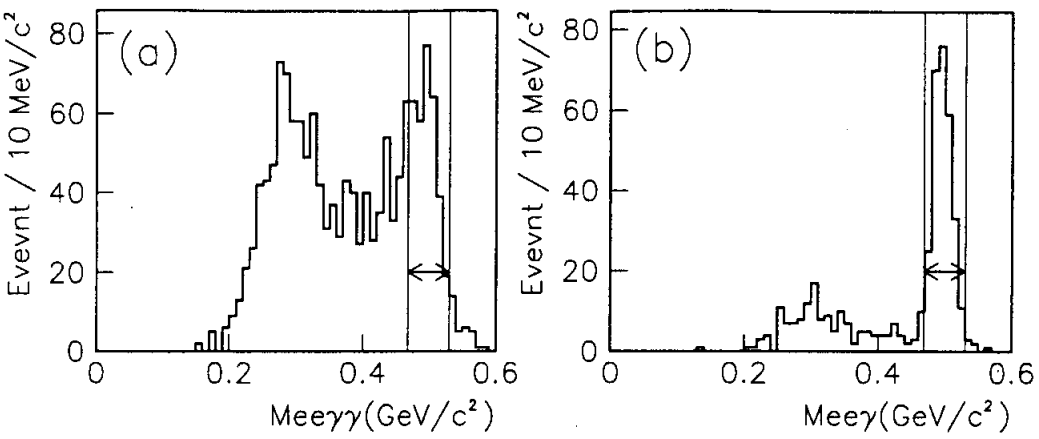

Figure 4.19: The $e^+e^-\gamma$ and $e^+e^-\gamma\gamma$ invariant mass distributions after $\Sigma\cos$ and $\min\Sigma\cos$ cuts without the kaon mass cut. The kaon mass window is shown, too.

θ_{min} Cut

An additional quantity introduced for the $e^+e^-\gamma\gamma$ events was :

$$\theta_{\min} = Minimum(\theta_{11}, \theta_{21}, \theta_{12}, \theta_{22}),$$

where the θ's were already defined above. θ_{min} is sensitive to the radiative decay. Figure 4.20 shows θ_{min} distributions for the data and Monte Carlo events for $K_L \to e^+e^-\gamma\gamma$ and major backgrounds.

The bremsstrahlung photon tends to be emitted in the same direction as the parent electron with a θ_{min} on the order of 10^{-1} radians. However there were no correlations for the angles in the background $K_L \to \pi^0\pi^0_D$. θ_{min} was required to be less than 0.5 radians in order to suppress the $K_L \to \pi^0\pi^0_D$ backgrounds. $M_{ee\gamma\gamma}$ distribution after this cut is shown in Figure 4.21.

Finally, we observed the clean kaon mass peak for the $e^+e^-\gamma\gamma$ events. However, we should note an additional background: the decay $K_L \to e^+e^-\gamma$ with external bremsstrahlung. This background has a peak at kaon mass as well as the decay $K_L \to e^+e^-\gamma\gamma$. The θ_{min} can additionally distinguish between internal and external bremsstrahlung since θ_{min} distribution of the external bremsstrahlung is peaked more sharply near 0. Therefore, θ_{min} was also required to be larger than 0.06 radians in order to suppress the $K_L \to e^+e^-\gamma$ events with external bremsstrahlung. Although this cut can suppress the $K_L \to e^+e^-\gamma$ events with external bremsstrahlung, this cut also decreases the $K_L \to e^+e^-\gamma\gamma$ acceptance by 56%. Therefore, we removed

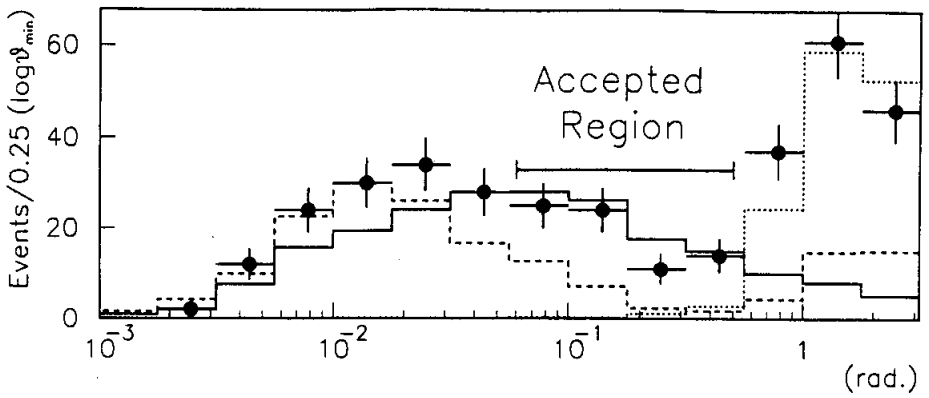

Figure 4.20: *The*θ_{min} distributions for the data and the Monte Carlo simulation. The data is shown by dots with the error bar. For the Monte Carlo events, the $K_L \to e^+e^-\gamma\gamma$ events, the $K_L \to e^+e^-\gamma$ events in the $e^+e^-\gamma\gamma$ events and the $K_L \to \pi^0\pi^0_D$ background are shown by the solid, dashed and dotted line, respectively. The Monte Carlo normalization were arbitrary for all decay modes. Final accepted region is shown there.

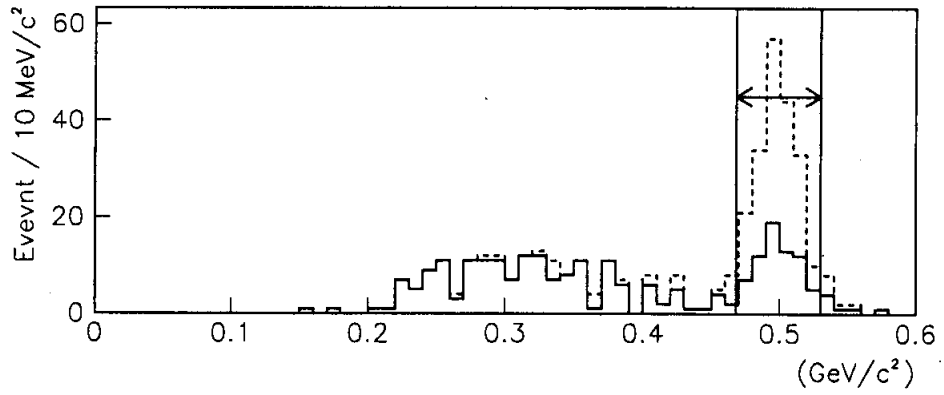

Figure 4.21: $M_{ee\gamma\gamma}$ invariant mass distributions. The solid line is the final sample to measure the branching ratio, and the dashed line is the sample with the less restrictive analysis. The region indicated by an arrow shows the kaon mass window.

this cut in some cases where more statistics was required. The analysis without this cut is referred to as "less restrictive analysis".

Finally, we observed 275 $e^+e^-\gamma$ events and 69 $e^+e^-\gamma\gamma$ events. The invariant mass distributions for the $e^+e^-\gamma\gamma$ and $e^+e^-\gamma\gamma$ events are shown in Figure 4.19 and Figure 4.21, respectively.

4.3 Background Estimation

Among the 275 obserbed $e^+e^-\gamma$ events, we estimated that there are 2.7 ± 1.0 background events, mostly from $K_L \to \pi^\pm e^\mp \nu(\gamma)$. We also estimated that there are 3.4 ± 0.4 $e^+e^-\gamma\gamma$ background events in the 69 $e^+e^-\gamma\gamma$ events; 2.4 ± 0.3 from $K_L \to \pi^0\pi^0_D$, 0.6 ± 0.2 from $K_L \to \pi^\pm e^\mp \nu(2\gamma)$, and 0.5 ± 0.2 from $K_L \to \pi^0\pi^0\pi^0_D$. After the background subtraction, the number of observed $K_L \to e^+e^-\gamma$ and $K_L \to e^+e^-\gamma\gamma$ decays are 272.3 ± 16.6 and 65.6 ± 8.3 events, respectively. There is also a mixture between $K_L \to e^+e^-\gamma$ and $K_L \to e^+e^-\gamma\gamma$ samples, but this will be disentangled in Section 5.1.

The background levels were estimated with the following general method. First, background decay modes were generated by Monte Carlo simulation, and analyzed in exactly the same way as data. For each background source, a kinematic region outside of the signal region where the background source was dominant was chosen. The number of data events in the same region was used to normalize the Monte Carlo events. The normalization took care of the uncertainty in particle misidentification probability etc.. The number of MC events in the signal region was scaled by the normalization factor to derive the number of background events in the signal region.

In the following subsections, we describe how the number of background events for $K_L \to e^+e^-\gamma$ and $K_L \to e^+e^-\gamma\gamma$ were estimated, in more detail.

4.3.1 Estimation of Background to $e^+e^-\gamma$ Events

In case of the $e^+e^-\gamma$ events, the $K_L \to \pi^\pm e^\mp \nu(\gamma)$ was the only main background source. In order to normalize this MC background events to data, the Σcos distribution was used. Figure 4.22 shows the Σcos distribution for the data, the $K_L \to e^+e^-\gamma$ MC events, and the $K_L \to \pi^\pm e^\mp \nu(\gamma)$ background MC events, without the cut on /nsc.

In Section 4.2, Σcos in the range between the -2.0 and -0.6 was selected as the $K_L \to e^+e^-\gamma$ signal region. Therefore, the $K_L \to \pi^\pm e^\mp \nu(\gamma)$ MC background events were normalized in the region of $\Sigma\cos > -0.6$ where the $K_L \to \pi^\pm e^\mp \nu(\gamma)$ background events are dominant. The number of data and MC events in both signal and normalization regions are listed in Table 4.1. The estimated contribution of the $K_L \to e^+e^-\gamma$ to the $\Sigma\cos > -0.6$ region was about 20 events. From these numbers, the normalization factor of the $K_L \to \pi^\pm e^\mp \nu(\gamma)$ MC events was found to be $(75 - 20) \div 140 = 0.39$.

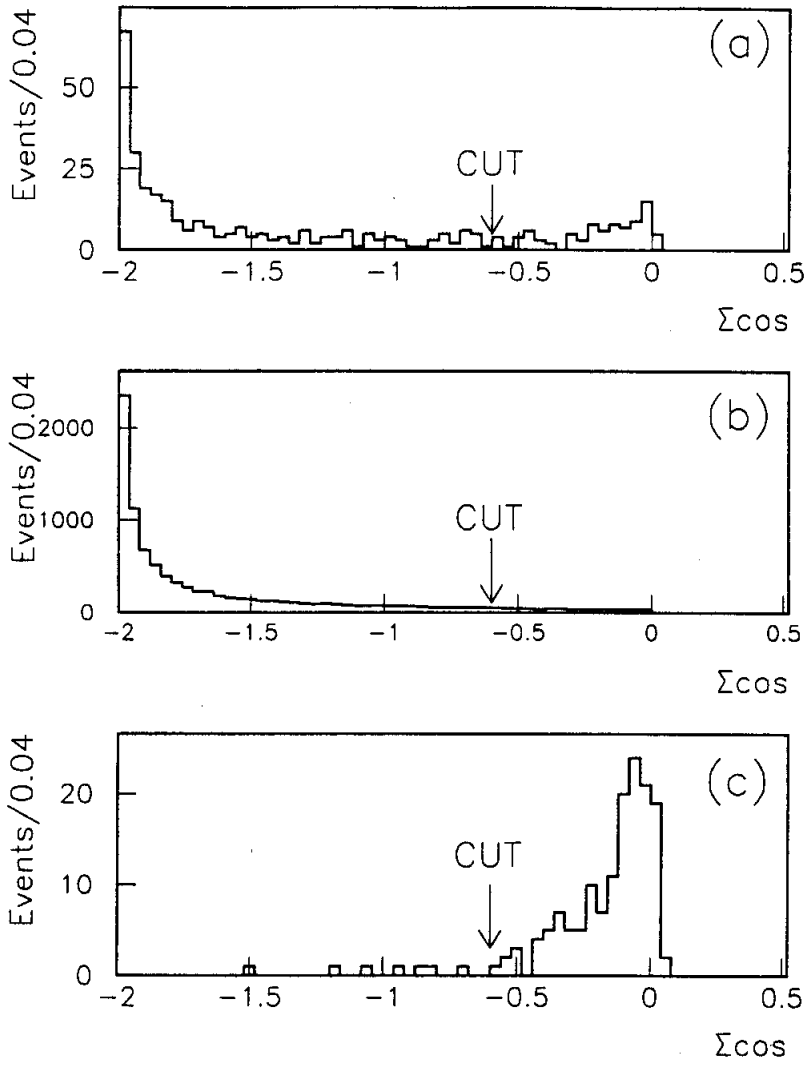

Figure 4.22: Σ cos distributions for the $e^+e^-\gamma$ events (a), the $K_L \to e^+e^-\gamma$ MC (b) and the $K_L \to \pi^\pm e^\mp \nu(\gamma)$ background MC (c) without the Σ cos cut. The background $K_L \to \pi^\pm e^\mp \nu(\gamma)$ was normalized at the region outside of the signal region.

Table 4.1: The Number of data and MC events for $e^+e^-\gamma$ events in both signal region ($-2.0 < \Sigma\cos < -0.6$) and normalization region ($-0.6 < \Sigma\cos$).

Events	Number of events	
	$-2.0 < \Sigma\cos < -0.6$	$-0.6 < \Sigma\cos$
DATA	275	75
MC: $K_L \to e^+e^-\gamma$	8461	636
MC: $K_L \to \pi^\pm e^\mp \nu$	7	140

After imposing all the final cuts for selecting $e^+e^-\gamma$ events, 7 $K_L \to \pi^\pm e^\mp \nu(\gamma)$ MC events remained. Therefore, the number of $K_L \to \pi^\pm e^\mp \nu(\gamma)$ background was estimated to be $7 \times 0.39 = 2.7 \pm 1.0$ events[1]. After the correction, the number of the $e^+e^-\gamma$ events was reduced to 272.3 ± 16.6 events from 275 events.

4.3.2 Estimation of Background to $e^+e^-\gamma\gamma$ Events

We estimate background to $K_L \to e^+e^-\gamma\gamma$ decay in this section. In order to reduce the statistical error on the normalization factor, we removed θ_{min}, min$\Sigma\cos$ and kaon mass cuts. Figure 4.23 and Figure 4.24 show the total invariant mass and the e^+e^- invariant mass distributions for the data and each background Monte Carlo events.

As the background normalization regions, two regions in $M_{ee\gamma\gamma}$, $0.2 \le M_{ee\gamma\gamma}(GeV/c^2) \le 0.4$ (M_{Low}) and $0.4 \le M_{ee\gamma\gamma}(GeV/c^2) \le 0.46$ (M_{High}), and two regions in M_{ee}, $0 \le M_{ee}(GeV/c^2) \le 0.12$ ($M_{ee}[\pi^0]$) and $0.3 \le M_{ee}(GeV/c^2) \le 0.45$ ($M_{ee}[K_{e3}]$) were selected. The number of events for data and MC backgrounds in each normalization region are listed in Table 4.2. As an example, the 651 $K_L \to \pi^\pm e^\mp \nu(2\gamma)$ MC events and 351 data events were observed in the region of ($M_{High}\&M_{ee}[K_{e3}]$). Therefore, the $K_L \to \pi^\pm e^\mp \nu(2\gamma)$ MC normalization factor was determined to $351 \div 651 = 0.54$. Similarly, the $K_L \to \pi^0\pi^0_D$ and $K_L \to \pi^0\pi^0\pi^0_D$ MC normalization factors were determined to 0.0575 and 1.13, respectively.

Once we determined the normalization factors, we can estimate the number of background events in the final 69 $e^+e^-\gamma\gamma$ events with all the cuts in Section 4.2. For $K_L \to \pi^0\pi^0_D$ background, 42 MC events passed all the cuts which were used to select the final $e^+e^-\gamma\gamma$ sample. Therefore, the number of $K_L \to \pi^0\pi^0_D$ background was estimated to be $42 \times 0.0575 = 2.4 \pm 0.3$ events. In case of $K_L \to \pi^\pm e^\mp \nu(2\gamma)$ and $K_L \to \pi^0\pi^0\pi^0_D$ backgrounds, we used a slightly different technique to increase statistics. First, we applied all the cuts which we used for the final selection, except for the fusion cut, to the MC background events. We then corrected for the rejection factor for fusion cut. For $K_L \to \pi^\pm e^\mp \nu(2\gamma)$ background, 6 MC events passed such

[1]This number is slightly different from the value, 2.3 ± 0.9, in the reference [42] because the p_t^2 cut was relaxed at the reference for this background estimation.

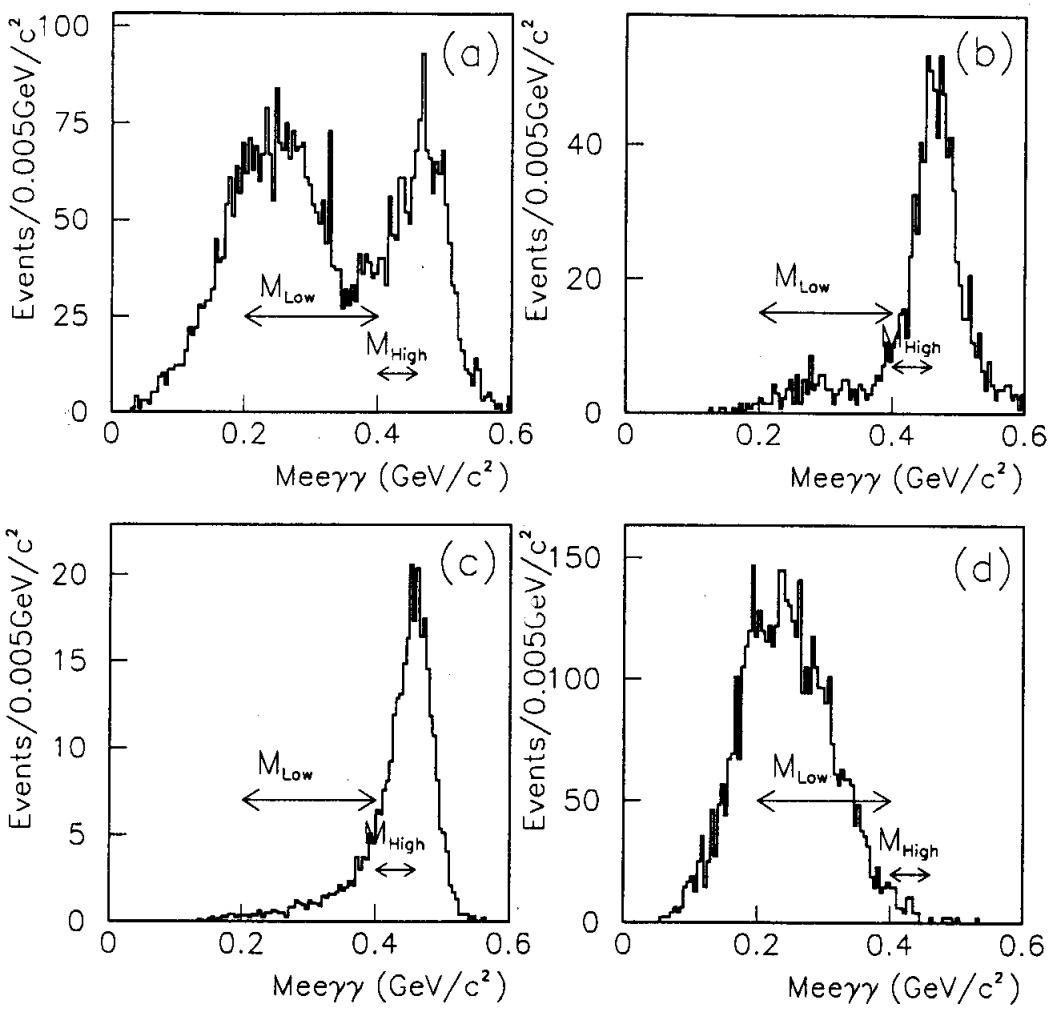

Figure 4.23: The total mass distributions for the $e^+e^-\gamma\gamma$ events and each background MC events without θ_{min}, minΣcos and the kaon mass cuts. (a) Data, (b) $K_L \to \pi^{\pm}e^{\mp}\nu(2\gamma)$ MC, (c) $K_L \to \pi^0\pi^0_D$ MC and (d) $K_L \to \pi^0\pi^0\pi^0_D$ MC events are shown above. The selected regions used for the normalization are shown by the arrows where the labels "M_{Low}" and the "M_{High}" show the selected low and high mass region, respectively.

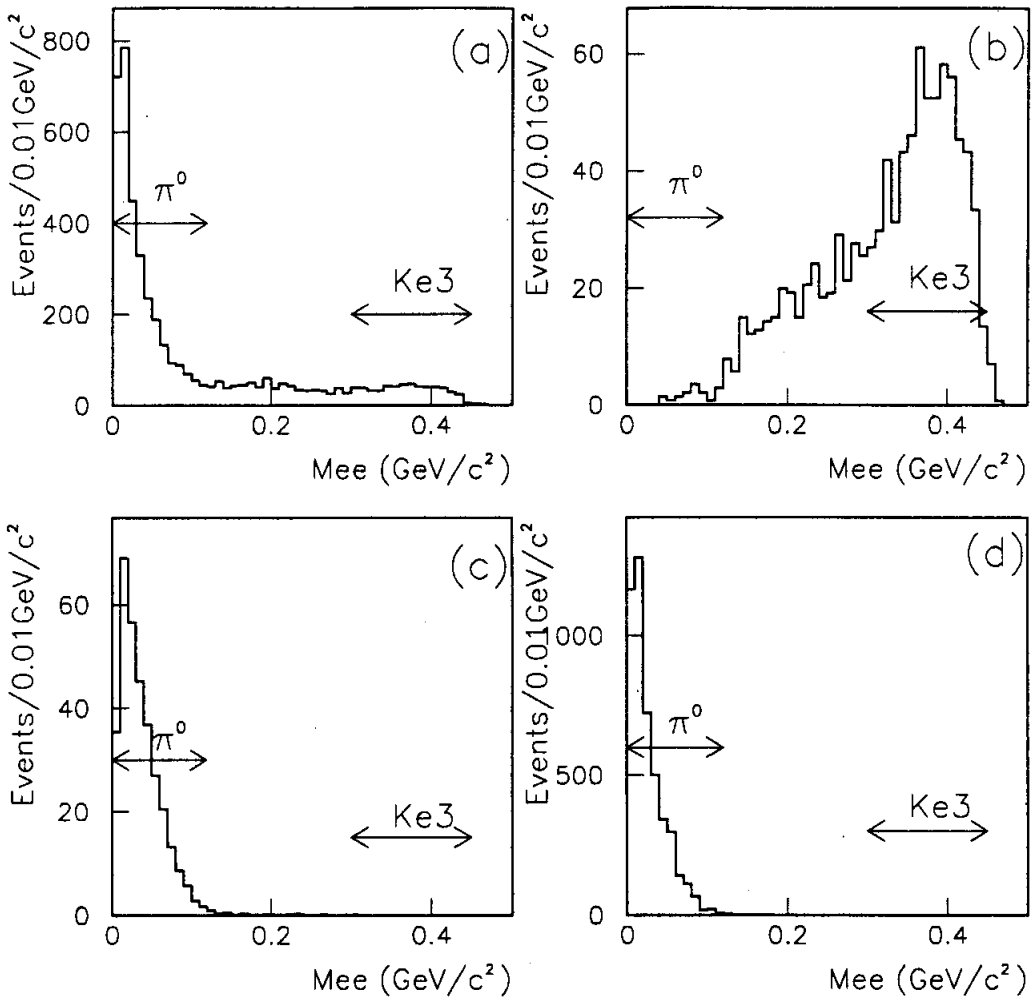

Figure 4.24: The e^+e^- mass distributions for the $e^+e^-\gamma\gamma$ events and each background MC events without θ_{min}, minΣcos and the kaon mass cuts. (a) Data, (b) $K_L \to \pi^\pm e^\mp \nu(2\gamma)$ MC, (c) $K_L \to \pi^0\pi^0_D$ MC and (d) $K_L \to \pi^0\pi^0\pi^0_D$ MC events are shown above. The selected regions used for the normalization are shown by the arrows where the labels "π^0" and the "$Ke3$" show the selected regions of $M_{ee}[\pi^0]$ and $M_{ee}[K_{e3}]$, respectively.

Table 4.2: The Number of MC background events and data events for $e^+e^-\gamma\gamma$ events in each normalization region. The regions of M_{Low} and M_{High} are defined as $0.2 \leq M_{ee\gamma\gamma}(GeV/c^2) \leq 0.4$ and $0.4 \leq M_{ee\gamma\gamma}(GeV/c^2) \leq 0.46$, respectively. The regions of $M_{ee}[\pi^0]$ and $M_{ee}[K_{e3}]$ are defined as $0 \leq M_{ee}(GeV/c^2) \leq 0.12$ and $0.3 \leq M_{ee}(GeV/c^2) \leq 0.4$, respectively.

Background	#event without normalization		
	$M_{Low}\&M_{ee}[\pi^0]$	$M_{High}\&M_{ee}[\pi^0]$	$M_{High}\&M_{ee}[K_{e3}]$
$K_L \to \pi^\pm e^\mp \nu(2\gamma)$	4	1	651
$K_L \to \pi^0\pi^0_D$	1286	3195	0
$K_L \to \pi^0\pi^0\pi^0_D$	1556	33	0
DATA	1832	221	351

cuts. Monte Carlo simulation predicts the rejection power of the fusion cut to be 0.186 for the $K_L \to \pi^\pm e^\mp \nu(2\gamma)$ background. Therefore, the number of $K_L \to \pi^\pm e^\mp \nu(2\gamma)$ background was estimated to be $6 \times 0.186 \times 0.54 = 0.6 \pm 0.2$ events. For $K_L \to \pi^0\pi^0\pi^0_D$ background, 10 MC events passed such cuts. The rejection power of the fusion cut was estimated by MC to be 0.045 for the $K_L \to \pi^0\pi^0\pi^0_D$ background. Therefore, the number of $K_L \to \pi^0\pi^0\pi^0_D$ background was estimated to be $10 \times 0.045 \times 1.13 = 0.5 \pm 0.2$ events.

To conclude, the contribution from these backgrounds to the signal region was estimated to be 2.4 ± 0.3 events from $K_L \to \pi^0\pi^0_D$, 0.6 ± 0.2 events from $K_L \to \pi^\pm e^\mp \nu(2\gamma)$ and 0.5 ± 0.2 events from $K_L \to \pi^0\pi^0\pi^0_D$.

4.4 Summary

As the summary of the event selection, the number and the fraction of the events which passed each stage is shown in Table 4.3. The table also shows the fraction of the $K_L \to e^+e^-\gamma\gamma$ and the $K_L \to e^+e^-\gamma$ MC events kept at each stage. After correcting for the background events, there remained 272.3 ± 16.6 $e^+e^-\gamma$ events and 65.6 ± 8.3 $e^+e^-\gamma\gamma$ events.

Table 4.3: Number (fraction) of events passing at each stage in this analysis. The fraction is shown by the parentheses. The fraction of the $K_L \to e^+e^-\gamma\gamma$ and the $K_L \to e^+e^-\gamma$ MC events are also listed.

	The Number (Fraction) Kept DATA		Fraction Kept Monte Carlo	
CUT	$e^+e^-\gamma\gamma$	$e^+e^-\gamma$	$e^+e^-\gamma\gamma$	$e^+e^-\gamma$
Trigger	176,376,610(1.00)		1.00	1.00
	Event Reconstruction			
Track Finding	(0.20)		0.85	0.81
Cluster Finding	(0.12)	(0.032)	0.77	0.79
Track-Cluster Matching	(0.094)	(0.028)	0.73	0.78
E/p Cut	(8.0×10^{-3})	(3.2×10^{-3})	0.64	0.70
Vertex Fitting	(7.2×10^{-3})	(2.8×10^{-3})	0.61	0.65
Fiducial Cut	(4.5×10^{-3})	(1.9×10^{-3})	0.57	0.58
Trigger Verification	(4.1×10^{-3})	(1.8×10^{-4})	0.51	0.49
Photon Veto Cut	(3.3×10^{-3})	(1.5×10^{-4})	0.45	0.45
Same Trigger Requirement	(3.3×10^{-3})	(8.2×10^{-4})	0.45	0.40
Fusion Cut	(8.6×10^{-4})	(3.2×10^{-4})	0.26	0.29
Summary	151,700	56,965	0.26	0.29
	Event Selection			
$p_t^2 \leq 1000(\mathrm{MeV/c^2})$	71,817 (3.3×10^{-4})	5,001 (2.8×10^{-5})	0.20	0.23
$K_L \to \pi^+\pi^-\pi^0$ Cut	5,012 (2.8×10^{-5})	5,001 (2.8×10^{-5})	0.20	0.23
Kaon Mass Cut	655 (3.7×10^{-6})	350 (2.0×10^{-6})	0.18	0.22
$\Sigma\cos$ or $\min\Sigma\cos$	349 (2.0×10^{-6})	275 (1.6×10^{-6})	0.17	0.20
θ_{min} (Less Restrictive)	203 (1.2×10^{-6})	275 (1.6×10^{-6})	0.15	0.20
θ_{min} Cut	69 (3.9×10^{-7})	275 (1.6×10^{-6})	0.064	0.20

Chapter 5

Measurement of the Branching Ratio

In this chapter, results of the $K_L \to e^+e^-\gamma\gamma$ branching ratio measurement are presented. The way to extract the branching ratio for the radiative Dalitz $K_L \to e^+e^-\gamma\gamma$ decay is described in Section 5.1. The systematic uncertainties in this measurement are described in Section 5.2 in detail. Finally, by relaxing θ_{min} cut, we show some phase space variables for this decay in Section 5.3.

5.1 Measurement of the Branching Ratio

After the background subtraction, the number of the $e^+e^-\gamma\gamma$ events and the $e^+e^-\gamma$ events were 65.6 ± 8.3 and 272.3 ± 16.6, respectively. However, these are not directly the number of the $K_L \to e^+e^-\gamma\gamma$ and the $K_L \to e^+e^-\gamma$ events. Some $K_L \to e^+e^-\gamma$ decay with an external bremsstrahlung will be identified as $e^+e^-\gamma\gamma$ events. On the other hand, if a photon from $K_L \to e^+e^-\gamma\gamma$ decay did not have enough energy to make a cluster in the calorimeter or missed the calorimeter, the decay will be identified as $e^+e^-\gamma$ events. We disentangled these decays by the following method.

Let us define $R = BR(K_L \to e^+e^-\gamma\gamma)/BR(K_L \to e^+e^-\gamma)$ where the branching ratio, $BR(K_L \to e^+e^-\gamma)$, includes its radiative decay, $K_L \to e^+e^-\gamma\gamma$. Of course, the variable, R, is a function of the cutoff energy for the radiative photon. The number of observed $e^+e^-\gamma\gamma$ events is formulated by using the branching ratio, $BR(K_L \to e^+e^-\gamma)$, as:

$$\begin{aligned} N_{e^+e^-\gamma\gamma} &= \#K_L \times (1-R) \times BR(K_L \to e^+e^-\gamma) \times A_{ee\gamma \to ee\gamma\gamma} \\ &\quad + \#K_L \times R \times BR(K_L \to e^+e^-\gamma) \times A_{ee\gamma\gamma \to ee\gamma\gamma}, \end{aligned} \tag{5.1}$$

where $\#K_L$ is the kaon flux in the experiment and the $A_{x \to y}$ is the probability that the decay $K_L \to x$ is observed as the event y, which is referred to as "acceptance". In Equation 5.1, the first term represents the number of the $K_L \to e^+e^-\gamma$ events in

the $e^+e^-\gamma\gamma$ events, and the second term represents the number of the $K_L \to e^+e^-\gamma\gamma$ signal events in the $e^+e^-\gamma\gamma$ events. Similarly, the number of the $e^+e^-\gamma$ events is formulated as :

$$\begin{aligned} N_{e^+e^-\gamma} &= \#K_L \times (1-R) \times BR(K_L \to e^+e^-\gamma) \times A_{ee\gamma \to ee\gamma} \\ &\quad + \#K_L \times R \times BR(K_L \to e^+e^-\gamma) \times A_{ee\gamma\gamma \to ee\gamma}. \end{aligned} \tag{5.2}$$

The acceptances were determined from the MC simulation with energies of the kaon between 35 and 220 GeV and the decay points between 90 and 160 m from the target. Additionally, $M_{\gamma\gamma}$ threshold to distinguish the decays $K_L \to e^+e^-\gamma\gamma$ from $K_L \to e^+e^-\gamma$ was set to be $2.29 MeV/c^2$ which is explained in Section 3.2.1. Each acceptance is shown in Table 5.1.

Table 5.1: The acceptance for each decay mode. The acceptance of observed $ee\gamma$ events includes a trigger prescale factor of 1/14.

Decay Mode	Acceptances (10^{-4})	
	$ee\gamma$	$ee\gamma\gamma$
$K_L \to ee\gamma$	9.2	0.44
$K_L \to ee\gamma\gamma$	13.1	7.6

Now since there are two unknown parameters, R and $\#K_L$, in two equations, we can solve the equation. By dividing Equation 5.1 by Equation 5.2, we get the new equation:

$$\frac{N_{ee\gamma\gamma}}{N_{ee\gamma}} = \frac{(1-R) \times A_{ee\gamma \to ee\gamma\gamma} + R \times A_{ee\gamma\gamma \to ee\gamma\gamma}}{(1-R) \times A_{ee\gamma \to ee\gamma} + R \times A_{ee\gamma\gamma \to ee\gamma}}. \tag{5.3}$$

This equation has just one unknown parameter, R. Since the same photon energy cutoff is used for R and acceptances, the ratio $N_{ee\gamma\gamma}/N_{ee\gamma}$ is independent of the cutoff energy for the radiative photon. By using the acceptances in Table 5.1 and the observed numbers of the $e^+e^-\gamma\gamma$ and the $e^+e^-\gamma$ events, the variable R is measured by solving Equation 5.3 as:

$$\begin{aligned} \frac{65.6 \pm 8.3}{272.3 \pm 16.6} &= \frac{(1-R) \times 0.44 \times 10^{-4} + R \times 7.6 \times 10^{-4}}{(1-R) \times 9.2 \times 10^{-4} + R \times 13.1 \times 10^{-4}} \\ R &= 0.29 \pm 0.06. \end{aligned} \tag{5.4}$$

By substituting R by 0.29 ± 0.06 in Equation 5.1 or Equation 5.2, the kaon flux, $\#K_L$, is measured to be $(2.89 \pm 0.19) \times 10^{10}$. As mentioned earlier, the first and the second terms on the right side of Equation 5.1 represent the number of the $K_L \to e^+e^-\gamma$ events in the $e^+e^-\gamma\gamma$ events and the number of the $K_L \to e^+e^-\gamma\gamma$

signal events in the $e^+e^-\gamma\gamma$ events, respectively. Thus, the observed 65.6 $e^+e^-\gamma\gamma$ events consist of $57.3 \pm 8.5(stat.)$ $K_L \to e^+e^-\gamma\gamma$ decays and $8.3 \pm 2.0(stat.)$ $K_L \to e^+e^-\gamma$ decays. Similarly, the 272.3 ± 16.6 $e^+e^-\gamma$ events consist of $173.3 \pm 23.4(stat)$ $K_L \to e^+e^-\gamma$ decays and $98.9 \pm 17.0(stat)$ $K_L \to e^+e^-\gamma\gamma$ decays. The observed $K_L \to e^+e^-\gamma\gamma$ decay is about three times larger than the number obtained in the previous experiment [20] and this is the most rich sample of the decay $K_L \to e^+e^-\gamma\gamma$.

By using the inclusive branching ratio of $BR(K_L \to e^+e^-\gamma) = (9.1 \pm 0.5) \times 10^{-6}$ [43], the branching ratio of the decay $K_L \to e^+e^-\gamma\gamma$ is obtained straightforwardly from the definition of the parameter R as:

$$\begin{aligned} & BR(K_L \to e^+e^-\gamma\gamma, \mathrm{M}_{\gamma\gamma} > 2.29\mathrm{MeV/c^2}) \\ &= R \times BR(K_L \to e^+e^-\gamma) \\ &= [0.29 \pm 0.06(stat)] \times [(9.1 \pm 0.5) \times 10^{-6}] \\ &= [2.6 \pm 0.55(stat)] \times 10^{-6}. \end{aligned}$$

Now we have all the variables which we want.

In the previous experiment and the theoretical calculation, the applied cutoff energy for a photon was 5MeV in the center of mass frame of the kaon. In order to allow direct comparison between this measurement and theoretical prediction [1] as well as the previous published measurement [20], the branching ratio must be presented with the same cutoff energy. The spectrum of the minimum energy photon is shown in Figure 5.1 for our $K_L \to e^+e^-\gamma\gamma$ Monte Carlo events. The ratio of the $K_L \to e^+e^-\gamma\gamma$ branching ratios with the two different cutoffs was calculated to be

$$BR(K_L \to e^+e^-\gamma\gamma, E_\gamma^* \geq 5 \text{ MeV})/BR(K_L \to e^+e^-\gamma\gamma, \mathrm{M}_{\gamma\gamma} > 2.29\mathrm{MeV/c^2}) = 0.247,$$

where E_γ^* is the minimum energy of photons in the center of mass frame of the kaon. Therefore, the measured branching ratio of the decay $K_L \to e^+e^-\gamma\gamma$ with the photon energy cutoff of 5 MeV is:

$$BR(K_L \to e^+e^-\gamma\gamma, E_\gamma^* \geq 5 \text{ MeV}) = [6.5 \pm 1.2(stat)] \times 10^{-7}. \qquad (5.5)$$

This result is consistent with both the previous measurement, $BR = (6.6 \pm 3.2) \times 10^{-7}$ [20] and the theoretical prediction, $BR = (5.8 \pm 0.27) \times 10^{-7}$ [1].

5.2 Systematic Errors

The main sources of systematic errors come from uncertainties in normalization, detector resolution, background estimation and Monte Carlo simulation. All systematic errors are summarized in Table 5.2. By adding all individual components in quadrature, the total systematic error was calculated to be 8.5%. With this total

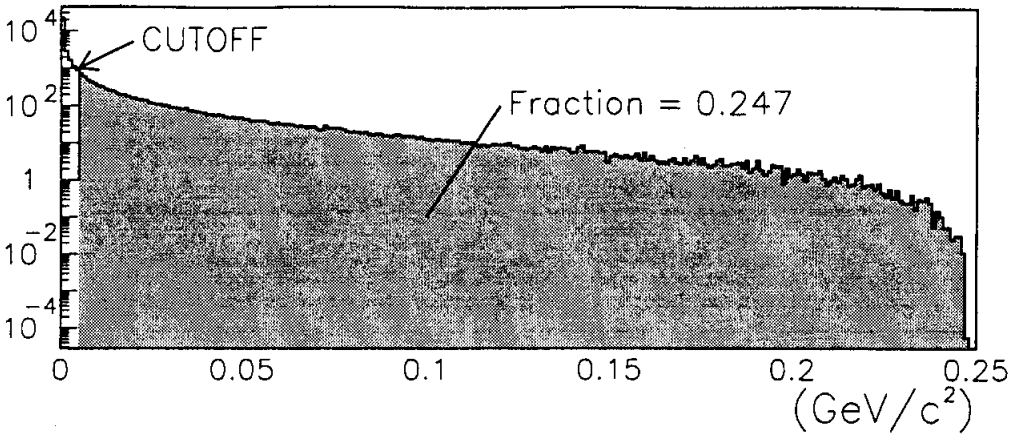

Figure 5.1: The spectrum of the minimum energy photon in our $K_L \to e^+e^-\gamma\gamma$ Monte Carlo events. The 5 MeV cutoff for the photon, the events passed this cutoff (shaded) and the fraction are shown, too.

systematic error, the final result of the branching ratio of the decay $K_L \to e^+e^-\gamma\gamma$ is deduced to be:

$$BR(K_L \to e^+e^-\gamma\gamma, E_\gamma^* \geq 5 \text{ MeV}) = [6.5 \pm 1.2(stat) \pm 0.6(syst)] \times 10^{-7} (5.6)$$

In the following subsections, each source of systematic error is described in detail.

5.2.1 $K_L \to e^+e^-\gamma$ Branching Ratio

The lack of the knowledge of the normalization decay mode, $K_L \to e^+e^-\gamma$, causes systematic error. The uncertainty in the $K_L \to e^+e^-\gamma$ branching ratio, $(9.1 \pm 0.5) \times 10^{-6}$, caused the 5.5% systematic error.

5.2.2 The Material of the Detector

The uncertainty in the amount of the detector material changes the probability of emitting a bremsstrahlung photon, or the expectation of the $K_L \to e^+e^-\gamma$ events in the $e^+e^-\gamma\gamma$ events with bremsstrahlung. In order to study the uncertainty, the probability of emitting a bremsstrahlung photon was studied experimentally by using the special electron calibration data which is described in Section 2.6.2. There was a 20% descrepancy in the probability between the data and the Monte Carlo

Table 5.2: Sources of the systematic error for the measurement of $BR(K_L \to e^+e^-\gamma\gamma)$.

The source of systematic error	error (%)
Branching ratio of $K_L \to ee\gamma$	5.5
Amount of material upstream of the analysis magnet	3.5
Monte Carlo statistics	3.4
Form factor of $K_L \to ee\gamma$	2.2
Position resolution for the photon candidates	2.2
Fusion cut	1.5
Uncertainty in the energy measurement	1.5
Uncertainty in the momentum measurement	1.0
Background subtraction	0.7
Total	8.5

simulation. This discrepancy was used as the uncertainty in the amount of the material upstream the magnet. Due to this uncertainty, the 3.5% systematic error was assigned to the $K_L \to e^+e^-\gamma\gamma$ branching ratio through the following equation:

$$\delta BR(K_L \to e^+e^-\gamma\gamma) = \frac{BR(K_L \to e^+e^-\gamma)}{A_{ee\gamma\gamma\to ee\gamma\gamma} - (N_{ee\gamma\gamma}/N_{ee\gamma}) \times A_{ee\gamma\gamma\to ee\gamma}} \times (1 - \frac{BR(K_L \to e^+e^-\gamma\gamma)}{BR(K_L \to e^+e^-\gamma)})^2 \times (\delta A_{ee\gamma\to ee\gamma\gamma}). \quad (5.7)$$

This equation is easily derived by using Equation 5.3.

The procedure on how to measure the amount of detector material by using the special electron calibration data is described in the following.

Special Electron Calibration Data

The Special Electron Calibration Data consisted of mainly pairs of an electron and a positron generated by the photon conversion upstream of the decay volume, where some of them generated external bremsstrahlung photons in the decay volume. The details of the special electron calibration run is described in Section 2.6. The ratio between the number of electron-positron pairs and the number of pairs with a bremsstrahlung photon is used to deduce the probability for emitting external bremsstrahlung.

The electrons and positrons in the pair were split vertically by the magnet located at 119 m downstream from the target, and horizontally by other magnet at 142 m and the analyzing magnet at 169 m. The illumination on the calorimeter for one magnet setting is shown in Figure 5.2. In the analysis, the basically two electron

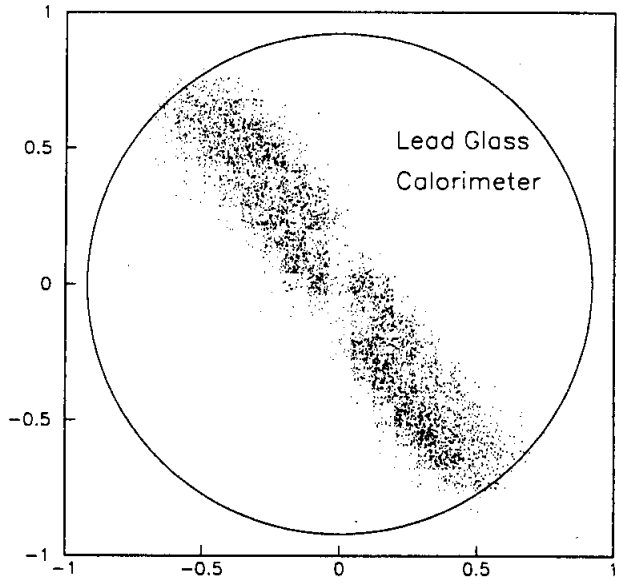

Figure 5.2: The typical illumination on the calorimeter in the special electron calibration run. The circle shows the outline of the lead glass calorimeter. By changing the ratio of horizontal to vertical momentum kicks of the magnets, the bands of electrons pairs rotated on the calorimeter.

events or two electrons and a photon events were accepted. In order to select these events, the following cuts were imposed.

1. The number of the clusters was two or three, and there were two charged clusters.
2. The number of tracks was at least two in both the x-view and y-view.
3. The E/p of electrons was required to be between 0.8 and 1.2.
4. The p_t^2 was required to be less than 0.001 GeV/c^2.
5. There were no hits in the MU1 counter.
6. The fusion cut was imposed.
7. The energy of each particle was greater than 2.5GeV to be same as the normal run.
8. The events with the e^+e^- invariant mass less than 20MeV/c^2 were discarded to suppress the photon conversion events in the detector.
9. The events with the cluster on the pipe blocks were discarded to suppress the accidental activities and to avoid the energy leakage from the side.
10. The total energy was required to be less than 45GeV which was the energy range of the parent photons.
11. The distance on the calorimeter between the photon cluster and the extrapolated position from the upstream track was required to be less than 5cm in order to select the events with an external bremsstrahlung photon.

The distributions of some basic variables are shown in Figure 5.3 and Figure 5.4 for the two electron events and the two electron with a photon events, respectively. The consistency between data and Monte Carlo simulation was good except for the z vertex distribution where there were unknown tails in the Monte Carlo simulation. The total invariant mass and the z vertex distributions have many peaks because of several magnet current settings. The number of the Monte Carlo events was normalized to the total number of events. The normalization factors for the two samples are shown in Table 5.3. The ratio between the number of three clusters and two clusters differ by 20%, between data and Monte Carlo.

This discrepancy between the normalization factors was not caused by the acceptance for bremsstrahlung photon, since the energy distribution of bremsstrahlung photons is consistent between the data and MC as shown in Figure 5.5.

The discrepancy in the emitting probability of the bremsstrahlung photon, 20%, was assigned to the uncertainty in the amount of the material upstream the magnet.

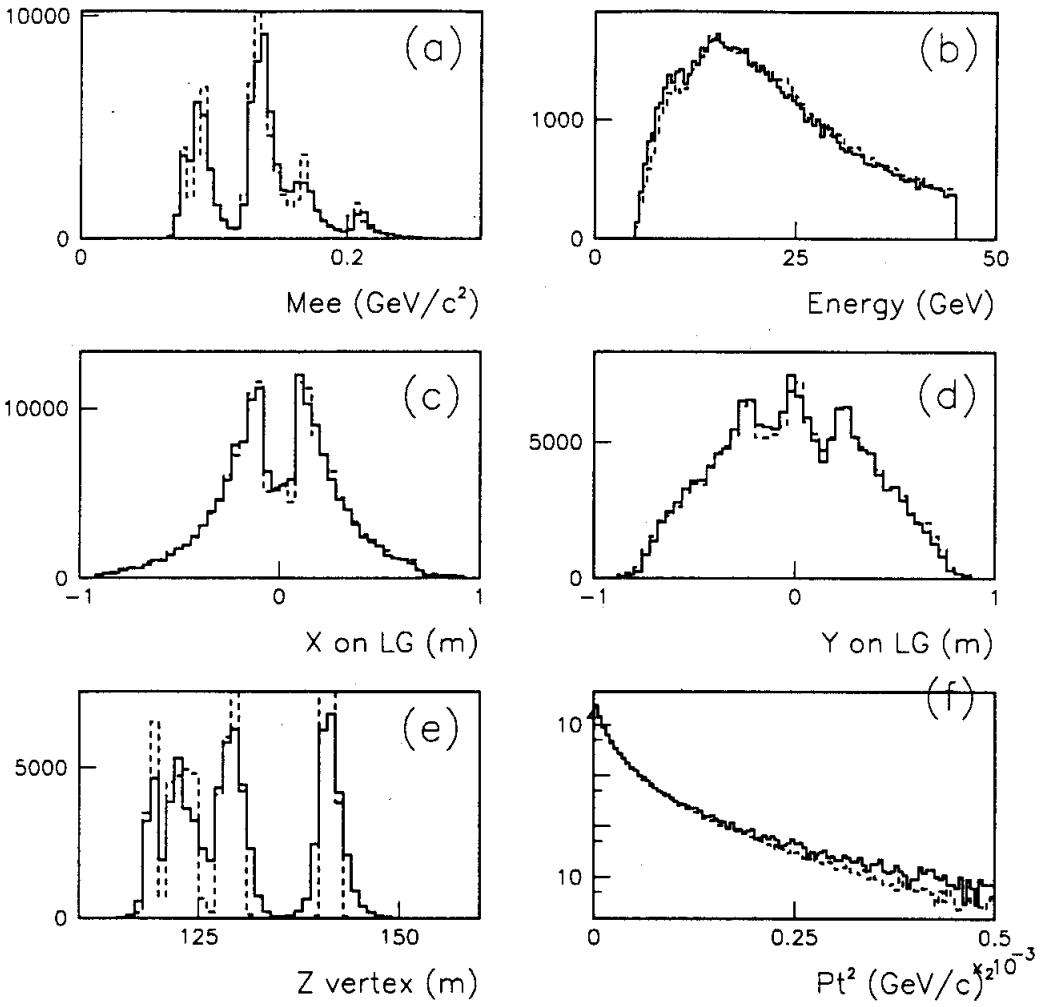

Figure 5.3: For the two electron events in the calibration data, (a) the total invariant mass distribution, (b) the total energy distribution, (c) the illumination at the calorimeter in the x direction, (d) the illumination at the calorimeter in the y direction, (e) the z vertex distribution, and (f) the p_t^2 distribution are shown for the data (solid line) and the Monte Carlo (dashed line). The Monte Carlo was normalized by the number of events.

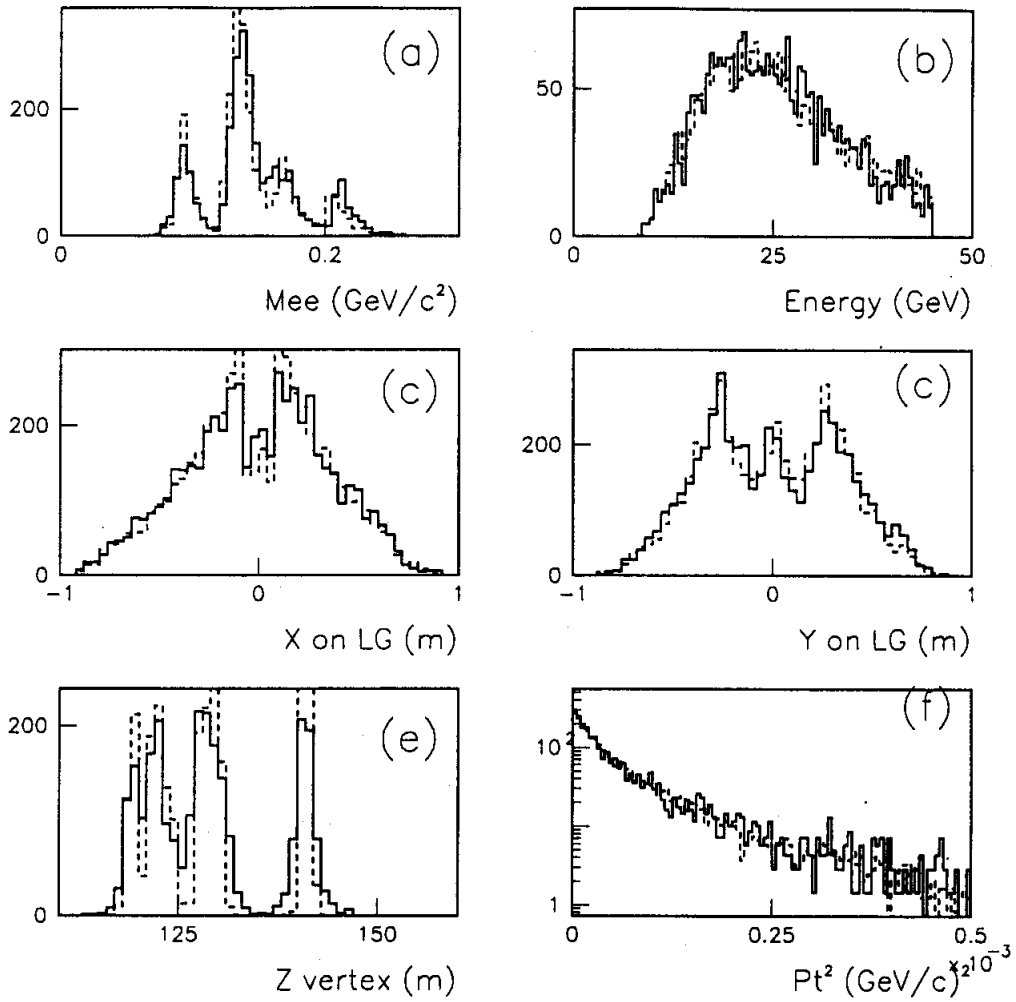

Figure 5.4: For the two electron with a photon events in the calibration data, (a) the total invariant mass distribution, (b) the total energy distribution, (c) the illumination at the calorimeter in the x direction, (d) the illumination at the calorimeter in the y direction, (e) the z vertex distribution, and (f) the p_t^2 distribution are shown for the data (solid line) and the Monte Carlo (dashed line). The Monte Carlo was normalized by the number of events.

Table 5.3: The numbers of the two cluster events and three cluster events in the electron calibration run, and the ratios between the data and Monte Carlo. The ratio from the MC expectation differed by 20% from the data.

	# 2 Cluster	# 3 Cluster	$\frac{\#\text{ 3 cluster}}{\#\text{ 2 Cluster}}$
DATA	79512	2652	0.0334
MC	279717	7513	0.0269
$\frac{\text{MC}}{\text{DATA}}$	3.52	2.83	0.805

5.2.3 Monte Carlo Statistics

Another important systematic error comes from the statistics of the Monte Carlo events. Each decay mode in Table 5.1 was generated with a weight (w_i) for each event. When each event has its own weight, the effective number of events is formulated as:

$$n_{eff} = \frac{T^2}{\delta^2} = (\sum w_i)^2 / \sum w_j^2,$$

where T is the number of accepted events and δ is the related error to T [51]. The statistical error of the generated events, $\delta/T = \sqrt{\sum w^2}/\sum w$, was taken as the systematic error of the Monte Carlo events. The statistical information for accepted events in the final analysis is summarized in Table 5.4.

Table 5.4: The statistical information for accepted events in the final analysis.

	$\sum w$	$\sum w^2$	$\sqrt{\sum w^2}/\sum w$
$A_{e^+e^-\gamma\to e^+e^-\gamma}$	8460.653	2308.996	0.00568
$A_{e^+e^-\gamma\gamma\to e^+e^-\gamma}$	4166.872	8252.723	0.0218
$A_{e^+e^-\gamma\to e^+e^-\gamma\gamma}$	2711.546	10411.03	0.0376
$A_{e^+e^-\gamma\gamma\to e^+e^-\gamma\gamma}$	32190.88	682257.7	0.0257

Each error is related to the branching ratio through the similar equations as Equation 5.8. Finally, the combined MC statistics error gave 3.4% systematic error to the $K_L \to e^+e^-\gamma\gamma$ branching ratio.

5.2.4 $K_L \to e^+e^-\gamma$ Form Factor

The uncertainty in the $K_L \to e^+e^-\gamma$ form factor contributed to the total systematic error. Some experiments observed a non-constant $K_L \to e^+e^-\gamma$ form factor

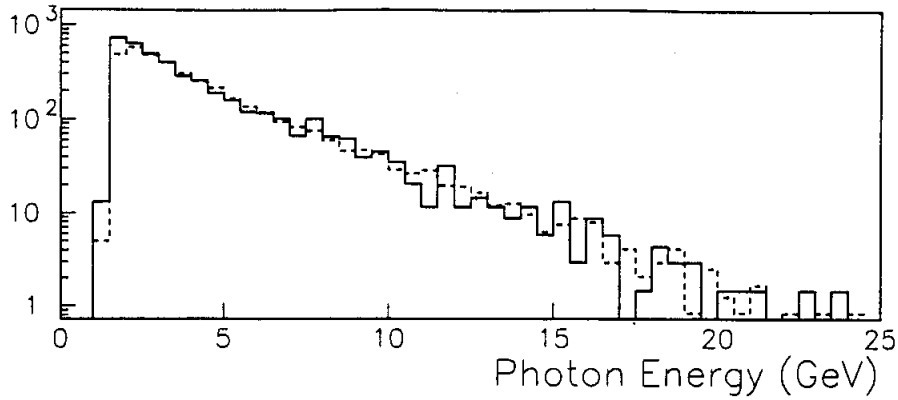

Figure 5.5: The cluster energy distributions of the bremsstrahlung photon for the data (solid line) and MC (dashed line) without the 2.5 GeV cluster energy requirement.

as described in Section 1.2. In this analysis, a constant form factor was used for the decays $K_L \to e^+e^-\gamma\gamma$ and $K_L \to e^+e^-\gamma$ in the Monte Carlo simulation. The change in the $K_L \to e^+e^-\gamma\gamma$ branching ratio by using the non-constant form factor was assigned as a systematic error.

Using the non-constant form factor with the parameter of $\alpha_{K^*} = -0.28$, the acceptances for decays $K_L \to e^+e^-\gamma$ and $K_L \to e^+e^-\gamma\gamma$ were recalculated. The result is shown in Table 5.5 with the deviations from the acceptances for the constant form factor.

Table 5.5: The acceptance for each decay mode with the non-constant form factor with the parameter of $\alpha_{K^*} = -0.28$. The percentage in the parentheses shows the deviation from the acceptances for the constant form factor.

Decay Mode	Acceptances (10^{-4})	
	$ee\gamma$	$ee\gamma\gamma$
$K_L \to ee\gamma$	10.00 (8.5%)	0.49 (10.4%)
$K_L \to ee\gamma\gamma$	14.7 (12.1%)	8.2 (7.9%)

The acceptances for decays with the non-constant form factor are larger than those with the constant form factor. This is because the non-constant form factor enhances the high e^+e^- invariant mass events in the decay $K_L \to e^+e^-\gamma$ and $K_L \to e^+e^-\gamma\gamma$, and our detector had larger acceptance at the high e^+e^- invariant

mass region. The branching ratio using the acceptances in Table 5.5 is $BR(K_L \to e^+e^-\gamma\gamma, E_\gamma^* \geq 5 \text{ MeV}) = 6.615 \times 10^{-7}$, which was 2.2% higher than the branching ratio using the constant form factor. The change in the branching ratio is smaller than the change in acceptances, since both the normalization decay mode and the signal decay mode have a common form factor.

5.2.5 Position Resolution for Photons

The uncertainty in the position resolution for photons caused the systematic error in the acceptances of the decays $K_L \to e^+e^-\gamma\gamma$ and the $K_L \to e^+e^-\gamma$ with external bremsstrahlung photon through the θ_{min} cut. In order to study the position resolution for photons, the events with an external bremsstrahlung photon in the special electron calibration run was used, since the position of the bremsstrahlung photon can be determined from the extrapolation of the parent electron track. The distribution of the bremsstrahlung photon around the extrapolated position is so small (typically 0.5 mm) compared with the typical position resolution of the calorimeter (4.6 mm) that we can study the position resolution for photons.

The distance between the bremsstrahlung photon and the extrapolated position of the electron upstream track in the x-direction and y-direction are shown in Figure 5.6 for the data and the Monte Carlo. The standard deviation in the x-direction for the data, 5.3 ± 0.2(stat.) mm, was far larger than the σ predicted by MC, 4.6 mm. Although the source of the discrepancy between the data and the Monte Carlo is not known, the positions of the photon in the Monte Carlo events were smeared to match the data. This smearing changed the acceptance of the $K_L \to e^+e^-\gamma$ decay in the $e^+e^-\gamma\gamma$ events by 5.5% and the acceptance of the $K_L \to e^+e^-\gamma\gamma$ decay by 1.0%, which resulted in 2.2% change in the $K_L \to e^+e^-\gamma\gamma$ branching ratio.

5.2.6 Fusion Cut

The difference in the fusion cut efficiency between the data and MC causes a systematic error. The fusion cut efficiency was studied by removing the fusion cut for the $e^+e^-\gamma$ final sample and for the "less restrictive" $e^+e^-\gamma\gamma$ sample where it was assumed that these samples were composed of purely electrons and photons. Each efficiency of the fusion cut for the electron and the photon between data and Monte Carlo in these samples is shown in Table 5.6.

Though the efficiencies were consistent between the data and MC within the statistical error, the difference of the central value was assigned as a systematic error. Since we measured the relative branching ratio of the decay $K_L \to e^+e^-\gamma\gamma$ to that of the decay $K_L \to e^+e^-\gamma$, the only difference of the fusion cut efficiencies appears for one photon. Therefore, we took the difference of the fusion cut efficiency for a photon, 1.5%, as this systematic error.

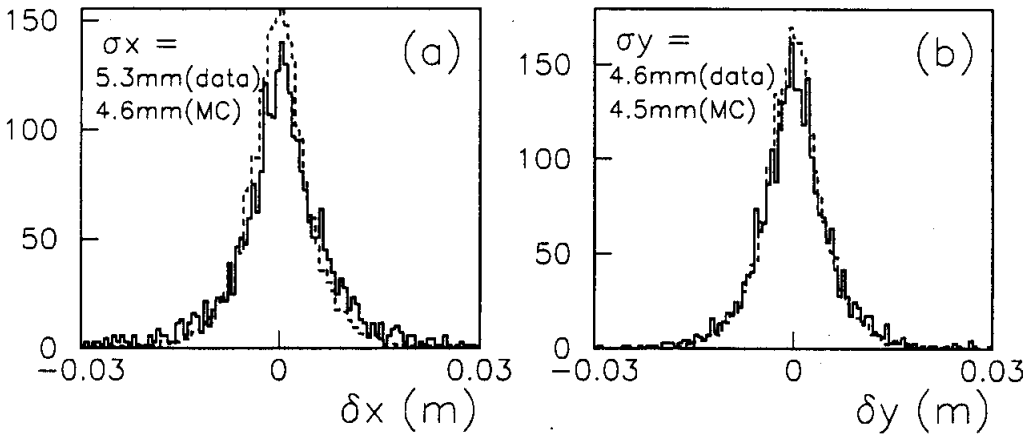

Figure 5.6: The distributions of the distance between the photon and the extrapolated position of the electron upstream track. The data (solid line) and Monte Carlo (dashed line) were compared in the x-direction (a) and the y-direction (b). The standard deviations were σ_x(data) = 5.3 mm, σ_x(MC) = 4.6 mm , σ_y(data) = 4.6 mm and σ_y(MC) = 4.5 mm .

Table 5.6: The efficiency (%) of the fusion cut for the electron and the photon for the data and the Monte Carlo.

	The Data	MC	Difference
The electron	$94 \pm 3\%$	92.5%	-1.6%
The photon	$87 \pm 3\%$	85.6%	-1.5%

5.2.7 Energy Measurement

Various distributions, such as mass, p_t^2, etc. have finite width due to the detector resolution, and we accept events which are in windows of finite width. Therefore, an uncertainty in the detector resolution gives an uncertainty in the acceptances, and thus to the branching ratio.

In the analysis, the overall calorimeter energy scale had a shift of about 1%, and the photon energy modeling for highly damaged blocks which located around beam holes was not accurate. In addition, there were uncorrected pedestal shifts, uncertainty in the calorimeter gain and a large coherent changes to the calibration constants in the most damaged blocks. The signal and the normalization Monte Carlo samples were modified in various ways to include the above effects, and then the change of the acceptances were studied. The change of the branching ratio due to the change of the acceptances was taken as an associated systematic error.

In order to estimate the above effects quantitatively, the energy resolution was smeared or shifted intentionally as followings in the reasonable extents on the Monte Carlo simulation:

1. In order to study the uncertainty in the energy scale, all cluster energies were shifted by 1%.

2. In order to study the uncertainty in the energy resolution, all cluster energies were smeared by 4%.

3. In order to study the uncertainty in energy resolution of each block, the energies of the blocks in the cluster were smeared by 2%.

4. In order to study the uncorrected pedestal shifts, all cluster energies were shifted by 20 MeV and smeared by 60 MeV.

5. In order to study the uncertainty in the energy scale of the damaged block around the beam holes, the energies of the pipe blocks which were the blocks around the beam hole were shifted by 1.5%.

6. In order to study the uncertainty in the energy resolution of the damaged blocks, the energies of the pipe blocks were smeared by 3.7% , and the energies of the blocks around the pipe blocks were smeared by 2.4%.

In the above description, the shift means that the energy (E) was changed from E to $E \times (1+h)$ where h is the factor of the shift, and the smear means that the energy was changed from E to $E \times (1+g)$ where g is the Gaussian distribution with the σ equal to the factor of the smear. Table 5.7 shows the change of the acceptances and the change in the branching ratio after these smears and shifts. In this study, the smearing of cluster energies (#2) gave the largest change in the acceptance, but the change in the branching ratio was as small as others because of the cancellation between signal and normalization modes. Finally, adding all individual components in quadrature, the systematic errors on the branching ratio was calculated to be 1.5%.

Table 5.7: The changes (%) in the acceptances and branching ratio after the smears and shifts of the energy. The detailed description of the smears and shifts is in the text, and the numbers correspond to the labels in the text.

	$\delta A_{ee\gamma \to ee\gamma}$	$\delta A_{ee\gamma \to ee\gamma\gamma}$	$\delta A_{ee\gamma\gamma \to ee\gamma}$	$\delta A_{ee\gamma\gamma \to ee\gamma\gamma}$	$\delta BR(K_L \to e^+e^-\gamma\gamma)$
1	0.2	0.04	-0.5	0.7	-0.8
2	-7.4	-10.3	-8.1	-7.5	0.2
3	-1.5	-1.7	-1.9	-1.7	0.0
4	-0.2	-1.4	-0.4	-0.2	0.1
5	-0.2	0.7	-0.1	0.7	-1.1
6	-1.7	-1.6	-1.4	-1.1	-0.7

5.2.8 Momentum Measurement

In the same fashion as Section 5.2.7, the uncertainty in the momentum measurement was taken as a systematic error on the branching ratio.

The observed $K_L \to \pi^+\pi^-$ decay in this experiment had a mass of 497.86 ± 0.04 MeV/c^2 and a width of 0.614 ± 0.010% where Monte Carlo predicted the mass of 497.70 ± 0.03 MeV/c^2 and the width of 0.553 ± 0.006%. In order to check the effect of these uncertainties in the momentum measurements to the branching ratio, the momentum resolution was smeared or shifted intentionally as followings in the reasonable extents on the Monte Carlo simulation:

1. In order to study the uncertainty in the momentum scale, the track momenta were shifted by 0.05%.

2. In order to study the uncertainty in the momentum resolution, the track momenta were smeared by 0.42%.

3. In order to study the uncertainty in the momentum resolution due to the non-Gaussian tail, the track momenta were catastrophically smeared by 14% with the probability of 0.7%.

Table 5.8 shows the change in the acceptances and the change in the branching ratio after these smears and shifts. Adding all individual components in quadrature, the systematic errors on the branching ratio was calculated to be 1.0%.

Table 5.8: The changes (%) in the acceptances and branching ratio after the smears and shifts of the momentum. The detailed description of the smears and shifts is in the text, and the numbers correspond to the labels in the text.

	$\delta A_{ee\gamma\to ee\gamma}$	$\delta A_{ee\gamma\to ee\gamma\gamma}$	$\delta A_{ee\gamma\gamma\to ee\gamma}$	$\delta A_{ee\gamma\gamma\to ee\gamma\gamma}$	$\delta BR(K_L\to e^+e^-\gamma\gamma)$
1	-1.2	-1.5	-1.0	-0.9	-0.2
2	-1.3	-1.8	-1.5	-0.7	-0.7
3	-1.5	-1.4	-1.3	-0.8	-0.8

5.2.9 Backgrounds Subtraction

The error on the background estimation corresponds to the error on the number of signal events. Therefore the effect of this error to the uncertainty on the branching ratio was taken as a systematic error. In Section 4.3, there are 3.5 ± 0.4 background events in the $e^+e^-\gamma\gamma$ events, and there are 2.7 ± 1.0 background events in the $e^+e^-\gamma$ events. These errors caused the 0.7% systematic error on the branching ratio.

5.3 Observation of the Phase Space Variables

In order to see the distributions of phase space variables with higher statistics, θ_{min} cut was loosened for the $e^+e^-\gamma\gamma$ events. This relaxation also increased the number of the $K_L \to e^+e^-\gamma$ decay in the $e^+e^-\gamma\gamma$ events.

Figure 4.20 shows θ_{min} distribution with lower θ_{min} cut, $0.06 \leq \theta_{min}$. In order to get higher statistics, θ_{min} cut was removed. This relaxation increased the number of the $e^+e^-\gamma\gamma$ events to 203 events from 69 events. With the exactly same analysis described in Section 4.3 and 5.1, the number of the $K_L \to e^+e^-\gamma\gamma$ events was measured to be 151.6 ± 17.4 events. The expected number of background events are 47.2 ± 9.9 from $K_L \to e^+e^-\gamma$, 2.6 ± 0.4 from $K_L \to \pi^0\pi^0_D$, 1.1 ± 0.3 from $K_L \to \pi^\pm e^\mp \nu(2\gamma)$, and 0.5 ± 0.2 from $K_L \to \pi^0\pi^0\pi^0_D$. The definitions of these background are given in Section 4.2.

By using 203 $K_L \to e^+e^-\gamma\gamma$ events with an estimated backgrounds of 51 ± 10 events, we observed some phase space distributions for the radiative $K_L \to e^+e^-\gamma\gamma$ decay. Figure 5.7 shows M_{ee} and $M_{\gamma\gamma}$ distributions. This is the first time that these distributions are observed.

In addition, Figure 5.8 shows the maximum and the minimum photon energy distributions, and the energy asymmetry ($\frac{|E_1-E_2|}{E_1+E_2}$) in the center of mass frame of

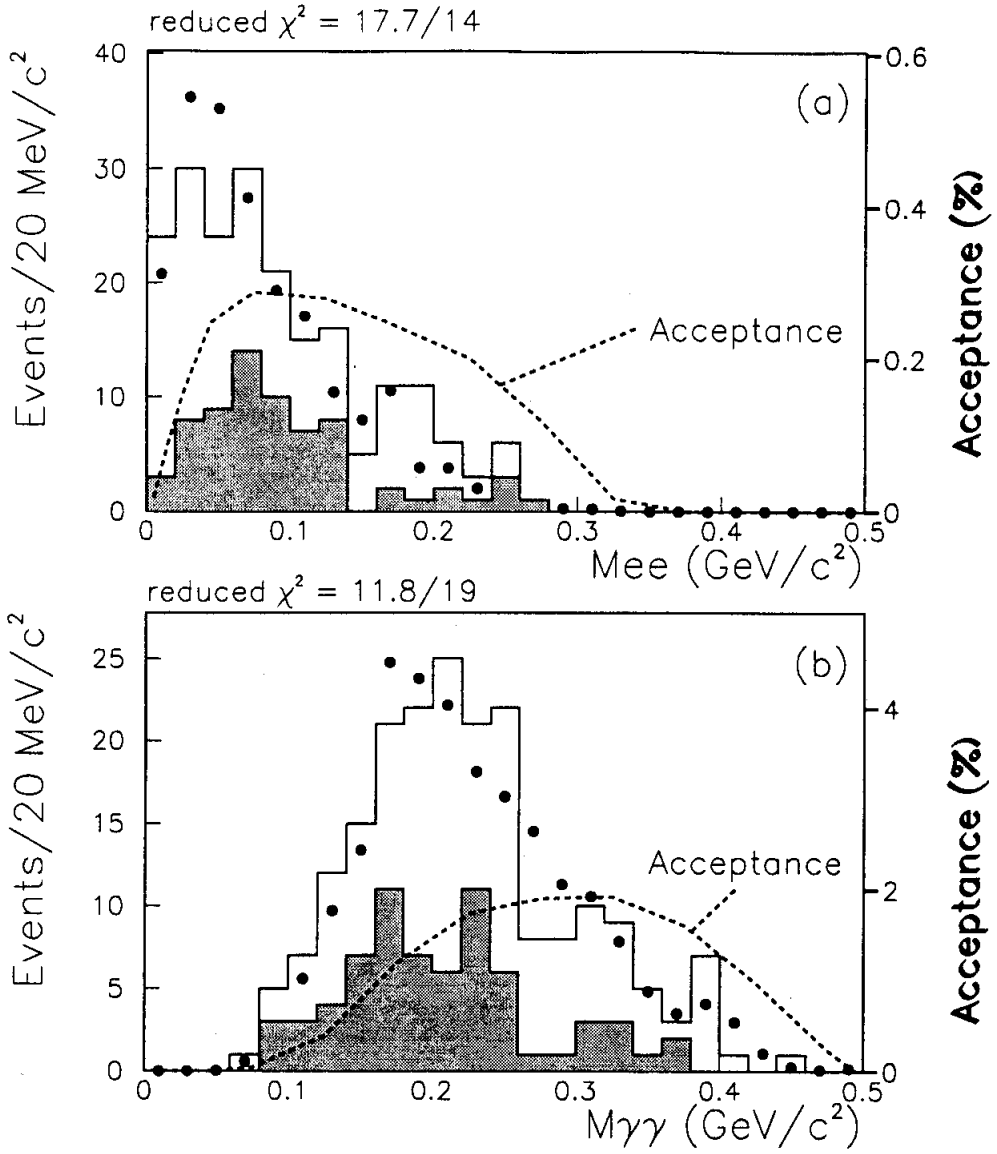

Figure 5.7: M_{ee} (a) and $M_{\gamma\gamma}$ (b) distributions for the decay $K_L \to e^+e^-\gamma\gamma$. For the less restrictive analysis, the Monte Carlo is shown by the dots, and the data is shown by the solid line. The Monte Carlo events composed of 152 $K_L \to e^+e^-\gamma\gamma$ signal events and 51 background events including the decay $K_L \to e^+e^-\gamma$. The data selected by the normal analysis is also shown by the shaded region. The acceptances in the less restrictive analysis are shown as a function of M_{ee} and $M_{\gamma\gamma}$.

the kaon. The energetic photons shown in Figure 5.8 (a) mostly come from the K_L decay vertex directly, while the low energy photons in Figure 5.8 (b) come from internal bremsstrahlung. Therefore, the energies of photons are very asymmetric. These distributions support that the main process in the decay $K_L \to e^+e^-\gamma\gamma$ is the radiative Dalitz $K_L \to e^+e^-\gamma\gamma$ decay.

By moving the analysis backward, we check θ_{min} distribution in Figure 5.9 without the criteria on θ_{min}. In addition, we also check minΣ cos distribution in Figure 5.10 without the criteria on both θ_{min} and minΣ cos. Since no special cuts on the phase space were imposed on these events, this will be a sample used for a direct emission $K_L \to e^+e^-\gamma\gamma$ process and for the decay $K_L \to He^+e^-, H \to \gamma\gamma$. In these distributions, the Monte Carlo events well reproduced the data by including all background MC events which are estimated in Section 4.3. The difference between the data and MC prediction would indicate the existence for the direct emission $K_L \to e^+e^-\gamma\gamma$ process or for the decay $K_L \to He^+e^-, H \to \gamma\gamma$. These processes are studied in the next chapter.

Form Factor

In Figure 5.7 (a), M_{ee} distribution is consistent with MC prediction which does not include any non-constant form factor. By fitting M_{ee} distributions with a non-constant form factor shown in Equation 1.1, we measured the parameter in the form factor to be $\alpha_{K^*} = -3.0^{+5.0}_{-9.0}$. This result is consistent with the previous measurements [25, 26, 52] within the large error. Since this measurement had a large error due to the low statistics of events with high M_{ee}, a more precise measurement requires the $K_L \to e^+e^-\gamma\gamma$ sample with higher statistics.

In spite of the large uncertainty of the measured $K_L \to e^+e^-\gamma\gamma$ form factor, the measured $K_L \to e^+e^-\gamma\gamma$ branching ratio helps to determine the $K_L \to e^+e^-\gamma$ form factor which has an uncertainty due to radiative correction. The effect of the radiative correction to the $K_L \to e^+e^-\gamma$ form factor is discussed in Appendix A.

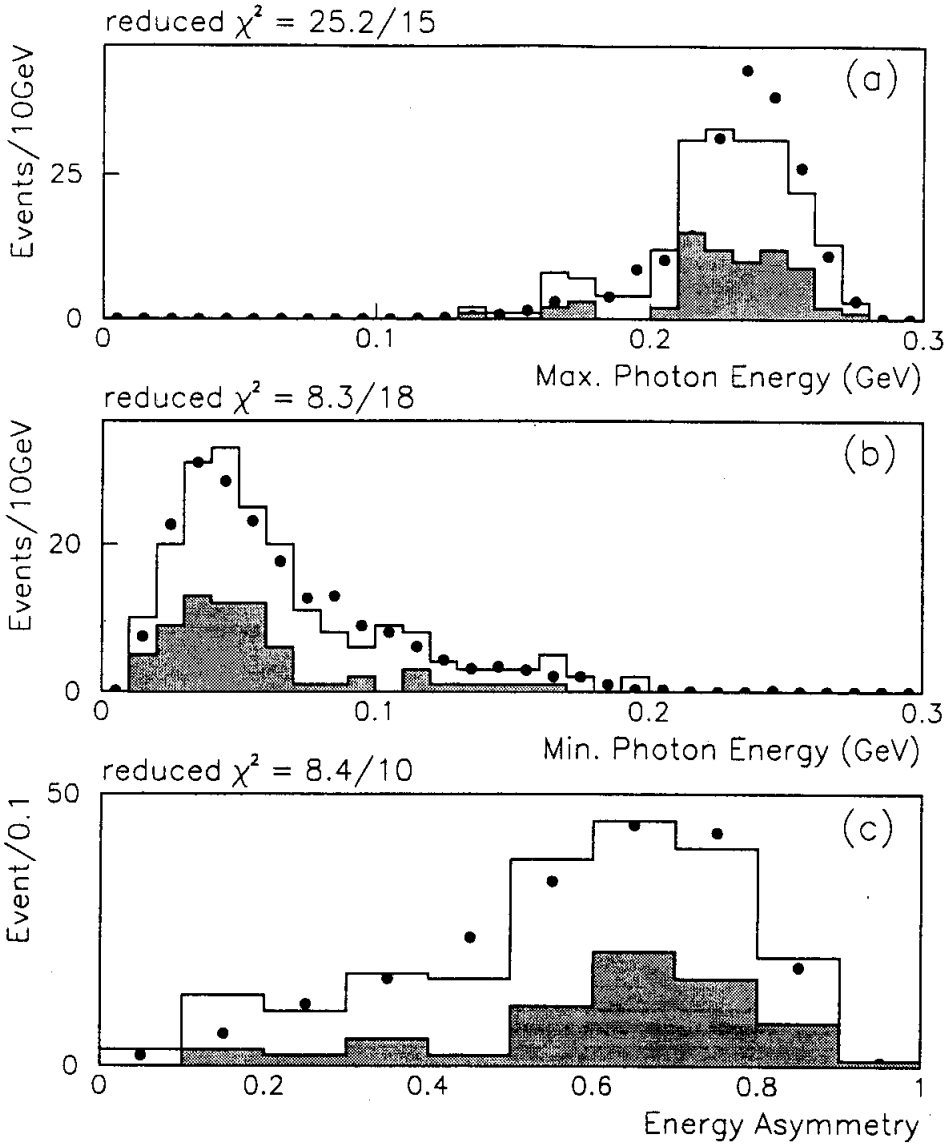

Figure 5.8: The distributions of the maximum (a) and the minimum (b) photon energy, and the energy asymmetry, $\frac{|E_1-E_2|}{E_1+E_2}$, (c) in the center of mass frame of the $K_L \to e^+e^-\gamma\gamma$ events. The Monte Carlo events is shown by the dots for the less restrictive analysis, and the data is shown by the solid line for the less restrictive analysis. The shaded region shows the events selected by the normal analysis for the branching ratio measurement.

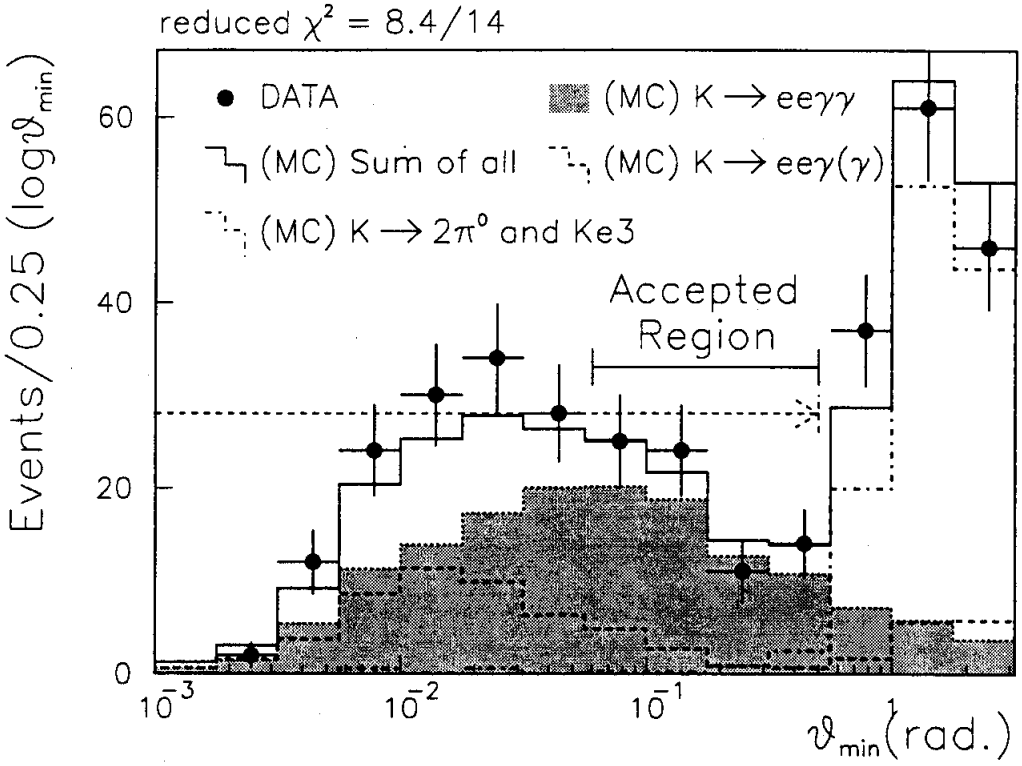

Figure 5.9: The distribution of the minimum angle (θ_{min}) between each electron and photon combination in the center of mass frame of the kaon. The normalization is described in the text. The accepted region in the normal analysis is shown by the solid line, and the region in the less restrictive analysis is shown by the dashed arrow.

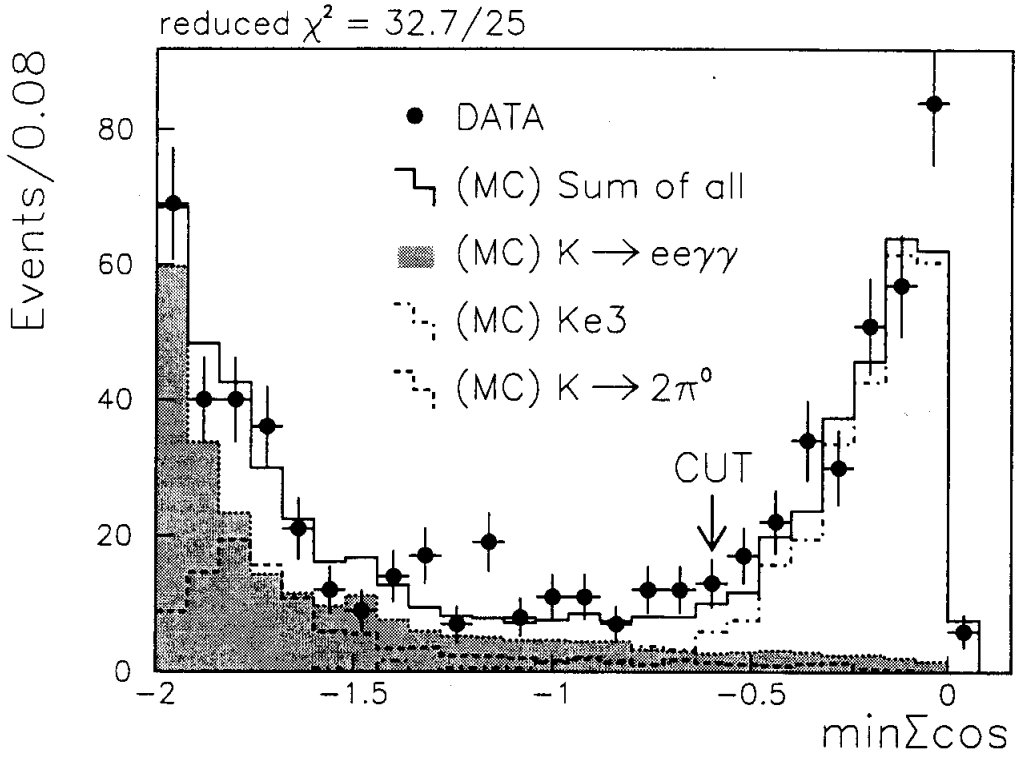

Figure 5.10: The minΣcos distribution of the $e^+e^-\gamma\gamma$ events for the data, and Monte Carlo signal and the background events. The Monte Carlo normalization is described in Section 4.3. The peak at -2 is the signal from the decay $K_L \to e^+e^-\gamma\gamma$, where the Monte Carlo includes the sum of the $K_L \to e^+e^-\gamma\gamma$ and $K_L \to e^+e^-\gamma$ events in the $e^+e^-\gamma\gamma$ events in the proportions derived from the normal analysis.

Chapter 6

Search for Non-Radiative Dalitz $K_L \to e^+e^-\gamma\gamma$ Decays, and Impact of $K_L \to e^+e^-\gamma\gamma$ Decay to $K_L \to \pi^0 e^+e^-$

In Chapter 5, we measured the branching ratio of the radiative K_L Dalitz decay, $K_L \to e^+e^-\gamma\gamma$, with the optimized cuts for this decay. In addition, we confirmed that some phase space distributions of the $e^+e^-\gamma\gamma$ events are also consistent with those of the radiative K_L Dalitz decay. In Chapter 5, we concluded that the $K_L \to e^+e^-\gamma\gamma$ decay is well explained with the model of the radiative Dalitz decay.

We expect that there are two processes in the decay $K_L \to e^+e^-\gamma\gamma$: one comes from the radiative Dalitz K_L decay and the other comes from the direct emission process, $K_L \to \gamma\gamma\gamma^* \to e^+e^-\gamma\gamma$. Therefore, when we remove the optimized cuts for the radiative K_L Dalitz decay from the $e^+e^-\gamma\gamma$ events, the direct emission process in the decay $K_L \to e^+e^-\gamma\gamma$ could show up as an excess over the prediction from the radiative Dalitz $K_L \to e^+e^-\gamma\gamma$ decay and known K_L decay backgrounds. If the excess is not caused by the direct emission process, it would have come from unknown physics outside of the standard model.

In Section 6.1, we search for the direct emission process in the decay $K_L \to e^+e^-\gamma\gamma$. In Section 6.2, we also search for the decay outside of the standard model where a Higgs-like particle would be related with the decay $K_L \to e^+e^-\gamma\gamma$, such as $K_L \to He^+e^-, H \to \gamma\gamma$. In Section 6.3, we study the $K_L \to e^+e^-\gamma\gamma$ background level in search for $K_L \to \pi^0e^+e^-$. The decay $K_L \to \pi^0e^+e^-$ is one of the attractive decays to study the CP violation. Since the decay $K_L \to e^+e^-\gamma\gamma$ is the most serious background for the decay $K_L \to \pi^0e^+e^-$, the decay $K_L \to e^+e^-\gamma\gamma$ also strongly arrests the attention of the particle physicists who study the CP violation. Therefore, we study the $K_L \to e^+e^-\gamma\gamma$ background level for $K_L \to \pi^0e^+e^-$ based on our measurement of the $K_L \to e^+e^-\gamma\gamma$ branching ratio.

6.1 Search for Direct Emission Process

6.1.1 Result

The direct emission $K_L \to e^+e^-\gamma\gamma$ decay is an interesting process since this decay is a probe to see the higher order effect in ChPT. In ChPT, the predicted branching ratio is around 10^{-10} due to some anomalous vertexes as shown in Figure 1.7. Therefore, the measured branching ratio of this process can set the constraint on the coupling strength of the above vertexes. In case of naive expectation, the direct emission process would be seen around 10^{-8} on the branching ratio. The direct emission $K_L \to e^+e^-\gamma\gamma$ decay has never been seen as well as the parent $K_L \to \gamma\gamma\gamma$ decay. Therefore, we had a possibility to see this process.

In order to search for the direct emission process in the decay $K_L \to e^+e^-\gamma\gamma$, we removed θ_{min} and minΣcos cuts which were optimized for the radiative K_L Dalitz in Section 4.2. Without these cuts, we observed 655 $e^+e^-\gamma\gamma$ events as shown in Table 4.3. We searched for the direct emission process as the deviation between data and the expectation from the known K_L decays. Monte Carlo simulation expected 639 ± 42 events from the known K_L decays in the above 655 $e^+e^-\gamma\gamma$ events. The contents of the MC expectations are 191 ± 38 events from the radiative Dalitz $K_L \to e^+e^-\gamma\gamma$, 62 ± 12 events from $K_L \to e^+e^-\gamma$, 263 ± 12 events from $K_L \to \pi^\pm e^\mp \nu(2\gamma)$, 119 ± 4 events from $K_L \to \pi^0\pi^0_D$ and 4 ± 2 events from other decays. The $K_L \to \pi^\pm e^\mp \nu(2\gamma)$ background was defined as $K_L \to \pi^\pm e^\mp \nu$ decay with two extra photons where the pion was misidentified as a electron, and the $K_L \to \pi^0\pi^0_D$ background was defined as $K_L \to 2\pi^0$ decay with a $\pi^0 \to e^+e^-\gamma$ decay where one photon was missed. The $K_L \to e^+e^-\gamma\gamma$ branching ratio measured with tight cuts, was used for the radiative Dalitz K_L decays.

The Monte Carlo expectation was consistent with the number of the $e^+e^-\gamma\gamma$ events without the direct emission $K_L \to e^+e^-\gamma\gamma$ decay. Therefore, we observed no signature for the direct emission $K_L \to e^+e^-\gamma\gamma$ process. We set the following limit on the number of the direct emission $K_L \to e^+e^-\gamma\gamma$ process (N_{direct}) as:

$$\begin{aligned} N_{direct} &< (N_{observed} - N_{expected}) + 1.96\sigma \ (95\% C.L.) \\ &= (655 - 639) + 1.96 \times \sqrt{655 + 42^2} \ (95\% C.L.) \\ &= 112 \ (95\% C.L.), \end{aligned}$$

where $N_{observed}$ and $N_{expected}$ are the number of observed and expected $e^+e^-\gamma\gamma$ events, respectively. The σ is the error of $(N_{observed} - N_{expected})$ where both statistics and systematic errors are combined. The acceptance of the direct emission $K_L \to e^+e^-\gamma\gamma$ decay was calculated to be 2.92% by assuming the flat four-body phase space. The total number of kaon decays in our experiment was measured to be $(2.89 \pm 0.19) \times 10^{10}$ by the decay $K_L \to e^+e^-\gamma$ as shown in Section 5.1. Therefore, the upper limit on the branching ratio of the direct emission $K_L \to e^+e^-\gamma\gamma$ decay

was set to be:

$$\begin{aligned} BR(K_L \to e^+e^-\gamma\gamma[direct]) &= \frac{N_{direct}}{A(K_L \to e^+e^-\gamma\gamma[direct]) \times \#K_L}\ (95\%C.L.) \\ &< \frac{112}{0.0292 \times 2.89 \times 10^{10}}\ (95\%C.L.) \\ &= 1.3 \times 10^{-7}\ (95\%C.L.), \end{aligned}$$

where the error on the kaon flux can be ignored since it is much smaller than the error on the N_{direct}.

In order to get a better sensitivity to this decay, phase space cuts were applied to the events described above based on the following general assumptions (see Section 1.2.2).

- There is no pole for $E_{\gamma^*}(M_{ee}) = 0$ in the direct emission $K_L \to e^+e^-\gamma\gamma$ decay.
- The energies of two photons are less asymmetric than the radiative Dalitz $K_L \to e^+e^-\gamma\gamma$ decay.

Based on these assumptions, the invariant mass of two electrons of the events was required to be greater than 135 MeV/c^2 (M_{π^0}) in order to suppress the $K_L \to \pi^0\pi^0_D$ backgrounds. In addition, the energy asymmetry of two photons was required to be less than 0.5 in order to suppress the radiative Dalitz $K_L \to e^+e^-\gamma\gamma$ decay. The minΣcos cut was also imposed on the events in order to suppress the $K_L \to \pi^\pm e^\mp \nu(2\gamma)$ background as described in Section 4.2. After these cuts, we observed 24 $e^+e^-\gamma\gamma$ events where MC predicted 25.5 ± 3.2 events, whose contents are 13.5 ± 2.7 events from $K_L \to \pi^\pm e^\mp \nu(2\gamma)$, 9.0 ± 1.8 events from the radiative Dalitz $K_L \to e^+e^-\gamma\gamma$, and the rest of events from other decays. We did not observe any deviations. The acceptance of the direct emission $K_L \to e^+e^-\gamma\gamma$ decay was 0.88% for this event selection. Therefore, the upper limit on the branching ratio of the direct emission $K_L \to e^+e^-\gamma\gamma$ decay was set to be:

$$\begin{aligned} BR(K_L \to e^+e^-\gamma\gamma[direct]) &= \frac{N_{direct}}{A(K_L \to e^+e^-\gamma\gamma[direct]) \times \#K_L}\ (95\%C.L.) \\ &< \frac{(24 - 25.5) + 1.96 \times \sqrt{24 + 3.2^2}}{0.0088 \times 2.89 \times 10^{10}}\ (95\%C.L.) \\ &< \frac{0 + 1.96 \times 5.9}{0.0088 \times 2.89 \times 10^{10}}\ (95\%C.L.) \\ &= 4.5 \times 10^{-8}\ (95\%C.L.). \end{aligned}$$

This upper limit is close to the naive expectation of $\sim 3.1 \times 10^{-8}$ for the direct emission $K_L \to e^+e^-\gamma\gamma$ process, but we did not see a signature for the direct emission process.

In addition, these results also indirectly set a limit on the branching ratio of the decay $K_L \to \gamma\gamma\gamma$. With an assumption of $BR(K_L \to \gamma^*\gamma\gamma \to e^+e^-\gamma\gamma) = \alpha_{QED} \cdot$

$BR(K_L \to \gamma\gamma\gamma)$, the upper limit on the branching ratio of the decay $K_L \to \gamma\gamma\gamma$ is:

$$\begin{aligned} BR(K_L \to \gamma\gamma\gamma) &= \frac{1}{\alpha_{QED}} BR(K_L \to e^+e^-\gamma\gamma[direct]) \\ &< 137 \times (1.3 \times 10^{-7})\ (95\%C.L.) \\ &= 1.7 \times 10^{-5}\ (95\%C.L.). \end{aligned}$$

The events without any phase space cuts were used for this limit because M_{ee} is expected to be peaked near 0. This is also the first limit on the branching ratio of the decay $K_L \to \gamma\gamma\gamma$.

6.1.2 Discussion

The absence of the direct emission process is still consistent with both the naive expectation ($\sim 3.1 \times 10^{-8}$) and ChPT predictions ($\sim 10^{-10}$). Our negative result at the sensitivity of 10^{-8} on the branching ratio would indicate the existence of some suppression mechanisms to $K_L \to \gamma\gamma\gamma^*$, which otherwise is expected at $\sim 3.1 \times 10^{-8}$.

In ChPT, a suppression mechanisms is a small coupling on the anomalous vertexes as shown in Figure 1.7, which are $K_L - \gamma^* S^{*\,++}$, $K_L - \gamma^* P^{*\,--}$, and $K_L - \gamma V^{*\,++}$ vertexes where S^{++} is a scalar (0^{++}) state, P^{--} is a CP-even Psuedoscalar (0^{--}, e.g. K_S) state, and V^{++} is a C-even Axial-vector state. The first vertex, $K_L - \gamma^* S^{*\,++}$ would be not small, but the branching fraction of $S \to \gamma\gamma$ is small where S state would be $f_0(980)$ or $a_0(980)$. The second vertex, $K_L - \gamma^* P^{*\,--}$, would be small because of the small charge radius of K_L as described in Section 1.2.2. In addition, the branching fraction of $P^* \to \gamma\gamma$ is also small since P^* is actually a K_S ($BR(K_S \to \gamma\gamma) = (2.4 \pm 1.2) \times 10^{-6}$). The third vertex, $K_L - \gamma V^{*\,++}$, would not be small since we have some evidence of large contribution from conventional vector meson exchange diagrams by ρ, ω and ϕ. Nevertheless, we do not have many evidences for the influence of higher energy vector resonances, such as $a_1(1260)$ or $f_1(1285)$, in the low energy processes. The small contribution from higher energy vector resonances would make the third vertex small empirically. The small branching ratio of the $K_L \to e^+e^-\gamma\gamma$ direct emission process supports the above explanations, but the quantitative limits to the above vertexes require more theoretical efforts.

If the branching ratio of the $K_L \to e^+e^-\gamma\gamma$ direct emission process is larger than ChPT prediction, it would indicate the effect of higher energy vector resonances or the effect of unknown resonances. In addition it would indicate the existence of unknown particles, such as a Higgs-like particle or an axion which can contribute to the first and second vertexes in Figure 1.7, respectively. In the future, if we measure the branching ratio at ChPT prediction level, it would be meaningful since it is the first verification of the order p^8 contribution in ChPT where p is the momentum of the decay product, or the first verification of ChPT at the very small branching ratio ($\sim 10^{-10}$). Therefore, further experimental challenge is encouraged.

6.2 Search for Higgs-like Particles from the Decay $K_L \to He^+e^-, H \to \gamma\gamma$

6.2.1 Result

In addition to the $K_L \to e^+e^-\gamma\gamma$ decay inside of the standard model, we looked for the decay outside of the standard model, or new physics. In the $e^+e^-\gamma\gamma$ events, we looked for the decay $K_L \to He^+e^-, H \to \gamma\gamma$ where H denotes a Higgs-like particle with spin 0. The Higgs-like particle is assumed to couple to photons more strongly than electrons and muons with the smaller mass than that of the kaon. Therefore, this particle was not the standard Higgs particle which couples to electrons and muons as well as to photons in the mass around the kaon mass. We looked for the non-standard Higgs-like particle. A motivation of such a Higgs-like particle is due to the inconsistency on the $K_L \to \pi^0\gamma\gamma$ branching ratio between experiment and theory, which would indicate the existence of the particle as described in Section 1.2.3. The decay $K_L \to He^+e^-, H \to \gamma\gamma$ is sensitive to such a particle as well as the decay $K_L \to \pi^0\gamma\gamma$. In order to find the decay, we looked for a peak in $M_{\gamma\gamma}$ distribution.

In order to search for the Higgs-like particle in the $e^+e^-\gamma\gamma$ events, we removed θ_{min} and minΣcos cuts which were optimized to the radiative K_L Dalitz in Section 4.2. Without these phase space cuts, we observed 655 $e^+e^-\gamma\gamma$ events as shown in Table 4.3. Since photons from the decay $H \to \gamma\gamma$ are symmetrical, the energy asymmetry of photons in the center of mass frame of the kaon was required to be less than 0.5, which suppressed the radiative Dalitz $K_L \to e^+e^-\gamma\gamma$ decay. After this cut, we observed 399 $e^+e^-\gamma\gamma$ events. Figure 6.1 shows $M_{\gamma\gamma}$ distribution for the $e^+e^-\gamma\gamma$ events with the Monte Carlo prediction from the known K_L decays which are normalized in Section 4.3. The Monte Carlo predicts that low $M_{\gamma\gamma}$ events around $M_{\gamma\gamma} < 120\text{MeV}/c^2$ are dominated by the decay $K_L \to \pi^\pm e^\mp \nu(2\gamma)$, while the high $M_{\gamma\gamma}$ events around $M_{\gamma\gamma} > 120\text{MeV}/c^2$ are dominated by the decays $K_L \to e^+e^-\gamma\gamma$ and $K_L \to \pi^0\pi^0_D$.

We did not find any signature for the decay $K_L \to He^+e^-, H \to \gamma\gamma$ in Figure 6.1. Therefore, we set an upper limit on the branching ratio of the decay $K_L \to He^+e^-, H \to \gamma\gamma$.

In order to set the upper limit, we should know the acceptance for the decay $K_L \to He^+e^-, H \to \gamma\gamma$ which depends on both the mass and the life time of the Higgs-like particle. In case of the zero life time ($c\tau$), the acceptance as a function of the mass is shown in Figure 6.2 where the window for $M_{\gamma\gamma}$ was selected to be within 3σ of $M_{\gamma\gamma}$ resolution. The typical resolutions of $M_{\gamma\gamma}$ were σ = 5.7, 9.6 and 12.1 (MeV/c^2) for M_{Higgs} = 100, 200 and 300 (MeV/c^2), respectively. For the Higgs-like particle with the finite life time, Figure 6.3 shows the relative acceptance to that of prompt decay.

As an example, we will describe the Higgs-like particle search with the mass of 200 MeV/c^2 and the life time ($c\tau$) of less than 10^{-2} m. The mass window for

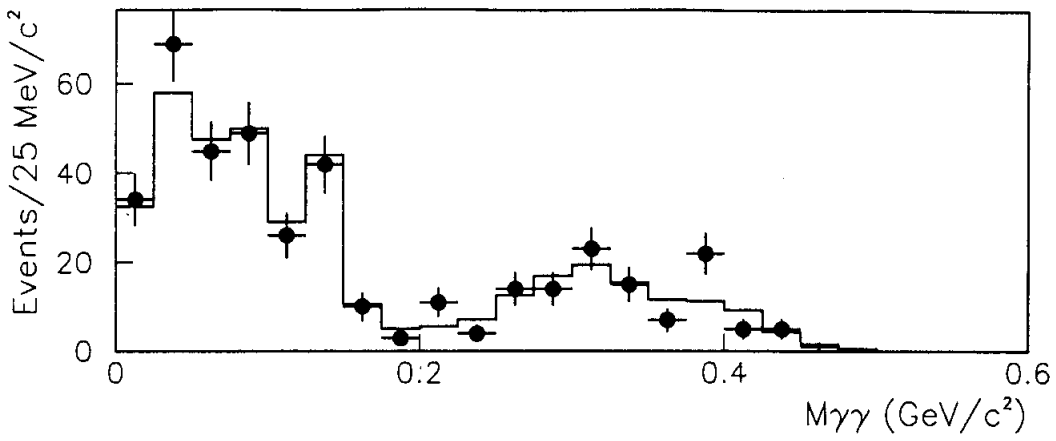

Figure 6.1: $M_{\gamma\gamma}$ distribution for the $e^+e^-\gamma\gamma$ events for Higgs-like particle search after the photon energy asymmetry cut imposed. The dots show the data and the solid line shows the Monte Carlo prediction from the known K_L decays.

the particle was set to be within $200 \pm 3 \times 9.6$ MeV/c^2 on $M_{\gamma\gamma}$ distribution. In this window, we observed 16 $e^+e^-\gamma\gamma$ events where MC predicted 13.8 ± 2.8 events from the known K_L decays. The acceptance for the decay $K_L \to He^+e^-, H \to \gamma\gamma$ is calculated to be 3.4% assuming the flat three-body phase space for the decay $K_L \to He^+e^-$. Therefore, the upper limit on the branching ratio for this decay is

$$\begin{aligned} BR(K_L \to He^+e^-, H \to \gamma\gamma) &= \frac{N_{Higgs}}{A(K_L \to He^+e^-, H \to \gamma\gamma) \times \#K_L} \\ &< \frac{(16 - 13.8) + 1.96 \times \sqrt{16 + 2.8^2}}{0.034 \times 2.89 \times 10^{10}} \ (95\% C.L.) \\ &= 1.2 \times 10^{-8} \ (95\% C.L.), \end{aligned}$$

where N_{Higgs} is a deviation of the numbers between the observed events and the MC prediction.

With this method, we can set the limit on the branching ratio for the range of the Higgs-like particle mass, $10 < M_{Higgs}(\mathrm{MeV/c^2}) < 450$ with the life time of $c\tau < 10^{-2}$ m. The result is shown in Figure 6.4. For the Higgs-like particle with a longer life time, the sensitivity in Figure 6.4 should be divided by the relative acceptance shown in Figure 6.3.

In order to get the better sensitivity for this search at lower mass region, we applied additional cuts; $M_{ee} > 135\mathrm{MeV/c^2}$ to suppress $K_L \to \pi^0\pi^0_D$ background and $-2.0 < \min\Sigma\cos < -0.6$ to suppress $K_L \to \pi^\pm e^\mp \nu(2\gamma)$ backgrounds. Figure 6.5

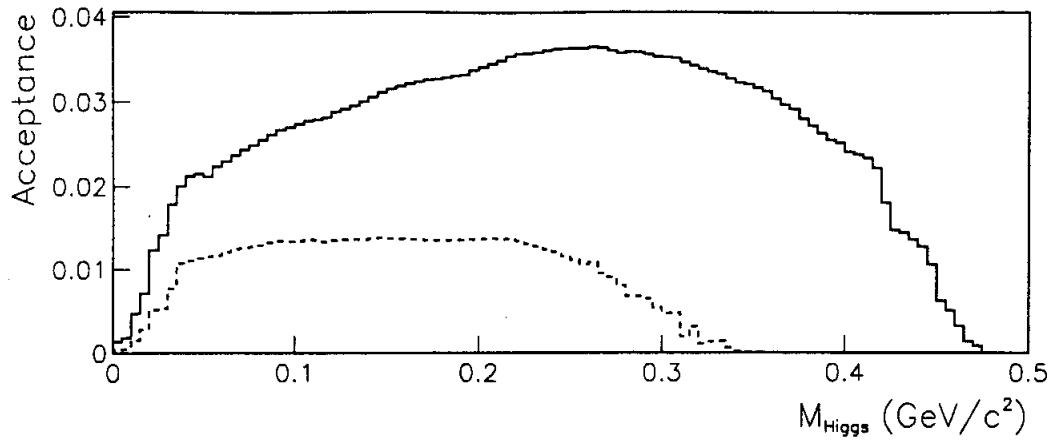

Figure 6.2: The acceptance for the decay $K_L \to He^+e^-, H \to \gamma\gamma$ (prompt decay). The mass window for the Higgs-like particle is set to be within 3σ of $M_{\gamma\gamma}$ resolution. The solid line shows the acceptance after the photon energy asymmetry cut imposed. The dashed line shows the acceptance with additional requirements of $M_{ee} > 135$ MeV/c^2 and of $\min\Sigma\cos < -0.6$.

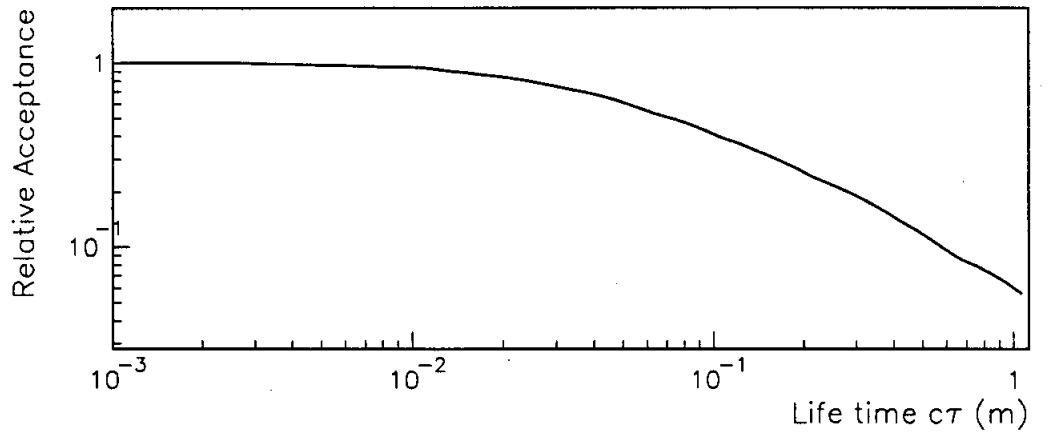

Figure 6.3: The relative acceptance for the decay $K_L \to He^+e^-, H \to \gamma\gamma$ with a finite life time ($c\tau$) to that of prompt decay.

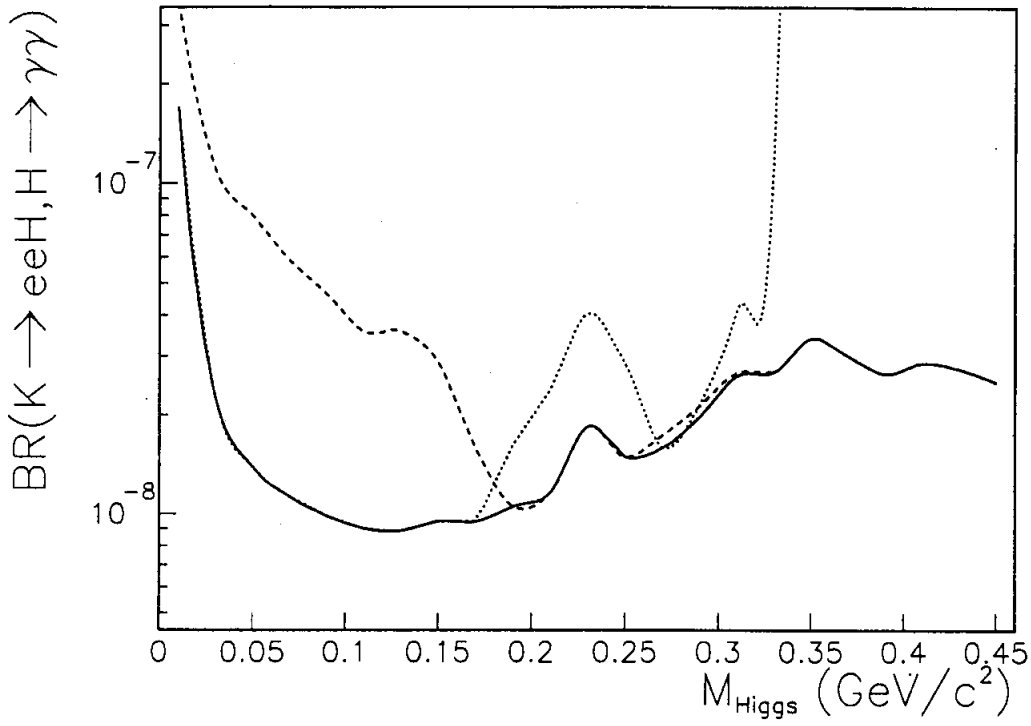

Figure 6.4: The upper limit on the branching ratio of the decay $K_L \to He^+e^-, H \to \gamma\gamma$ with the life time of $c\tau < 10^{-2}$ m. The solid line shows the final result which combined two analyses. The dashed line shows the result from the analysis with the photon energy asymmetry cut. The dotted line shows the acceptance for the final sample with additional M_{ee} and minΣcos cuts described in the text. For the Higgs-like particles with a longer life time, the limit on the branching ratio should be divided by the relative acceptance shown in Figure 6.3.

shows $M_{\gamma\gamma}$ distribution for the data and MC prediction. Since we did not observe any signatures for the decay $K_L \to He^+e^-, H \to \gamma\gamma$, we set an upper limit on the branching ratio in the same way as described previously. The result is shown in Figure 6.4.

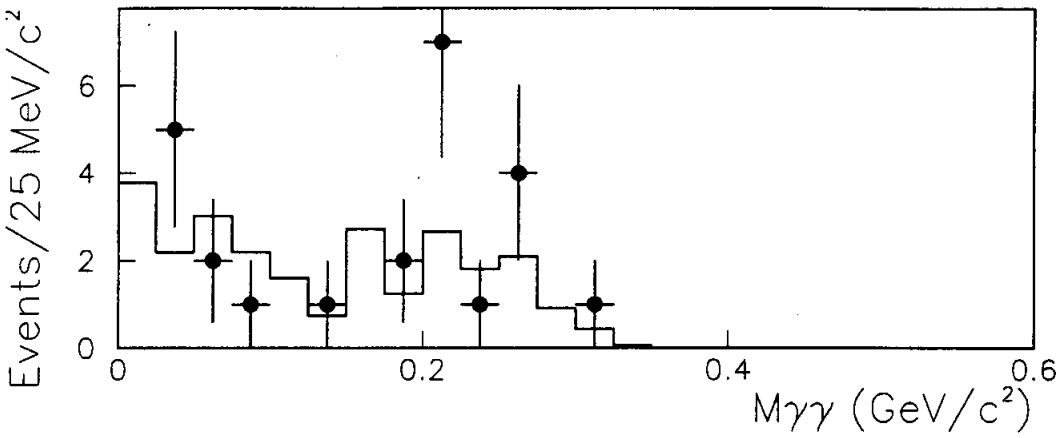

Figure 6.5: $M_{\gamma\gamma}$ distribution for the $e^+e^-\gamma\gamma$ events for Higgs-like particle search with additional requirement of $M_{ee} > 135$ MeV/c^2 and that of min$\Sigma\cos < -0.6$. The dots show the data and the solid line shows the Monte Carlo prediction from known K_L decays.

When we combined both analyses, the upper limit on the branching ratio for the decay $K_L \to He^+e^-, H \to \gamma\gamma$ is

$$BR(K_L \to He^+e^-, H \to \gamma\gamma) \;<\; 3.0 \times 10^{-8}\ (95\% C.L.) \qquad (6.1)$$

for the wide mass range between 30 and 450 MeV/c^2.

This upper limit is far smaller than any other previous searches for this kind of decays, but we did not observe any enhancements in $M_{\gamma\gamma}$ distribution, unlike the decay $K_L \to \pi^0\gamma\gamma$.

6.2.2 Discussion

We searched for Higgs-like (spin 0) particle in a model independent way where the particle was assumed to decay to two photons. A general motivation for this search is on the importance to derive the limit for such a particle from many sources as possible with high sensitivity. In addition, one of motivations of this search comes from the inconsistency of the $K_L \to \pi^0\gamma\gamma$ branching ratio between the data

and theoretical prediction. The measured $K_L \to \pi^0\gamma\gamma$ branching ratio is about three times higher than the theoretical prediction, which would indicate the existence of a Higgs-like particle, or unknown resonances which decays to two photons. The result of the $K^+ \to \pi^+\gamma\gamma$ dose not have a sensitivity to check the $K_L \to \pi^0\gamma\gamma$ result at present. Therefore, the decay $K_L \to He^+e^-, H \to \gamma\gamma$ is a unique place to see the effect.

In our search, the Higgs-like particle is not restricted to an elementary particle, but it can be a composite particle. In addition, this particle should couple to photons more strongly than to electrons and muons since we have no evidence for $K_L \to \pi^0e^+e^-$ and $K_L \to \pi^0\mu^+\mu^-$. As a matter of fact, our data in Figure 6.4 at $M_{\gamma\gamma} = M_{\pi^0}$ set a limit on the $K_L \to \pi^0e^+e^-$ branching ratio at (9×10^{-9}) $(95\%C.L.)$ [1]. Therefore, this particle must couple more strongly to quarks than electrons, which generates a photon coupling. The heavy top quark would contribute to this strong coupling.

In our model, an example of Feynman Diagram of the decay $K_L \to He^+e^-, H \to \gamma\gamma$ is shown in Figure 6.6. The $K_L \to \pi^0\gamma\gamma$ decay would also have similar diagrams as shown in Figure 6.6. Therefore, our limit to the decay $K_L \to He^+e^-, H \to \gamma\gamma$ set a limit to the unknown contribution in the decay $K_L \to \pi^0\gamma\gamma$.

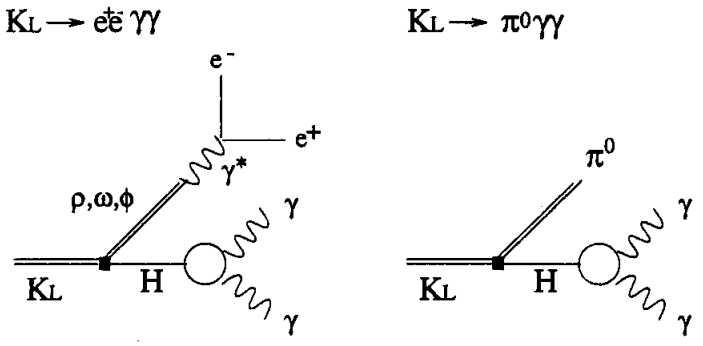

Figure 6.6: Feynman Diagram of $K_L \to He^+e^-$ decay. In addition to the above diagrams, we can also consider a contribution from the vector meson with strangeness. The similar diagrams of the decay $K_L \to \pi^0\gamma\gamma$ also shown.

Quantitatively, our limit is set on the branching ratio at around 10^{-8} compared to the excess in $K_L \to \pi^0\gamma\gamma$ branching ratio of around 10^{-6}. However, the direct comparison between the two results is difficult because of the contribution of vector meson exchange diagram in Figure 6.6. The concrete limit for the Higgs-like particle is entrusted to theorists including the expectation of the width of $H \to \gamma\gamma$ and the life time.

[1]The dedicated analysis for $K_L \to \pi^0e^+e^-$ search set a limit on the branching ratio at 4.3×10^{-9} $(90\%C.L.)$ [38, 39]

6.3 $K_L \to e^+e^-\gamma\gamma$ Background Level in Search for $K_L \to \pi^0 e^+e^-$

As we mentioned earlier, the decay $K_L \to \pi^0 e^+e^-$ is an interesting decay to see the CP violation. As shown in Section 6.2, our higgs search also set the limit on the $K_L \to \pi^0 e^+e^-$ branching ratio at $9 \times 10^{-9}(95\% C.L.)$, and our dedicated analysis set a limit at $4.3 \times 10^{-9}(90\% C.L.)$ [38, 39]. Beyond this sensitivity, the $K_L \to e^+e^-\gamma\gamma$ decay becomes most serious background in search for $K_L \to \pi^0 e^+e^-$. In this section, we will study the $K_L \to e^+e^-\gamma\gamma$ background level in search for $K_L \to \pi^0 e^+e^-$.

In Section 6.3.1, the models of $K_L \to \pi^0 e^+e^-$ are introduced. In Section 6.3.2, the difference of phase space distributions between the two decays is studied. The expected $K_L \to e^+e^-\gamma\gamma$ background level is finally given there. In Section 6.3.3, we discuss the possibility to measure the $K_L \to \pi^0 e^+e^-$ branching ratio in the future.

6.3.1 Models of the $K_L \to \pi^0 e^+e^-$ Decay

Here, we will assume two models for the decay $K_L \to \pi^0 e^+e^-$; one with a flat distribution over the available phase space, and the other, vector interaction (single-photon) model where the intermediate process is assumed to be $K_L \to \pi^0\gamma^*$. The vector interaction model is expected to represent the CP-violating $K_L \to \pi^0 e^+e^-$ decay. The differential decay spectra of these three-body are:

$$\frac{d\Gamma}{dxdy} \propto \lambda^{1/2}(1, x, x_{\pi^0}) \text{ [Flat Phase Space]} \tag{6.2}$$

$$\propto \lambda^{3/2}(1, x, x_{\pi^0})(1 - y^2), \text{ [Vector Model]} \tag{6.3}$$

where $\lambda(a, b, c) = a^2 + b^2 + c^2 - 2(ab + bc + ca)$, $x = \mathrm{M}^2_{\mathrm{ee}}/\mathrm{M}^2_{\mathrm{K_L}}$, $x_{\pi^0} = M^2_{\pi^0}/M^2_{K_L}$, and $y = \frac{2P\cdot(p_1-p_2)}{M^2_{K_L}\lambda^{1/2}(1,x,x_{\pi^0})}$ by using the four-momentum of the kaon (P), the electron (p_1) and the positron (p_2). The feature of phase space distribution of the vector interaction model can be understood in terms of conservation of angular momentum. The quantum numbers of the e^+e^- pair are mainly $J^{PC} = 1^{--}$ of the virtual photon where we ignore the spin 0 component of the virtual photon. In order to conserve the angular momentum, the e^+e^- pair must be longitudinally polarized and it must be moving in a p wave relative to the π^0. The longitudinal polarization of the e^+e^- pair causes a decay angular distribution in the e^+e^- center of mass of $\sin^2\theta$ which corresponds to the term of $1 - y^2 (y \sim \cos\theta)$ in Equation 6.3, where θ is the angle of the electron-positron pair in the center of mass frame of the pair. There is another feature that the $x(\propto \mathrm{M}^2_{\mathrm{ee}})$ spectrum of the vector model falls faster than the flat phase space by a factor of $\lambda(1, x, x_{\pi^0}) = 4|p_{\pi^0}|^2/M^2_{K_L}$. This behavior is due to an orbital angular momentum barrier. As $\mathrm{M_{ee}}$ increases, the momentum of the e^+e^- pair relative to the π^0 goes to zero while the orbital angular momentum of the e^+e^- pair must be kept to one.

The x and y spectra of both models are shown in Figure 6.7 with the spectra of the decay $K_L \to e^+e^-\gamma\gamma$. In search for $K_L \to \pi^0 e^+e^-$, the $M_{ee} > M_{\pi^0}$ cut would be applied in order to suppress the background from $K_L \to \pi^0\pi^0_D$ which is the decay $K_L \to 2\pi^0$ with a $\pi^0 \to e^+e^-\gamma$ decay. This cut is also effective to suppress the decay $K_L \to e^+e^-\gamma\gamma$ relative to both models of $K_L \to \pi^0 e^+e^-$.

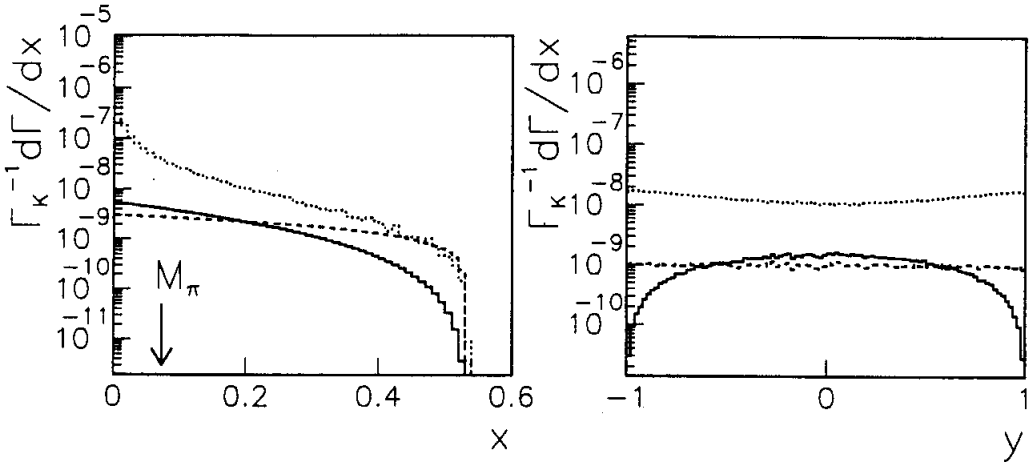

Figure 6.7: The x and y distributions of the decay $K_L \to \pi^0 e^+e^-$ are shown for the vector model (solid line) and the phase space model (dashed line). Both $K_L \to \pi^0 e^+e^-$ spectra are arbitrarily normalized to a branching ratio of 10^{-9}. As a reference, also shown is the spectrum of the decay $K_L \to e^+e^-\gamma\gamma$ (dotted line) with $M_{\gamma\gamma} = M_{\pi^0} \pm 2$ MeV/c^2. The $K_L \to e^+e^-\gamma\gamma$ spectra are normalized to the measured branching ratio.

6.3.2 Maximum Phase Space Difference

We will use a method developed by H.B. Greenlee [1] to maximize the signal ($K_L \to \pi^0 e^+e^-$) to background ($K_L \to e^+e^-\gamma\gamma$) ratio while keeping the best signal sensitivity. The signal and the background have their own density distribution in the phase space. We can calculate the signal to background ratio, let us call it R, at each given point in the phase space. The best way to maximize the reduction of background while minimizing the loss of signal, is to start removing the phase space area with the worst signal to background ratio where the ratio R is smallest. The ratio R is a function of phase space coordinate, so by removing the phase space volume with R below a given threshold, R_{min}, gives the best overall signal to background ratio for a given sensitivity.

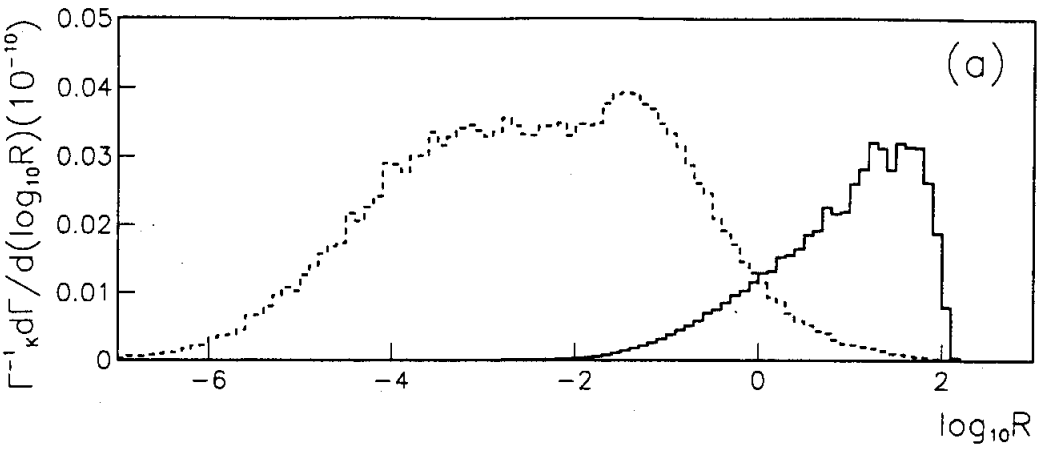

Figure 6.8: The distributions of the differential decay spectra for both the decays $K_L \to \pi^0 e^+ e^-$ (solid line) and $K_L \to e^+ e^- \gamma\gamma$ (dashed line) as a function of R, which is defined as the ratio of differential decay spectra between two decays. The $K_L \to \pi^0 e^+ e^-$ decay (vector model) was arbitrarily normalized to the branching ratio of 10^{-9}. The $K_L \to e^+ e^- \gamma\gamma$ events with the non-constant form factor are selected with the π^0 mass cut of $\pm 2\mathrm{MeV/c^2}$ and the e^+e^- invariant mass cut of $\mathrm{M_{ee}} > \mathrm{M_{\pi^0}}$.

There are 5 independent phase space variables to describe a 4-body decay[2]. Since R is a function of the phase space point, the differential decay spectrum can be expressed in terms of R, as $d\Gamma^{ee\gamma\gamma}(R)/dR$ instead of $d\Gamma^{ee\gamma\gamma}(x, y, x_\gamma, y_\gamma, \phi)/dx dy dx_\gamma dy_\gamma d\phi$. As we are interested in the region at $\mathrm{M_{\gamma\gamma}} \approx \mathrm{M_{\pi^0}}$ of the decay $K_L \to e^+e^-\gamma\gamma$, we select the $K_L \to e^+e^-\gamma\gamma$ events with the π^0 mass cut of $|\mathrm{M_{\gamma\gamma}} - \mathrm{M_{\pi^0}}| < 2\mathrm{MeV/c^2}$, which would be achieved by using a calorimeter with good energy resolution, such as CsI. In addition, the $\mathrm{M_{ee}} > \mathrm{M_{\pi^0}}$ cut is applied to suppress the $K_L \to \pi^0\pi^0_D$ background.

Figure 6.8 shows the decay spectra of both $K_L \to e^+e^-\gamma\gamma$ and $K_L \to \pi^0 e^+ e^-$ as a function of R. In the figure, the ratio of two decay spectra is equal to R, by definition. Since we are interested in the distribution of R, we can choose the $K_L \to \pi^0 e^+ e^-$ branching ratio arbitrarily, which is normalized to the branching ratio of 10^{-9}. As an example, we will first show some results with the vector model of $K_L \to \pi^0 e^+ e^-$, and with the $K_L \to e^+e^-\gamma\gamma$ decay of the non-constant form factor of the parameter $\alpha_{K^*} = -0.28$ as shown in Equation 1.3. The maximum rejection factor is shown as

[2]In case of this analysis, the number of independent phase space variables is actually 4 because we are interested in the region at $\mathrm{M_{\gamma\gamma}} \approx \mathrm{M_{\pi^0}}$ of the decay $K_L \to e^+e^-\gamma\gamma$.

the maximum value of R (R_{max}), which is $log_{10}R_{max} = 2.1(R_{max} = 126)$. Let us pick up a threshold on R, R_{min}, and accept events above it. The overall signal to background ratio is

$$\int_{R_{min}}^{R_{max}} \frac{d\Gamma(R)^{\pi^0 ee}}{dR} dR / \int_{R_{min}}^{R_{max}} \frac{d\Gamma(R)^{ee\gamma\gamma}}{dR} dR.$$

This is the best signal to background ratio for the signal efficiency since the phase space volume with $R < R_{min}$ has worse signal to background ratio that that at $R > R_{min}$. The efficiencies of the phase space cut for $K_L \to e^+e^-\gamma\gamma$ and $K_L \to \pi^0 e^+e^-$ are formalized as $\epsilon = \int_{R_{min}}^{R_{max}} \frac{d\Gamma(R)}{dR} dR$. Therefore, the selection efficiencies are functions of R_{min}, and are shown in Figure 6.9.

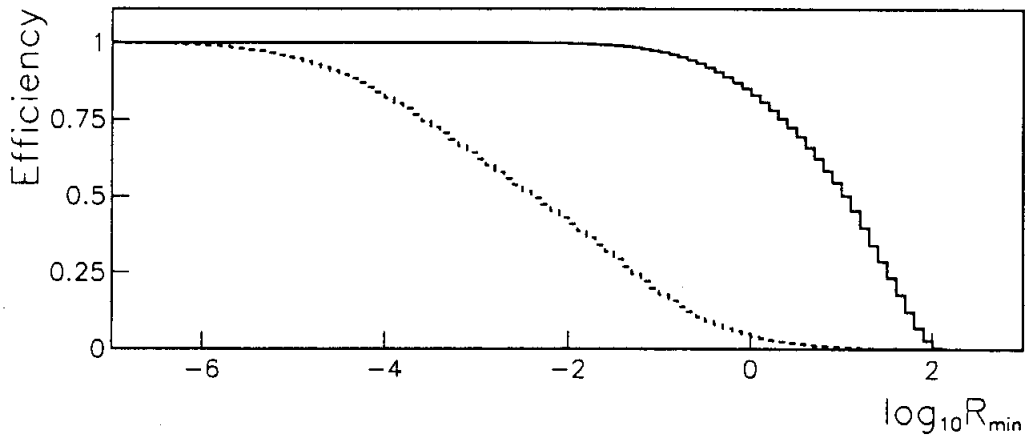

Figure 6.9: The efficiency of the phase space cut as a function of R_{min} for the decays $K_L \to \pi^0 e^+e^-$ (solid line) and $K_L \to e^+e^-\gamma\gamma$ (dashed line).

The effective background branching ratio is defined as:

$$B_{e^+e^-\gamma\gamma} = \tag{6.4}$$
$$BR(K_L \to e^+e^-\gamma\gamma, |M_{\gamma\gamma} - M_{\pi^0}| < 2\text{MeV/c}^2, M_{ee} > M_{\pi^0}) \times \frac{\epsilon_{ee\gamma\gamma}}{\epsilon_{\pi^0 ee}},$$

where $\epsilon_{ee\gamma\gamma}$ and $\epsilon_{\pi^0 ee}$ are the efficiencies of the phase space cut for the decay $K_L \to e^+e^-\gamma\gamma$ and $K_L \to \pi^0 e^+e^-$, respectively. The $K_L \to e^+e^-\gamma\gamma$ branching ratio is $BR(K_L \to e^+e^-\gamma\gamma, |M_{\gamma\gamma} - M_{\pi^0}| < 2\text{MeV/c}^2, M_{ee} > M_{\pi^0}) = 2.5 \times 10^{-9}$ based on our measurement of $BR(K_L \to e^+e^-\gamma\gamma, E_\gamma^* \geq 5 \text{ MeV}) = 6.5 \times 10^{-7}$. The cut, $M_{ee} > M_{\pi^0}$, reduces the $K_L \to \pi^0 e^+e^-$ efficiency to $\epsilon_{\pi^0 ee} \to 0.65\epsilon_{\pi^0 ee}$. Thus, the

effective background branching ratio is:

$$B_{e^+e^-\gamma\gamma} = 3.8 \times 10^{-9} \frac{\epsilon_{ee\gamma\gamma}(R_{min})}{\epsilon_{\pi^0 ee}(R_{min})} \tag{6.5}$$

The effective background branching ratio is plotted as a function of R_{min} in Figure 6.10. In addition, the effective background branching ratio is shown as a function of

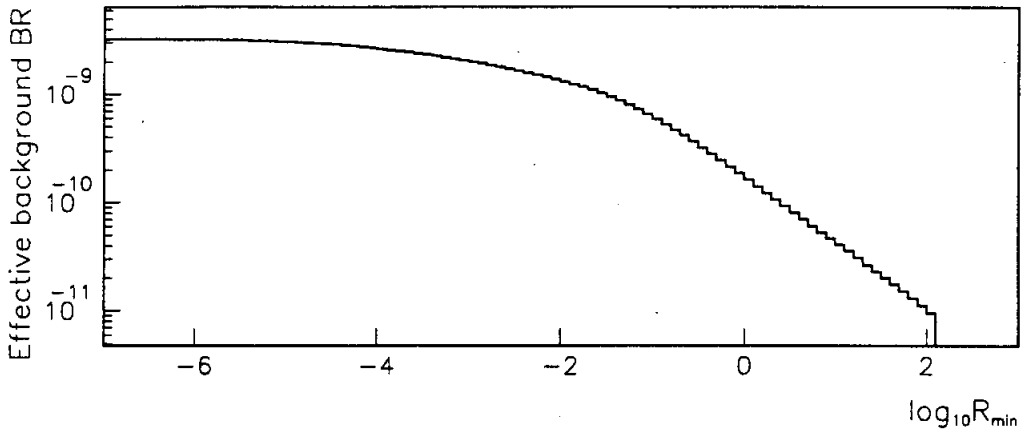

Figure 6.10: The effective $K_L \to e^+e^-\gamma\gamma$ background branching ratio $(3.8 \times 10^{-9} \frac{\epsilon_{ee\gamma\gamma}(R_{min})}{\epsilon_{\pi^0 ee}(R_{min})})$ as a function of R_{min}.

the $K_L \to \pi^0 e^+ e^-$ efficiency ($\epsilon_{\pi^0 ee}$) in Figure 6.11, which is easy to understand the background level from the experimental point of view. The minimum $K_L \to e^+e^-\gamma\gamma$ background level is reached at $R_{min} = R_{max}$ in Figure 6.10, or $\epsilon_{\pi^0 ee}(R_{min}) \to 0$ in Figure 6.11. This point corresponds to $x = x_{\pi^0}$, $y = 0$, $y_\gamma = 0$ and $\phi = \pi/2$ where the phase space variables are defined in Chapter 3. The minimum $K_L \to e^+e^-\gamma\gamma$ background level is listed in Table 6.1 for both phase space and vector models of $K_L \to \pi^0 e^+ e^-$ and with and without the non-constant $K_L \to e^+e^-\gamma\gamma$ form factor. The values in Table 6.1 are close to the $K_L \to \pi^0 e^+ e^-$ branching ratio expected by the standard model ($\sim 10^{-11}$, see Table 1.1). The limit in Table 6.1 scales linearly with the π^0 mass cut at the first approximation. Therefore, the calorimeter with good energy resolution is necessary. In the table, the predictions of the background level depend on both the model of $K_L \to \pi^0 e^+ e^-$ and the form factor of $K_L \to e^+e^-\gamma\gamma$. Therefore, we need more knowledge of the $K_L \to \pi^0 e^+ e^-$ decay spectra, and need further measurement of the $K_L \to e^+e^-\gamma\gamma$ form factor.

These results do not suggest that it is impossible to observe the decay $K_L \to \pi^0 e^+ e^-$, but that there is an attendant background to the decay $K_L \to \pi^0 e^+ e^-$ at

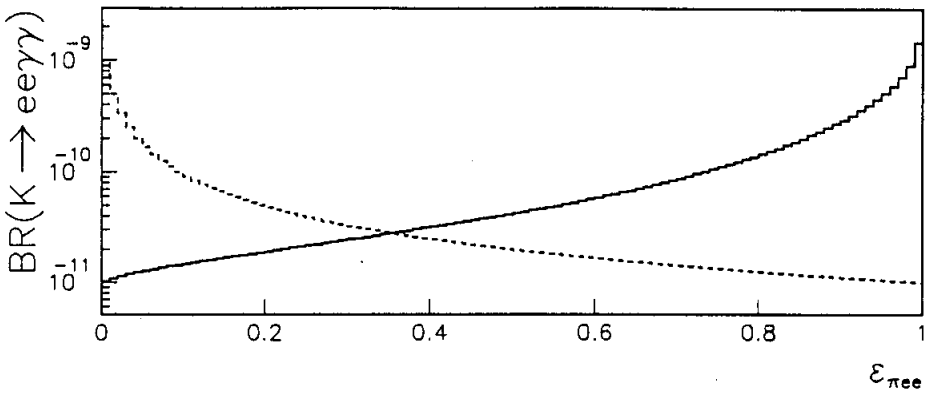

Figure 6.11: The effective $K_L \to e^+e^-\gamma\gamma$ background branching ratio to the decay $K_L \to \pi^0 e^+ e^-$ as a function of $\epsilon_{\pi^0 ee}$. In addition, the $K_L \to \pi^0 e^+ e^-$ single event sensitivity (referred as SES) is shown by the dotted line, normalized to $SES = 10^{-11}$ at $\epsilon_{\pi^0 ee} = 1$. At the cross point, one background event is expected.

Table 6.1: The lower limits of the effective $K_L \to e^+e^-\gamma\gamma$ background to the decay $K_L \to \pi^0 e^+ e^-$ are listed for both models of the $K_L \to \pi^0 e^+ e^-$ and with and without the form factor of the decay $K_L \to e^+e^-\gamma\gamma$.

The model of the $K_L \to \pi^0 e^+ e^-$	The lower limit of the $K_L \to e^+e^-\gamma\gamma$ branching ratio	
	non-constant form factor	constant form factor
Vector Model	1.0×10^{-11}	0.6×10^{-11}
Phase Space Model	1.6×10^{-11}	0.7×10^{-11}

the expected branching ratio. For example, let us consider an experiment which aims for a single event sensitivity of 10^{-11} for the vector model $K_L \to \pi^0 e^+ e^-$ decay at $\epsilon_{\pi^0 ee} = 1$. Without the $K_L \to e^+ e^- \gamma\gamma$ background cut, there will be $3.8 \times 10^{-9} \div 10^{-11} = 380$ $K_L \to e^+ e^- \gamma\gamma$ events. The single event sensitivity is proportional to $1/\epsilon_{\pi^0 ee}$, as shown in Figure 6.11. The number of background events is given by the ratio between the background level and the sensitivity, and it decreases as tighter cut is applied (low $\epsilon_{\pi^0 ee}$). At the crossing point between the single event sensitivity and the background level in Figure 6.11, the number of background events is reduced to one, with a loss of factor 3 in the $K_L \to \pi^0 e^+ e^-$ sensitivity.

6.3.3 Designed $K_L \to \pi^0 e^+ e^-$ Sensitivity

If the standard model is correct, it is apparent that the decay $K_L \to \pi^0 e^+ e^-$ must be searched for as a peak at M_{π^0} on top of broad $M_{\gamma\gamma}$ distribution of the $K_L \to e^+ e^- \gamma\gamma$ decay. In this section, we study how much sensitivity is required to measure the $K_L \to \pi^0 e^+ e^-$ branching ratio over the $K_L \to e^+ e^- \gamma\gamma$ background. We study the relation between the measurable $K_L \to \pi^0 e^+ e^-$ branching ratio and the required single event sensitivity.

In order to measure the $K_L \to \pi^0 e^+ e^-$ branching ratio, the number of the signal events must be greater than 3σ of the background fluctuation. In this section, we will assume that the number of the background events is large enough that the fluctuation can be treated as Gaussian, and the background level is estimated with no error from mass side bands. This assumption leads to the following relation:

$$N_S \;>\; 3\sqrt{N_S + N_{BG}} \tag{6.6}$$

where N_S and N_{BG} are the number of the signal events and background events, respectively. The number of the signal events, N_S, is formalized as $\#K_L \times \epsilon_{\pi^0 ee} \times BR(K_L \to \pi^0 ee)$ where $\#K_L$ is the kaon flux and $\epsilon_{\pi^0 ee}$ is an efficiency for $K_L \to \pi^0 e^+ e^-$. We separate the efficiency, $\epsilon_{\pi^0 ee}$, into two parts ($\epsilon'_{\pi^0 ee} \cdot \epsilon''_{\pi^0 ee}$): one part is the detector acceptance ($\epsilon'_{\pi^0 ee}$), and the other part reveals the efficiency of the phase space cut ($\epsilon''_{\pi^0 ee}$). Assuming that the detector acceptance would give no bias to the decay $K_L \to \pi^0 e^+ e^-$ in the phase space, $\epsilon''_{\pi^0 ee}$ is equal to the efficiency which was defined in Section 6.3.2. The single event sensitivity, S, is defined as $S = 1/(\#K_L \times \epsilon'_{\pi^0 ee})$. Therefore, Relation 6.6 is formalized as:

$$\#K_L \cdot \epsilon_{\pi^0 ee} \cdot BR(K_L \to \pi^0 ee) > 3\sqrt{\#K_L \cdot \epsilon_{\pi^0 ee} \cdot BR(K_L \to \pi^0 ee) + \#K_L \cdot \epsilon_{ee\gamma\gamma} \cdot BR(K_L \to ee\gamma\gamma)}$$

$$\frac{\epsilon''_{\pi^0 ee} BR(K_L \to \pi^0 ee)}{S} > 3\sqrt{\frac{\epsilon''_{\pi^0 ee} BR(K_L \to \pi^0 ee)}{S} + \frac{\epsilon'_{ee\gamma\gamma}\epsilon''_{ee\gamma\gamma} BR(K_L \to ee\gamma\gamma)}{\epsilon'_{\pi^0 ee} \cdot S}},$$

where $\epsilon'_{ee\gamma\gamma}$ and $\epsilon''_{ee\gamma\gamma}$ are the detector acceptance and the efficiency of the phase space cut for the decay $K_L \to e^+e^-\gamma\gamma$, respectively. Assuming that $\epsilon'_{ee\gamma\gamma}$ is equal to $\epsilon'_{\pi^0 ee}$, we finally reach the following relation:

$$\frac{\epsilon''_{\pi^0 ee} BR(K_L \to \pi^0 ee)}{S} > 3\sqrt{\frac{\epsilon''_{\pi^0 ee} BR(K_L \to \pi^0 ee)}{S} + \frac{\epsilon''_{ee\gamma\gamma} BR(K_L \to ee\gamma\gamma)}{S}}.$$

In the above relation, the first term in the square root is the number of $K_L \to \pi^0 e^+e^-$ signal and the second term is the number of $K_L \to e^+e^-\gamma\gamma$ background events. Since the number of background events would be larger than the number of signal events at the sensitivity of the standard model prediction, the first term could be ignored. Without the first term, the measurable branching ratio is expressed by a simple function of the single event sensitivity:

$$BR(K_L \to \pi^0 e^+e^-) > \sqrt{\frac{9}{(\epsilon''_{\pi^0 ee})^2/\epsilon''_{ee\gamma\gamma}} BR(K_L \to e^+e^-\gamma\gamma) \cdot S}. \qquad (6.7)$$

The smallest detectable branching ratio of the signal can be reached when the $(\epsilon''_{\pi^0 ee})^2/\epsilon''_{ee\gamma\gamma}$ is the maximum. The maximum value of the $(\epsilon''_{\pi^0 ee})^2/\epsilon''_{ee\gamma\gamma}$ is expected to be 41 in Figure 6.9 where the efficiencies for $K_L \to \pi^0 e^+e^-$ and $K_L \to e^+e^-\gamma\gamma$ are 0.40 and 0.0039, respectively. The result from Equation 6.7 is shown in Figure 6.12. We can see from Figure 6.12 that a single event sensitivity of 6.0×10^{-14} is required in order to detect the $K_L \to \pi^0 e^+e^-$ with the branching ratio of 10^{-11}. The future $K_L \to \pi^0 e^+e^-$ experiment which is designed for such a single event sensitivity could make a statistically significant observation of the $K_L \to \pi^0 e^+e^-$.

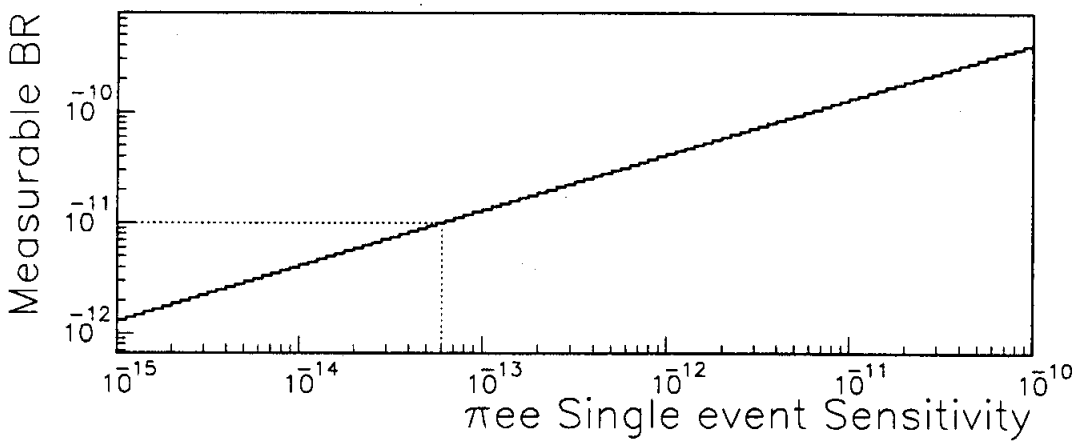

Figure 6.12: The $K_L \to \pi^0 e^+ e^-$ single event sensitivity versus the measurable branching ratio when the number of the $K_L \to \pi^0 e^+ e^-$ signal is required to be greater than 3σ of the background fluctuation with the π^0 mass cut of $\pm 2 \mathrm{MeV/c^2}$ and the e^+e^- mass cut of $M_{ee} > M_{\pi^0}$. The vector model of the $K_L \to \pi^0 e^+ e^-$ and the non-constant form factor of the $K_L \to e^+e^-\gamma\gamma$ was assumed. The point shown in Figure means that the sensitivity of 6.0×10^{-14} is needed in order to measure the $K_L \to \pi^0 e^+ e^-$ branching ratio of 10^{-11}.

Chapter 7

Conclusion

An experimental study of the decay $K_L \to e^+e^-\gamma\gamma$ has been performed in this thesis.

We observed $57.5 \pm 8.5(stat)$ $K_L \to e^+e^-\gamma\gamma$ decays on top of $11.5 \pm 2.0(stat)$ expected background events. Based on this sample, the radiative $K_L \to e^+e^-\gamma\gamma$ branching ratio is measured to be:

$$BR(K_L \to e^+e^-\gamma\gamma, E_\gamma^* \geq 5 \text{ MeV}) = [6.5 \pm 1.2(stat) \pm 0.6(syst)] \times 10^{-7}.$$

This result represents the first statistically significant measurement of the branching ratio and is consistent with the theoretical prediction, $(5.8 \pm 0.27) \times 10^{-7}$. This result also presents the first verification of the radiative correction for the decay $K_L \to e^+e^-\gamma$. In addition to this measurement, the phase space variables, such as M_{ee} and $M_{\gamma\gamma}$, are observed for the first time for the decay $K_L \to e^+e^-\gamma\gamma$. We confirmed that these distributions are consistent with the prediction for the radiative $K_L \to e^+e^-\gamma\gamma$ decay.

As described in Chapter 1, the $K_L \to \gamma\gamma^*$ form factor is interesting in its own right. The form factor should be determined in order to understand the long distance physics and to extract the short distance contribution covered with the long distance contribution. The form factor was not measured more precisely than that of the current measurement because of the lack of statistics. However, the measured branching ratio can help to determine the form factor on the decay $K_L \to e^+e^-\gamma$ since the ambiguity in the $K_L \to e^+e^-\gamma$ radiative correction is now resolved. We expect that this form factor will be determined in the next run of E799.

Furthermore, we searched for the direct emission process in the decay $K_L \to e^+e^-\gamma\gamma$. The direct emission process in the decay $K_L \to e^+e^-\gamma\gamma$ is a mysterious part in both experiment and theory. We did not observe a signature for such a process, and we set the upper limit on the branching ratio:

$$BR(K_L \to e^+e^-\gamma\gamma[direct]) < 4.5 \times 10^{-8} \ (95\% C.L.).$$

This is the first search for this process. Though the presented upper limit is very close to the naive expectation, $\sim 3.1 \times 10^{-8}$, the expectation is not excluded. This

result also provides the constraint on the coupling strength of the anomalous vertexes in the ChPT which are shown in Figure 1.7. In addition, the result set the constraint for the short distance contribution in the decay $K_L \to e^+e^-\gamma\gamma$. In order to put a quantitative constraint on the above effects, more theoretical efforts are expected. In order to search for this decay at the sensitivity of the ChPT prediction, the $e^+e^-\gamma\gamma$ sample with higher statistics is required. We expect that we will get the sample in the next run of E799. In addition to the higher statistics, an exact theoretical calculation is needed in order to optimize the selection criteria for this process.

This search indirectly set the limit on the decay $K_L \to \gamma\gamma\gamma$. In the kaon system, the C-violating decay $K_L \to \gamma\gamma\gamma$ is allowed, but it has never been searched for experimentally. The upper limit on the branching ratio of the decay $K_L \to \gamma\gamma\gamma$ is indirectly set to be:

$$BR(K_L \to \gamma\gamma\gamma) \ < \ 1.7 \times 10^{-5} \ (95\% C.L.),$$

with an assumption of $BR(K_L \to \gamma^*\gamma\gamma \to e^+e^-\gamma\gamma) = \alpha_{QED} BR(K_L \to \gamma\gamma\gamma)$. Though the upper limit on the branching ratio of the decay $K_L \to \gamma\gamma\gamma$ does not reach the level of the theoretical prediction, $\sim 3 \times 10^{-19}$, this result is the first constraint for the decay $K_L \to \gamma\gamma\gamma$.

We also searched for a Higgs-like particle in the decay $K_L \to He^+e^-, H \to \gamma\gamma$. The Higgs-like particle is a keystone in the current particle physics. Therefore, many experiments have tried to discover the signal including this experiment. We did not get any evidences for the particle. We set the upper limit on the branching ratio:

$$BR(K_L \to He^+e^-, H \to \gamma\gamma) \ < \ 3.0 \times 10^{-8} \ (95\% C.L.),$$

for the mass between 30 and 450 MeV/c^2 with the life time of $c\tau < 10^{-2}$ m. The upper limit as a function of $M_{\gamma\gamma}$ is shown in Figure 6.4. As mentioned in Chapter 1, this result is important in order to derive limit for such an unknown particle from as many as sources as possible. In Chapter 1, we pointed the inconsistency between the experiment and theory in the decay $K_L \to \pi^0\gamma\gamma$. In case of the decay $K_L \to e^+e^-\gamma\gamma$, we did not see any enhancements in $M_{\gamma\gamma}$ distribution. This upper limit is also lower than the result from the $K^+ \to \pi^+\gamma\gamma$ decay. In addition, our search covered the wide mass range ($30 < M_{Higgs}(\mathrm{MeV/c^2}) < 450$), in the kaon system for the particle with a short life time. The derivation of the concrete limit for the Higgs-like particle is entrusted to theorists including the expectation of the width of $H \to \gamma\gamma$ and the life time.

The decay $K_L \to e^+e^-\gamma\gamma$ strongly arrests the attention as a serious background for the CP violating decay $K_L \to \pi^0e^+e^-$. The background level is studied by using this measured $K_L \to e^+e^-\gamma\gamma$ branching ratio. The lowest limit of the $K_L \to e^+e^-\gamma\gamma$ background level depends on both $K_L \to e^+e^-\gamma\gamma$ form factor and the models of $K_L \to \pi^0e^+e^-$. The results are summarized in Table 7.1 where $M_{\gamma\gamma}$ mass cut is chosen to be within 2 MeV/c^2 of the π^0 mass. The mass cut is chosen by the typical resolution of the high resolution electromagnetic calorimeter, such as CsI.

Table 7.1: The lower limits of the effective $K_L \to e^+e^-\gamma\gamma$ background to the decay $K_L \to \pi^0e^+e^-$ are listed for both Vector and Phase Space models of the $K_L \to \pi^0e^+e^-$ and with both constant and non-constant form factors. The non-constant form factor is formulated in Chapter 1 with the parameter of $\alpha_{K^*} = -0.28$. $M_{\gamma\gamma}$ mass cut is chosen within 2 MeV/c^2 of the π^0 mass.

$K_L \to \pi^0e^+e^-$ models	The lower limit of the $K_L \to e^+e^-\gamma\gamma$ branching ratio	
	non-constant form factor	constant form factor
Vector Model	1.0×10^{-11}	0.6×10^{-11}
Phase Space Model	1.6×10^{-11}	0.7×10^{-11}

The $K_L \to e^+e^-\gamma\gamma$ background is at the same level as the $K_L \to \pi^0e^+e^-$ prediction in the standard model. Therefore, the continuous study for the decay $K_L \to e^+e^-\gamma\gamma$ is expected in order to find the decay $K_L \to \pi^0e^+e^-$ and to measure the parameter η in KM matrix from the decay $K_L \to \pi^0e^+e^-$.

This result is the first statistically significant measurement of the decay $K_L \to e^+e^-\gamma\gamma$. Improvements in the measurements in the future rare K_L decay experiments such as KTeV [41], will lead us to understand the long distance physics, to extract the reliable parameters in the short distance physics and to discover the new physics outside of the standard model.

Appendix A

$K_L \to e^+e^-\gamma$ Form Factor and Decay $K_L \to e^+e^-\gamma\gamma$

In this appendix, we discuss the effect of the radiative correction and the radiative Dalitz $K_L \to e^+e^-\gamma\gamma$ decay to the measurement of the $K_L \to e^+e^-\gamma$ form factor. The $K_L \to e^+e^-\gamma$ decay and especially its form factor are important in order to understand the long distance physics as described in Chapter 1.

A.1 Radiative Correction and K_L Dalitz Decay Form Factor

The radiative correction to the decay $K_L \to e^+e^-\gamma$ changes the e^+e^- invariant mass distribution as shown in Figure 1.5. Since the form factor is derived from the difference between the observed e^+e^- invariant mass and the prediction from QED, it is important to apply the correct radiative correction. Here, we define "measurable form factor" as:

$$F(x) = \frac{|f(x)|^2 \times (d\Gamma/dx + d\Gamma^{\mathrm{rad.}}/dx)}{d\Gamma/dx},$$

where x is $(\mathrm{M_{ee}}/\mathrm{M_{K_L}})^2$, $f(x)$ is the form factor shown in Equation 1.1, $d\Gamma/dx$ is the differential decay spectrum of $K_L \to e^+e^-\gamma$ in the lowest QED, and $d\Gamma^{\mathrm{rad.}}/dx$ is the radiative correction to $d\Gamma/dx$.

In Figure A.1, the shape of the measurable form factor with the radiative correction is shown with the parameter of $\alpha_{K^*} = -0.28$. The shape is similar to that of the measurable form factor of the parameter $\alpha_{K^*} = -0.22$ without the radiative correction at the range of $x < 0.6$ where the current $K_L \to e^+e^-\gamma$ form factor was actually measured. Therefore, it is important to treat the radiative correction correctly, in order to measure α_{K^*}. This result suggests that the effect of the radiative correction is equivalent to the reduction of the form factor. Actually, we can roughly explain the difference of the reported α_{K^*} [26] between with ($\alpha_{K^*} = -0.28$) and without ($\alpha_{K^*} = -0.18$) the radiative correction.

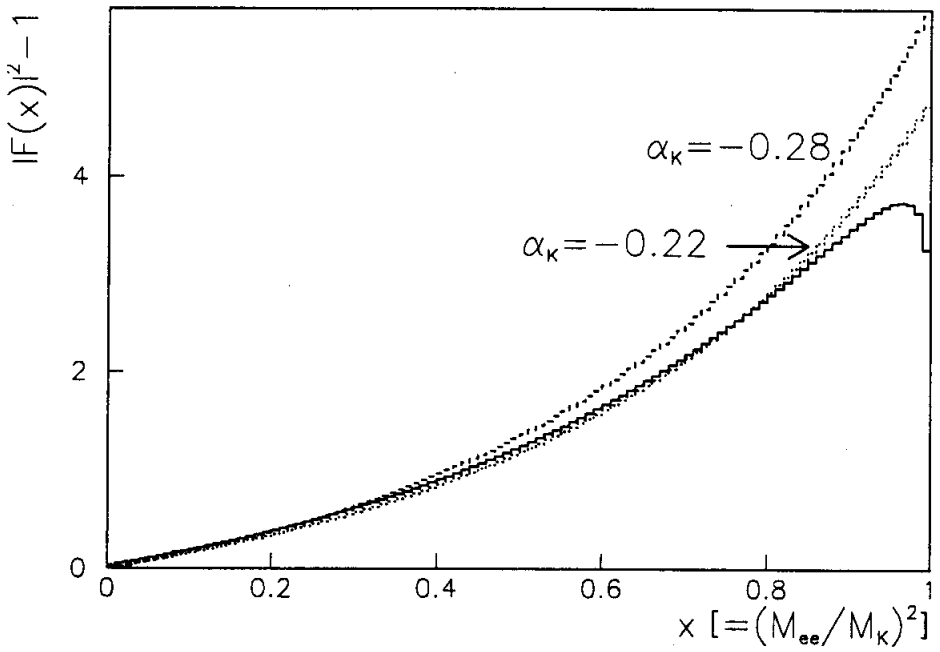

Figure A.1: The effect of the radiative correction to the K_L Dalitz decay form factor with the parameter of $\alpha_{K^*} = -0.28$. The measurable form factor, $F(x)$, with the radiative correction is shown by solid line and that without the radiative correction is shown by dashed line. As a reference, the measurable form factor of the parameter $\alpha_{K^*} = -0.22$ without the radiative correction is shown by dotted line. The shape of the form factor of the parameter $\alpha_{K^*} = -0.22$ without the radiative correction is very similar as the shape of the form factor of the parameter $\alpha_{K^*} = -0.28$ with the radiative correction.

A.2 Decay $K_L \to e^+e^-\gamma\gamma$ and the Form Factor of the $K_L \to e^+e^-\gamma$ Decay

Let us next discuss how the $K_L \to e^+e^-\gamma\gamma$ decay can affect the $K_L \to e^+e^-\gamma$ form factor measurement. The size of the effect depends on the detector configuration. Let us consider two types of detector; one without a spectrometer magnet and the other with the magnet. Without a magnet, M_{ee}, and the form factor would be measured by the positron and electron energies and their opening angle. One example is CERN NA31 experiment [52]. The detector with a magnet would measure M_{ee} by the momentum of the positron and electron and their opening angle. One example is our detector of FNAL E799 or the detector of BNL E845 [26]. The contribution of the $K_L \to e^+e^-\gamma\gamma$ decay to the form factor measurement is different between the two cases.

With the nonmagnetic detector, since the radiative photon would fall into the same energy cluster as the parent electron, the measured energy of the electron tend to be larger than expected. This effect enhances the part with large M_{ee}. This effect is in the opposite direction to the radiative correction described in Section A.1, which suppress large M_{ee}. It is impossible to calculate the quantitative value of this effect without specifying the experiment. As an example, this effect was reported in the reference [53, 54] for the experiment of the π^0 Dalitz decay at TRIUMF.

With the magnetic detector, the radiative photon can be separated from the parent electron, and the decay is observed as the decay $K_L \to e^+e^-\gamma\gamma$. This means that the $K_L \to e^+e^-\gamma\gamma$ term would be missed from the $K_L \to e^+e^-\gamma$ since M_{ee} distribution of the $K_L \to e^+e^-\gamma\gamma$ is different from that of the $K_L \to e^+e^-\gamma$. This effect depends on the detector configuration, such as the strength of the magnet field, the photon energy threshold, the position resolution of the photon and etc.. In order to simulate and study this effect, an extreme case was assumed, where the $K_L \to e^+e^-\gamma\gamma$ with $E^* > 5$ MeV is removed from the decay $K_L \to e^+e^-\gamma$ where E^* is the minimum energy of two photons in the center of mass frame of the kaon. The effect of the missing $K_L \to e^+e^-\gamma\gamma$ is shown in Figure A.2. As shown in Figure A.2, the effect of the missing $K_L \to e^+e^-\gamma\gamma$ decay has a negative slope at the $x < 0.1$ and a positive slope at the $x > 0.2$ where the effect is opposite to the radiative correction as explained in Section A.1. The combined effect of both the missing $K_L \to e^+e^-\gamma\gamma$ and the radiative correction to M_{ee} is also shown in Figure A.2. What we understand from Figure A.2 is that both effects are important for the measurement of the form factor.

It is clear that both effects of the radiative correction to M_{ee} and the missing $K_L \to e^+e^-\gamma\gamma$ must be considered for the precise measurement of the $K_L \to e^+e^-\gamma$ form factor. Therefore, it is important to measure M_{ee} distribution of $K_L \to e^+e^-\gamma\gamma$ more precisely.

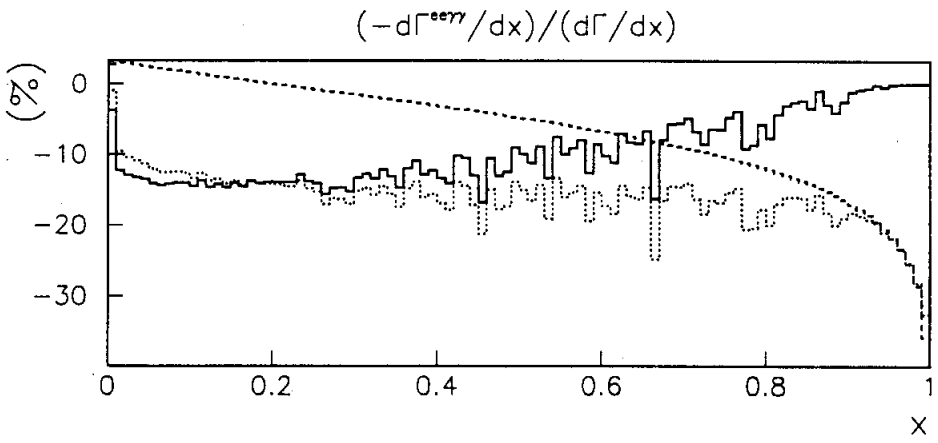

Figure A.2: $K_L \to e^+e^-\gamma\gamma$ contribution to the $K_L \to e^+e^-\gamma$ from factor. The solid line shows the change in the x distribution of $K_L \to e^+e^-\gamma$ caused by missing $K_L \to e^+e^-\gamma\gamma$ ($E^* > 5$ MeV). The dashed line shows the effect of the radiative correction as explained previously in Section A.1. The combined effect of both the missing $K_L \to e^+e^-\gamma\gamma$ and the radiative correction is plotted by the dotted line.

Bibliography

[1] H.B. Greenlee, Phys. Rev. **D42**, 3724 (1990).

[2] B. Winstein and L. Wolfenstein, Rev. Mod. Phys. **65** 1113 (1993).

[3] J.L. Ritchie and S.G. Wojcicki, Rev. Mod. Phys. **65** 1149 (1993).

[4] R. Battiston, D. Cocolicchio, G.L. Fogli and N. Paver, Phys. Rep. **214** 293 (1992).

[5] G. D'Ambrosio, G. Ecker, G. Isidori and H. Neufeld, hep-ph **9411439** CERN-TH.7503/94 (1994).

[6] M. Kobayashi and T. Maskawa, Prog. Theor. Phys. **49**, 652 (1973).

[7] L. Wolfenstein, Phys. Rev. Lett. **51**, 1945 (1983).

[8] Andrzeg J. Buras, hep-ph **9406272** MPI-PhT/94-30 (1994).

[9] L. Littenberg and G. Valencia, Ann. Rev. Nucl. Part. Sci. **43** 729 (1993).

[10] A. Pich, hep-ph **9308351** CERN-TH.6978/93 (1993).

[11] J. bijnens, G. Ecker and J. Gasser, hep-ph **9411232**, DAΦNE Physics Handbook.

[12] A. J. Buras, M. E. Lautenbacher, M. Misiak, and M. Munz, Direct CP violation in $K_L \to \pi^0 e^+ e^-$ beyond leading logarithms, Technical Report MPI-Ph/94-11, Max Planck Institut fur Physik, February 1994.

[13] G. Isidori, private communication (1995).

[14] G. D'Ambrosio, private communication (1995).

[15] Parkins, Introduction to the High Energy Physics.

[16] I. S. Hughes, Elementary particles (third edition), 136 (1990).

[17] G. D. Barr *et al.*, Phys. Lett. **B317**, 233 (1993).

[18] L. K. Gibbons *et al.*, Phys. Rev. Lett. **70**, 1203 (1993).

[19] L. Wolfenstein, Phys. Rev. Lett. **13**, 562 (1964).

[20] W. M. Morse, *et al.*, Phys. Rev. **D45**, 36 (1992).

[21] H. Burkhardt, *et al.*, Phys. Lett. **B199**, 139 (1987).

[22] L.Bergström, E.Massó, and P. Singer, Phys. Lett. **131B**, 229 (1983).

[23] N. M. Kroll and W. Wada, Phys. Rev. **98**, 1355 (1955).

[24] P. Ko, Phys. Rev. **D44**, 139 (1991).

[25] M. Spencer, *et al.*, to be published to Phys. Rev. Lett. (1995)

[26] K.E. Ohl, *et al.*, Phys. Rev. Lett. **65**, 1407 (1990).

[27] K. O. Mikaelian and J. Smith, Phys. Rev. **D5**, 2890 (1972).

[28] K. O. Mikaelian and J. Smith, Phys. Rev. **D5**, 1764 (1972).

[29] P. Heiliger, B. McKellar, and L.M. Sehgal, Phys. Lett. **B327**, 145 (1994).

[30] B. McKellar, private communication (1994).

[31] P. Heiliger and L.M. Sehgal, Phys. Lett. **B307**, 182 (1993).

[32] D. P. Majumdar and J. Smith, Phys. Rev. **187**, 2039 (1969)

[33] M.S. Atiya, *et al.*, hys. Rev. Lett. **65**, 1188 (1990).

[34] G.D. Barr, *et al.*, Phys. Lett. **284B**, 440 (1992).

[35] C. O. Dib, I. Dunietz, and F. J. Gilman, Phys. Rev. **D39**, 2639 (1989).

[36] P. Heiliger and L. M. Sehgal, Phys. Rev. **D47**, 4920 (1993).

[37] G. Ecker, A. Pich, and E. de Rafael, Nucl. Phys. **B291**, 692 (1987).

[38] D. A. Harris, *et al.*, Phys. Rev. Lett. **71**, 3918 (1993).

[39] Deborah Appel Harris, PhD thesis, University of Chicago, April 1994.

[40] N. Miyake, *et al.*, KEK Proposal 162 (1988).

[41] K. Arisaka, *et al.*, KTeV Design Report, FN-580 (1992).

[42] T. Nakaya *et al.*, Phys. Rev. Lett. **73**, 2169 (1994)

[43] Particle Data Group, K.Hikasa *et al.*, Phys. Rev. **D45** S1 (1992).

[44] T. Ferbel, *Experimental Tecniques in High Energy Physics.*

[45] M. Karlsson, PhD thesis, Princeton University, August, 1990

[46] V. Papadimitriou, PhD thesis, University of Chicago, December 1990.

[47] H. Sanders *et al.*, IEEE Trans. Nucl. Sci. **36**, 358 (1989).

[48] K.S. McFarland, PhD thesis, University of Chicago, November 1993.

[49] H.A. Bethe, Rev. Rev. **89**, 1256 (1953).

[50] R. Ford and W. Nelson, Technical Report UC-32, SLAC, June 1978.

[51] Louis Lyons, *Statistics for nuclear and particle physicists*, (Cambridge University Press) Sec 1.4.2, page 13.

[52] G.D. Barr, *et al.*, Phys. Lett. **240B**, 283 (1990).

[53] L. Roberts and J. Smith, Phys. Rev. **D33**, 3457 (1986).

[54] F. Farzanpay, *et al.*, Phys. Lett. **278B**, 413 (1992).